THERMAL AND HYDRODYNAMIC INTERACTIONS BETWEEN A LIQUID DROPLET AND A FLUID INTERFACE

A Thesis
Presented to
The Academic Faculty

by

Edwin F. Greco

In Partial Fulfillment
of the Requirements for the Degree
Doctor of Philosophy in the
School of Physics

Georgia Institute of Technology
April 2008

THERMAL AND HYDRODYNAMIC INTERACTIONS BETWEEN A LIQUID DROPLET AND A FLUID INTERFACE

Approved by:

Professor Roman Grigoriev, Advisor
School of Physics
Georgia Institute of Technology

Professor Daniel Goldman
School of Physics
Georgia Institute of Technology

Professor Michael Schatz
School of Physics
Georgia Institute of Technology

Professor Minami Yoda
School of Mechanical Engineering
Georgia Institute of Technology

Professor Predrag Cvitanović
School of Physics
Georgia Institute of Technology

Date Approved: November 30th, 2007

For my brother

Always loved, never forgotten.

ACKNOWLEDGEMENTS

If the faculty senate suddenly decided to award merit badges for patience, my advisor (Dr. Roman Grigoriev) would be at the top of the list of recipients. As a graduate student I have tested his patience time and again with the same result, a small sigh followed by another attempt to mold me into a respectable physicist. As a mentor, he has taught me how to tease the essential physics out of the most difficult problems and how to effectively communicate with my peers. In short, he has been the best advisor that a graduate student such as myself could ask for and I am forever indebted to him.

Of course, I must also acknowledge that without the support of my family I would never have survived graduate school. My wife, Elizabeth, has been my confidant and most ardent supporter. I am ever thankful for her love and enduring confidence in my ability to succeed. I would also like to acknowledge my in-laws, Al and Kathy, ever ready to pitch in and make my life a little easier and my parents, Vicki and Rick, who have always fostered a curiosity in me and a desire to understand why.

I would also like to acknowledge my friends here at Tech. Whether they realize it or not, they have all shared a part in shaping my graduate education. A special thanks to: Andreas Handel and Kapil Krishin for making sure my research efforts got off on the right foot, Vivek Sharma for our long discussions about interfacial phenomena, Daniel Borrero and Jonathan Apple for tirelessly proof reading several edits of my thesis, and John Widloski for introducing me to the wonders of southern Utah and "Country Classics." Finally, a special acknowledgment to Neeraj Kothari, a true friend throughout graduate school that over the years became like a brother to me. I am ever thankful for the many blessings you have all bestowed upon me.

TABLE OF CONTENTS

LIST OF TABLES

LIST OF FIGURES

SUMMARY

The research presented in this thesis was motivated by the desire to understand the flow field within temperature driven droplets which serve as an alternative implementation of microfluidic devices. We investigate the dynamics of a droplet migrating along the surface of another fluid due to interfacial surface tension gradients. The quantitative analysis of the flow field presented in this thesis provides the first known solution for the velocity field in a migrating droplet confined to an interface.

The first step towards gaining insight into the flow field was accomplished by using the method of reflections to obtain an analytical model for a submerged droplet migrating near a free surface. The submerged droplet model enabled the analysis of the velocity field and droplet migration speed and their dependence on the fluid properties. In general, the migration velocity of a submerged droplet was found to differ substantially from the classic problem of thermocapillary migration in an unbounded substrate.

A boundary-collocation scheme was developed to determine the flow field and migration velocity of a droplet suspended at the air-substrate interface. The numerical method was found to produce accurate solutions for the velocity and temperature fields for most parameters. This numerical scheme was used to judge the accuracy of the flow field obtained by the submerged droplet model. The model was also tested using parameter values taken from an experimental device. It was determined that the submerged droplet model captured most of the flow structure within the microfluidic droplet. However, for other choices of parameters, agreement between the two methods was lost. In this case, the numerical scheme was used to uncover novel flow structures.

CHAPTER I

INTRODUCTION

Small bubbles and drops affect many processes and products by virtue of their presence and mobility. Emulsions, suspensions of drops of one liquid in another, are routinely studied in the food and cosmetic industry for improving consumer products. Likewise, the basic science of the coalescence and breakup of ink droplets is of paramount importance to the design of new inkjet technologies. Even in the microgravity environment of space, the study of bubbles and drops has become essential for the development of liquid fuel storage, life support devices and other fluid management systems (for a comprehensive review refer to Ref. [43]). In the past decade there has been a new wave of interest in the study of small droplets due to the emerging field of microfluidics and other Lab-on-a-chip technologies [41].

Microfluidic devices promise to miniaturize many chemical and biological protocols, such as chemical synthesis and biological assays, to make them programmable and repeatable using a single device (chip) of the size of a few square centimeters. The advantages of a microfluidic device include: a decrease in the size of fluid samples, parallelization of simple laboratory processes, low cost of operation, and an increase in operational throughput. These devices are currently used for designing and testing of new pharmaceuticals, detection of environmental pollutants, and in the design of DNA microarrays that are used to detect the presence of proteins in biological samples.

Digital microfluidic devices are a new breed of microfluidic devices that transport, merge, mix, and analyze discrete fluid volumes (drops). An advantage over

microfluidic devices, which use continuous flow is that individual droplets may be independently manipulated in an open environment (e. g. sandwiched between two glass plates or floating on a fluid substrate). Manipulation of droplets is often achieved by pressure gradients, induced variations in surface tension at the droplet surface or sometimes by focused acoustic fields (ultrasound). The Marangoni effect, fluid flow induced by surface tension gradients, is a popular choice for manipulating droplets in digital microfluidic devices. A common practice for achieving flow is through a process known as electrowetting on dielectric. In this process, force gradients are induced with electric fields for a droplet sandwiched between two hydrophobic glass plates. Control is provided by an array of programmable electrodes covering the glass plates.

While investigating the control and manipulation of thin films, Garnier, Schatz and Grigoriev [9] first proposed an optically controlled digital microfluidic device that would use lasers to induce temperature gradients near small droplets floating at the surface of an aqueous substrate. Throught this thesis these droplets will be referred to as interfacial droplets, since they are floating at the air-substrate interface as in Fig. 1. The follow-up experimental study by Grigoriev, Sharma, and Schatz [11] demonstrated the feasibility of this idea with a prototype of an optically controlled digital microfluidic device. In this device, the thermal gradients could be used for both transport and mixing inside millimeter to micron size droplets.

The main advantage of an optically controlled microfluidic device is its relative simplicity when compared with the methods that utilize electrowetting. Droplets are simply injected into the open substrate and driven in any desired manner by the control of a laser beam. No dielectric coatings or patterned electrodes are needed on the container. Furthermore, imaging is straightforward; CCD microscopes are pointed at the interfacial droplet and can be made to follow the droplet by means of a translation stage.

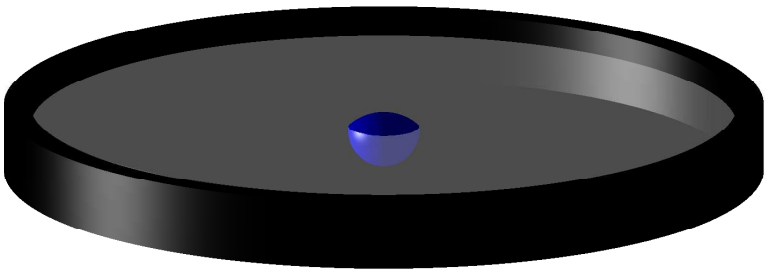

Figure 1: A droplet floating in an aqueous substrate is called an interfacial droplet because it is confined to the interface between two fluids. The casual observer is probably already familiar with these droplets from day-to-day life; such as in salad dressing and soups.

Regardless of the method of droplet manipulation, several challenges remain in the development of digital microfluidic devices. One such challenge is the efficient mixing inside the small droplets of a microfluidic device. When a slow moving droplet becomes very small (i. e., its radius is of the order of a few hundred micrometers or less), its flow field becomes very laminar (smooth). Such a flow removes the possibility of mixing due to turbulence, which is a common method of mixing two fluids on a macroscopic scale. Though very small, such droplets are not small enough for diffusion to significantly contribute to mixing in a short period of time (on the order of seconds). For example, it would take approximately 100 minutes for a passive fluid tracer $0.5\mu m$ in diameter to diffuse across a $100\mu m$ diameter quiescent water droplet.

To achieve rapid mixing by a laminar flow, it becomes necessary to implement a stirring mechanism within the droplet. One such stirring mechanism is chaotic advection, which describes the complex motion of a passive tracer advected in a laminar flow. This complex motion can be visualized as stretching and folding of the trajectories of passive tracers within the droplet. Much like the kneading of dough homogenizes the concentration of yeast, chaotic advection serves as a stirring mechanism; reducing the distance between mixed and unmixed portions of the droplet. A

quantitative description of mixing by chaotic advection requires an accurate knowledge of the trajectories allowed by the flow field inside the droplet.

The primary motivation for the research presented in this thesis is the desire to achieve efficient mixing in a novel digital microfluidic device by characterizing the flow field inside interfacial droplets. Grigoriev [10] and Vainchtein *et al.* [45] have made significant progress on thermocapillary driven mixing in droplets. In both of these studies the hydrodynamic interaction between the droplet and the air-substrate interface were neglected. Instead they considered the more idealized problem of a droplet in an unbounded substrate. A detailed, quantitative description of the flow field for interfacial droplets has not been previously formulated.

The first step towards finding an accurate solution for the flow inside interfacial droplets is to determine the asymptotic flow in the substrate in which they float. An analysis of the flow in the substrate is given in Chapter 2 for large aspect ratio layers. While such an analysis is not new, many of the governing equations, boundary conditions and parameter definitions determined in Chapter 2 will be used through the thesis.

In Chapter 3 of this thesis, an analytical procedure is derived for computing the velocity field of a droplet submerged near the air-substrate interface. The model successfully accounts for the thermal and hydrodynamic interaction between the droplet and air-substrate interface. This is accomplished by using the method of reflections. In an effort to gain a better understanding of what effect the air-substrate interface has on a submerged droplet, the dependence of the migration velocity of the droplet on the fluid parameters is also scrutinized.

In Chapter 4 of this thesis a numerical scheme, based on boundary collocation, is developed. This scheme is employed to determine the flow field for the more complex situation where the droplet resides at the air-substrate interface. The numerical computation of the flow field and migration velocities will allow us to gauge the accuracy

of the analytical model found by the method of reflections. In Chapter 5 predictions for the flow field and migrations velocities are made from both models. The impact of these findings, and their implications for efficient mixing in the microfluidic device of [11], are discussed in the concluding chapter. Before beginning Chapter 2 a brief introduction into the thermocapillary effect is given below. The reader already familiar with this phenomenon may wish to skip ahead.

1.1 The Thermocapillary Effect

For a liquid droplet suspended in an immiscible fluid substrate, the interfacial surface tension of the droplet is temperature dependent. Changes in the temperature at the interface will therefore result in surface tension gradients. These gradients generate a surface stress which is then transmitted to the fluid on either side of the interface by viscous dissipation. This results in the movement of fluid within and around the liquid droplet, a phenomenon known as the thermocapillary effect. This effect has been extensively studied for the last fifty years.

Under appropriate conditions, the collective movement of fluid both in and around the droplet can result in the transport of the droplet within the substrate. When the gradient in surface tension is caused by temperature gradients in the fluid, the resulting movement of the droplet is known as thermocapillary migration. The dependence of surface tension on temperature has been experimentally determined to be linear over a broad range of temperatures for many fluids. For most fluids, an increase in temperature causes a decrease in the surface tension. As a result, an isolated droplet will be observed to migrate to regions of warmer fluid (Fig. 2).

The first published investigation of thermocapillary migration dates back almost fifty years to the work by Young, Goldstein, and Block [50], who observed and analyzed air bubbles trapped in silicon oil under the effect of a constant temperature gradient. They discovered that the migration velocity depends linearly on both the

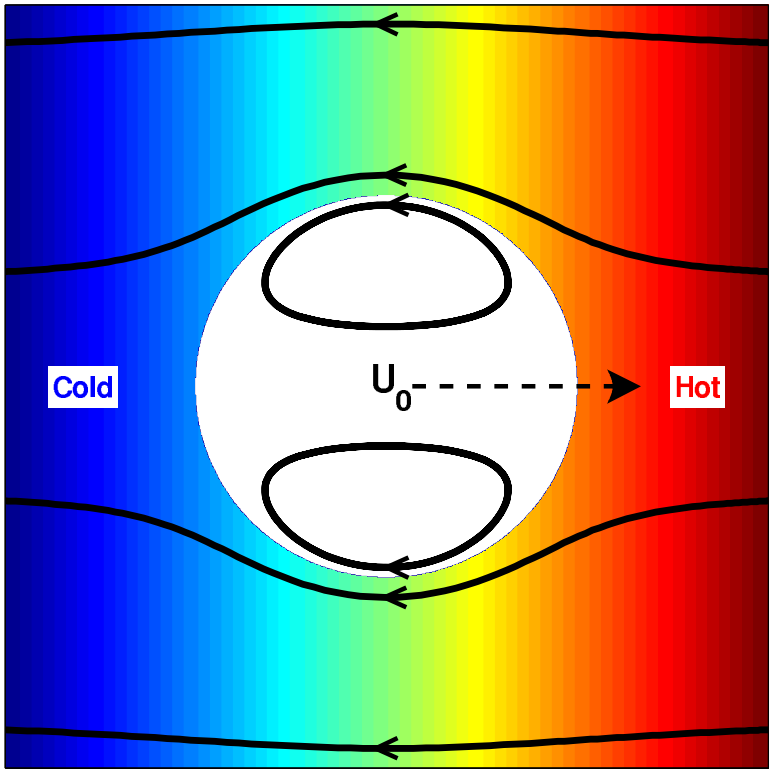

Figure 2: Thermocapillary migration of a liquid droplet (white) in a constant temperature gradient. The black lines indicate the direction of the flow as seen in the reference frame of the drop. U_0 is the migration velocity of the droplet.

bubble radius, and the imposed temperature gradient. It was also demonstrated that by aligning the temperature gradient with gravity, the migration of the bubble could be arrested or even reversed. In addition to these observations, a steady-state analytical solution was found for the velocity field and migration velocity in the limit of small Reynolds and thermal Péclet numbers. This solution was determined to be in good agreement with the experimental observations of a gas bubble. The analytical result was later shown, experimentally, to also accurately describe the thermocapillary migration of immiscible liquid droplets [19, 3].

More recent studies have concentrated on the experimental verification of the predicted migration velocity for a droplet in a low gravity environment [37, 44, 31, 48, 12, 25]. In many practical situations a small bubble or drop will not move in isolation.

Changes in the migration velocity due to neighboring bubbles or drops [28, 47, 46, 30] and solid or free boundaries[21, 27, 26, 4, 24, 6] have also been extensively studied. For a comprehensive review of these topics, the interested reader is referred to the excellent book by Subramanian and Balasubramanian [42].

There has been very little attention given to the motion of interfacial drops in a temperature gradient. Rybalko, Magome and Yoshikawa have observed the motion of an interfacial droplet directly heated with a laser beam [35]. A coarse image of the velocity field inside the droplet was reconstructed using particle-image velocimetry, and the velocity of thermocapillary migration was measured as a function of the laser power. The direction of the droplet motion was shown to reverse when the heating was switched from the top of the droplet to the bottom.

While not dealing with temperature gradients, there have been at least two studies that examined interfacial droplets in other settings. The only quantitative study of a flow field for interfacial droplet was undertaken by Smith, Ottino and De la Cruz [38], who numerically analyzed the effect of a simple shear flow on a two-dimensional interfacial drop with constant surface tension. They discovered that the interior flow pattern inside the droplet was topologically similar to that of a spherical droplet in an unbounded fluid. In addition, the droplet was observed to pinch off from the confining interface for large shear rates.

The other quantitative study of interfacial droplets focused on the shape dynamics of a liquid lens (i. e., interfacial drop) that was spreading out across a shallow liquid layer. As a result of the spreading, only very slender drops were considered by Craster and Matar [7]. Their analysis used the lubrication approximation to derive a set of differential equations for the time evolution of the droplet shape. In this limit the velocity field was not explicitly obtained as part of their solution, even though it could have been reconstructed from the thickness evolution.

CHAPTER II

FLOW IN A RECTANGULAR LIQUID LAYER

2.1 Introduction

In the optically controlled microfluidic device of Grigoriev, Sharma and Schatz [11], small droplets floating on a liquid substrate are manipulated by heating the substrate with a laser. Analytically modeling the complicated problem of a laser sheet heating a liquid layer is wrought with many difficulties. A much more tractable problem is one where the temperature gradient at the free surface is generated by maintaining the end walls of the container at different, fixed temperatures. In this chapter, the flow induced by such a system is determined. The solution for this flow is further used as the asymptotic flow for the submerged drop system of Chapter 3 and the interfacial drop system of Chapter 4.

Fig. 3 shows a cross section of a large aspect-ratio liquid layer. The difference in temperatures of the two end walls is assumed sufficiently small to allow the temperature and velocity fields in the substrate to reach a steady-state. Additionally, all physical parameters of the system are assumed temperature invariant, with the exception of surface tension. The height of the substrate is assumed fixed at $z = 0$ and the covering fluid is taken to be air. As an idealization, the viscosity and thermal conductivity of this covering fluid is taken to be zero. The free surface and the bottom of the container are thermally insulated. Under these conditions, analysis of the flow can be restricted to that of the liquid layer below the air-substrate interface.

The extent of the liquid in the direction out of the page is taken to be sufficiently large such that flow can be treated as two dimensional. Furthermore, the height of

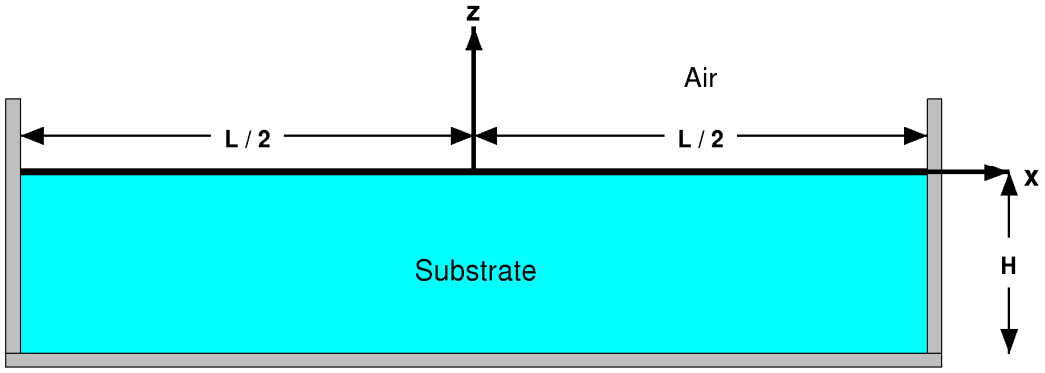

Figure 3: A view of liquid layer in the (x, z) plane (not to scale). We take the z axis to be vertical and the x axis to point in the direction of the temperature gradient.

the container H is taken to be much smaller than the length L so that the ratio

$$\zeta = \frac{H}{L} \tag{1}$$

is much less than unity. Without loss of generality the temperature of the right end wall T_r is assumed greater than the temperature of the left end wall T_l.

The treatment of the flow field presented here has been known in the literature for some time. A steady-state analysis in a similarly defined liquid layer can be found in Levich [22] and in the more recent book by Subramanian and Balasubramanian [42]. While not new, the results of this chapter are not superfluous. Aside from being useful as asymptotic flows in later chapters, the analysis in this chapter will be instrumental in defining recurrent equations and quantities.

2.2 Governing Equations and Boundary Conditions

Contributions to the temperature field from viscous dissipation, radiant transport of energy and heat sinks or sources are neglected. Evolution of the temperature field in the liquid layer is then governed by an advection-diffusion energy equation

$$\frac{\partial T}{\partial t} = \kappa \nabla^2 T - \mathbf{V} \cdot \nabla T, \tag{2}$$

where T is the temperature field, κ is the thermal diffusivity and $\mathbf{V}$ is the velocity in the liquid layer. The velocity field is governed by the Navier-Stokes equation for an incompressible fluid

$$\rho\frac{\partial \mathbf{V}}{\partial t} = \mu\nabla^2\mathbf{V} - \rho\left(\mathbf{V}\cdot\nabla\right)\mathbf{V} - \nabla p, \tag{3}$$

$$\nabla\cdot\mathbf{V} = 0, \tag{4}$$

where ρ is the the density of the liquid, μ is the dynamic viscosity and p is the pressure.

The boundary conditions for the temperature field at the air-substrate interface and the bottom of the container require the heat flux to vanish

$$\left.\frac{\partial T}{\partial z}(x,z)\right|_{z=0} = \left.\frac{\partial T}{\partial z}(x,z)\right|_{z=-H} = 0. \tag{5}$$

In addition, the temperature field must be continuous at the left and right container end walls

$$T\left(-\frac{L}{2},z\right) = T_l \tag{6a}$$

$$T\left(\frac{L}{2},z\right) = T_r. \tag{6b}$$

Boundary conditions on the velocity field at the container surface require the velocity to satisfy a no-slip constraint

$$\mathbf{V}|_{x=-\frac{L}{2}} = \mathbf{V}|_{z=-H} = \mathbf{V}|_{x=\frac{L}{2}} = 0. \tag{7}$$

At the air-substrate interface the normal velocity must vanish and the tangential component of the stress must balance the surface tension gradient at the air-substrate interface

$$\mathbf{V}\cdot\hat{\mathbf{z}}\big|_{z=0} = 0, \tag{8}$$

$$\hat{\mathbf{z}}\cdot\boldsymbol{\Sigma}\times\hat{\mathbf{z}}\big|_{z=0} = \nabla\sigma_p\times\hat{\mathbf{z}}. \tag{9}$$

Here, $\boldsymbol{\Sigma}$ is the stress tensor field and σ_p is the interfacial surface tension of the planar interface. Surface tension is assumed to vary linearly with temperature

$$\sigma_p(T) = \bar{\sigma_p} + \sigma_p'(T - T_0), \tag{10}$$

where $\bar{\sigma_p}$ is the value of the surface tension at the reference temperature T_0 (taken as the temperature at the origin) and σ_p' is the corresponding temperature coefficient. The normal component of the stress boundary condition (9) was omitted. This omission will be discussed in the next section following the definition the capillary number.

2.3 Important Scales

To reduce the number of parameters describing the problem to a minimum, the governing equations and boundary conditions are first nondimensionalized. Lengths in the x direction are scaled by L and lengths in the z direction are scaled by H. Temperature is scaled by subtracting the average of the two end wall temperatures and dividing by their difference. The $\hat{\mathbf{x}}$ component of the velocity is scaled by

$$v_0 = \frac{(-\sigma_p')(T_r - T_l)\zeta}{\mu}, \tag{11}$$

and the $\hat{\mathbf{z}}$ component is scaled by $v_0\zeta$. Both pressure and stresses are scaled by

$$\Sigma_0 = \frac{\mu v_0 L}{H^2}. \tag{12}$$

The characteristic length scale on which the surface tension $\sigma_p(T(x))$ varies is given by

$$l_0 = -\frac{\bar{\sigma_p}}{\sigma_p'\Theta}, \tag{13}$$

where

$$\Theta = \frac{T_r - T_l}{L}. \tag{14}$$

The negative sign in Eq. (13) reflects the fact that for most fluids the change in surface tension with temperature is negative. Any solution for the temperature or velocity fields will only be valid at scales of order l_0. This places an additional constraint on the maximum allowable length of the container L.

With these chosen scales, the governing equation for temperature (2) simplifies to:

$$\zeta^2 \frac{\partial^2 T}{\partial x^2} + \frac{\partial^2 T}{\partial z^2} = \zeta^2 Pe \left(\mathbf{V} \cdot \nabla T \right), \tag{15}$$

where the thermal Péclet number

$$Pe = \frac{v_0 L}{\kappa}, \tag{16}$$

is a measure of the relative strength of convective transport of energy compared to molecular transport (heat conduction). In the above scaled governing equation and in all subsequent equations, the same symbols for coordinates and fields have been reused.

The governing equations for the scaled velocity field are given by

$$\zeta^2 \frac{\partial^2 V_x}{\partial x^2} + \frac{\partial^2 V_x}{\partial z^2} - \frac{\partial p}{\partial x} = \zeta^2 Re \left(\mathbf{V} \cdot \nabla V_x \right), \tag{17a}$$

$$\zeta^4 \frac{\partial^2 V_z}{\partial x^2} + \zeta^2 \frac{\partial^2 V_z}{\partial z^2} - \frac{\partial p}{\partial z} = \zeta^4 Re \left(\mathbf{V} \cdot \nabla V_z \right), \tag{17b}$$

The subscript on the velocity field is used to distinguish a component of the field (e. g., $\mathbf{V} \cdot \hat{\mathbf{z}} = V_z$). The dimensionless parameter Re is the Reynolds number

$$Re = \frac{\rho v_0 L}{\mu}, \tag{18}$$

which gauges the relative contribution of inertial and viscous terms in the Navier-Stokes equation (3). Most of the boundary conditions on the temperature and velocity fields remain unchanged. Exceptions are the heat flux constraint (6) and stress balance (9) which are simplified to

$$T\left(-\frac{1}{2}, z\right) = -\frac{1}{2}, \tag{19a}$$

$$T\left(\frac{1}{2}, z\right) = \frac{1}{2}, \tag{19b}$$

and

$$\left(\frac{\partial V_x}{\partial z} + \frac{\partial T}{\partial x} - \zeta^2 \frac{\partial V_z}{\partial x} \right) \Bigg|_{z=0} = 0. \tag{20}$$

In the special limit when the Reynolds and Péclet numbers are of $\mathcal{O}(1)$ and $(\zeta \to 0)$, the velocity and temperature fields are decoupled. In this case, they may be computed independently of each other.

2.4 A Solution for the Temperature Field

In the limit $(\zeta \to 0)$ the governing equation for temperature (15) coupled with the boundary conditions (5) produces the trivial solution $T = 0$. This solution does not satisfy the temperature constraints at the end walls. Kevorkian and Cole [16] determined that the constant difference in end wall temperatures requires an expansion of the temperature field of the form

$$T = T_1(x) + \zeta^2 T_2(x, z). \tag{21}$$

Substituting this expansion into Eq. (15) and once again taking the limit of vanishing aspect ratio the following integrated form of the governing equation is obtained

$$\frac{\partial T_2}{\partial z} = -\frac{\partial^2 T_1}{\partial x^2} z + Pe \frac{\partial T_1}{\partial x} \int_0^z V_x(x, z')dz' + c_0. \tag{22}$$

Applying the condition of zero heat flux at the air-substrate interface, the unknown constant c_0 in Eq. 22) is found to be zero. Evaluating Eq. (22) at the bottom of the container $(z = -1)$ and using an integrated form of the incompressibility condition (4)

$$\int_0^{-1} \int_{-\frac{1}{2}}^{x} (\nabla \cdot \mathbf{V})\, dx'dz' = \int_0^{-1} V_x(x, z')dz' = 0, \tag{23}$$

the function $T_1(x)$ is found to be a solution of Laplace's equation which is linear in x. Using boundary conditions (19), the final form of the scaled temperature field is found to be

$$T(x) = x. \tag{24}$$

This solution for the temperature field will be used to calculate the surface tension gradient at the air-substrate interface. It is this gradient which will determine the form of the velocity field.

2.5 A Solution for the Velocity Field

In the limit ($\zeta \to 0$) the governing equations for the velocity field are directly integrated. Applying the no-slip condition at the bottom of the container and substituting the solution for the temperature field into (20), the $\hat{\mathbf{x}}$ component of the velocity is given by

$$V_x(x,z) = \frac{1}{2}\frac{\partial p(x)}{\partial x}(z^2-1) - (z+1). \tag{25}$$

This velocity does not satisfy the boundary conditions at the end walls which is a consequence of the chosen length scales. To find the recirculating flow near the end walls, lengths would need to be re-scaled in a different way and a solution for the field in that region would need to be matched to the flow field far from the walls. Since the research of this thesis is entirely focused on small drops located near the origin, such an analysis is unnecessary here. The inquisitive reader may consult the work of Sen and Davis [36], which also included surface deformation of the liquid layer.

In place of the boundary conditions at the end walls, the incompressibility condition (23) is used to ensure zero volumetric flow rate in the layer. Substitution of (25) into (23) yields the pressure field

$$p(x) = -\frac{3}{2}x. \tag{26}$$

By direct substitution and integration of the incompressibility condition the $\hat{\mathbf{z}}$ component of the velocity field was found to be zero. Approximate streamlines and level sets for the velocity field given in Fig. 4. Throughout this thesis, the magnitude of a field will always be represented by color and scaled so that the minimum is blue and the maximum is red.

2.6 Conclusions

Though the aspect ratio of the container was taken to be infinite, the solution for the velocity field required some knowledge of the shape of the container (i. e. that it is

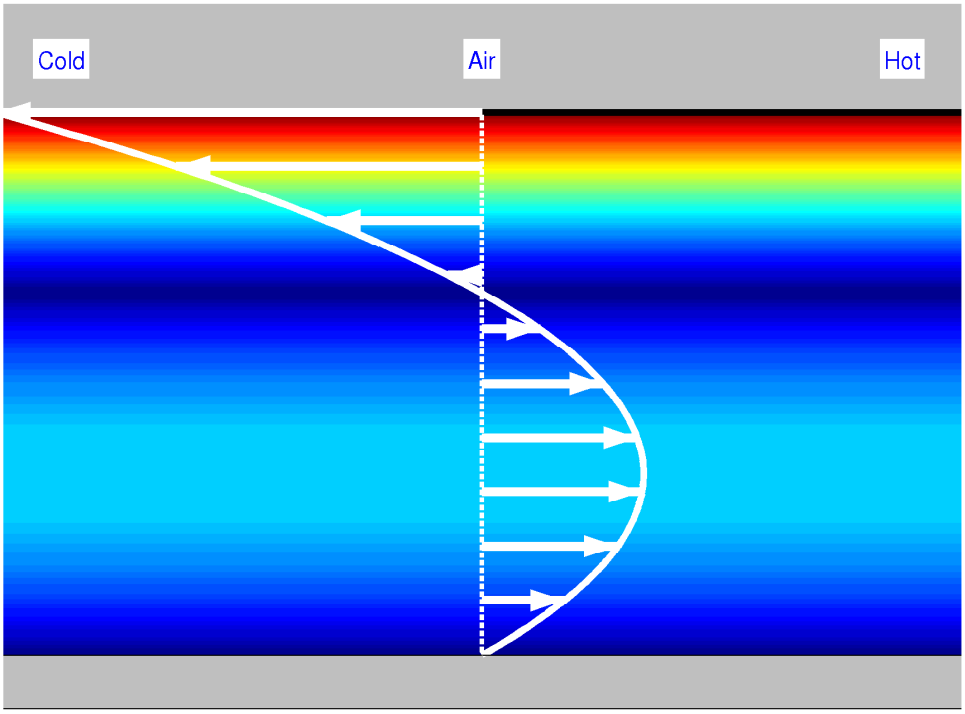

Figure 4: Streamlines and level sets of the scaled velocity field in the liquid layer. The flow was found to be a non-uniform shear flow with maximum velocity at the air-substrate interface

not infinite). This was accomplished by incorporating a zero volumetric flow rate in the substrate. If such a constraint had not been enforced, V_x would have been linear in z and the velocity at the air-substrate interface would have been four times larger. For a small droplet placed near this interface, consideration of zero volumetric flow rate is crucial in correctly determining the droplet migration velocity.

CHAPTER III

MOTION OF A SPHERICAL DROPLET NEAR A PLANE SURFACE

3.1 Introduction

This chapter deals with the motion of a fluid droplet in an immiscible fluid substrate moving parallel to and beneath a free surface. The substrate and droplet are subject to an imposed temperature field uniform far from the drop. Several efforts have been made to study the thermocapillary migration of a droplet normal to an interface. In comparison, limited attention has been given to the case of a droplet migrating parallel to the free surface. The analysis presented here was motivated by the need for an analytical model of the flow field inside the droplet. This model will be used to study the mixing properties of the optically controlled microfluidic device discussed in detail during the introduction of this thesis.

Meyyappan and Subramanian [27] determined the flow field and migration velocity numerically for the case of a gas bubble migrating parallel to a plane solid wall in a constant temperature gradient and found that the wall retarded the thermocapillary migration of the droplet. Chen [6] used the method of reflections to obtain an analytical result for the migration velocity and substrate flow field. Chen allowed the planar interface of the substrate to be either a plane solid wall or a free surface. Unfortunately, Chen's results were based, incorrectly, on the use of an approximation to the exterior velocity field derived by Anderson [2] in the study of multiple droplet interactions. In addition, Chen did not account for the variation in the interfacial tension with temperature at the free surface and did not provide results for the interior velocity field. The solution for the flow field computed in this chapter represents

the first correct solution to the full problem.

The research presented in this chapter extends the previous analysis of a submerged droplet by Grigoriev [10] by taking into account the thermal and hydrodynamic interactions between the droplet and the planar interface. In [10], the interactions between the droplet and the planar interface were not taken into account. This was due to the focus of the study on the mixing properties of the interior flow field in the limit when the droplet is very far from the planar interface and was the minimal model necessary to explain mixing. The results presented here provide an improvement on the model derived in [10] by considering the case of a droplet moving near the free surface.

This chapter begins with the derivation of the governing equations and boundary conditions that determine the flow field of a submerged droplet. Results for the migration velocities and flow structures are then analyzed for a range of physical parameters. In Chapter 5 the submerged droplet model derived here will be put to the test against a numerical solution with parameters values taken from experiment [11].

3.2 Governing Equations and Boundary Conditions

Consider a small immiscible droplet that has been placed a distance d below the air-substrate interface in a rectangular liquid layer such as the one considered in Chapter 2. For convenience, the origin of this system has been moved to the center of the droplet which is illustrated in Fig. 5. The temperature and velocity fields are governed by the energy and incompressible Navier-Stokes equations, (2) and (3), respectively.

Motivated by the study of micron-size droplets in gentle temperature gradients, we will assume that in the fluid surrounding the droplet and inside the droplet all velocities are small enough for convective momentum, and energy transport to be

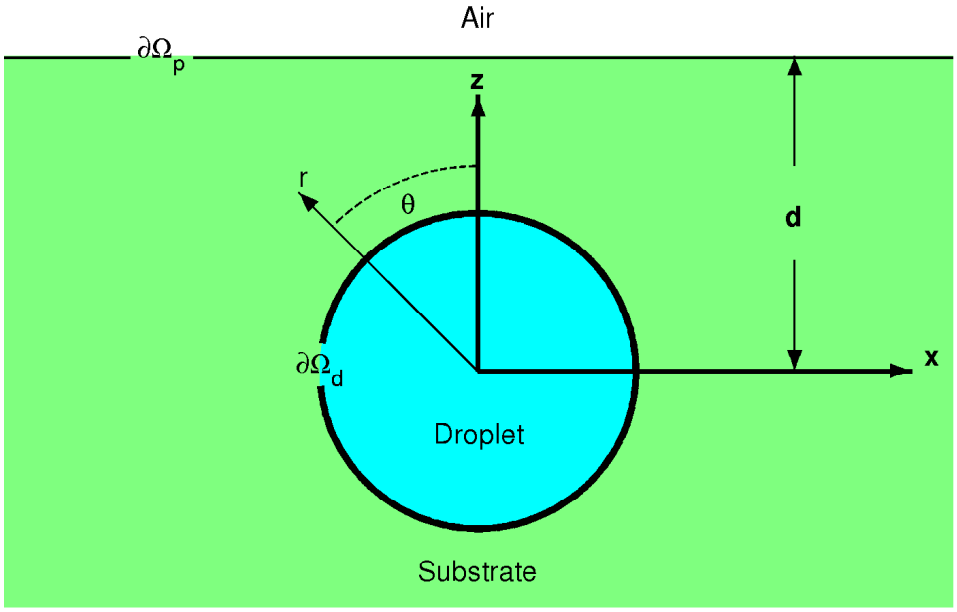

Figure 5: A view of the submerged drop in the (x, z) plane (not to scale). We take the z axis to be vertical and the x axis to point in the direction of the temperature gradient.

negligible. In the limit of vanishing thermal Péclet numbers, $Pe = 0$, the temperature field in each fluid must satisfy Laplace's equation

$$\nabla^2 T_i = 0, \tag{27}$$

where the subscript designates the i^{th} fluid. Air is designated by fluid 1, the substrate by fluid 2 and the droplet by fluid 3. In the limit of vanishing Reynolds numbers, $Re = 0$, the velocity field in the substrate and droplet are governed by the Stokes equation, subjecte to the incompressibility condition

$$\mu_i \nabla^2 \mathbf{V_i} = \nabla p_i, \tag{28a}$$

$$\nabla \cdot \mathbf{V_i} = 0, \tag{28b}$$

As in Chapter 2, contributions to the temperature and flow field from fluid 1 (air) are assumed negligible and analysis is restricted to fluids 2 (the substrate) and 3 (the droplet).

Boundary conditions on the temperature and velocity field at the air-substrate interface remain unchanged from the liquid layer analysis of Section 2.2: the heat flux must vanish (5); the normal component of the velocity field must vanish (8); and the tangential stress must balance the gradient of surface tension at the interface (9). At the droplet surface, boundary conditions require the continuity of the temperature field and the heat flux

$$(T_2 - T_3)|_{\partial\Omega_d} = 0, \tag{29a}$$

$$(k_2 \nabla T_2 - k_3 \nabla T_3) \cdot \hat{\mathbf{n}}|_{\partial\Omega_d} = 0, \tag{29b}$$

where k_i is the thermal conductivity and $\hat{\mathbf{n}}$ is the normal vector pointing from fluid 1 into fluid 2. Furthermore, the normal component of velocity at the droplet surface must vanish and the tangential component of velocity must be continuous

$$V_2 \cdot \hat{\mathbf{n}}|_{\partial\Omega_d} = V_3 \cdot \hat{\mathbf{n}}|_{\partial\Omega_d} = 0, \tag{30a}$$

$$(\mathbf{V}_2 - \mathbf{V}_3) \times \hat{\mathbf{n}}|_{\partial\Omega_d} = 0, \tag{30b}$$

where the position of the interface is assumed stationary (the validity of this assumption is discussed in Section 3.4). Finally, the jump in the tangential and normal components of the stress $\mathbf{\Sigma}$ must balance the surface tension gradient and curvature at the substrate droplet interface.

$$\hat{\mathbf{n}} \cdot (\mathbf{\Sigma}_2 - \mathbf{\Sigma}_3) \times \hat{\mathbf{n}}|_{\partial\Omega_d} = -\nabla\sigma_d \times \hat{\mathbf{n}}, \tag{31a}$$

$$\hat{\mathbf{n}} \cdot (\mathbf{\Sigma}_2 - \mathbf{\Sigma}_3) \cdot \hat{\mathbf{n}}|_{\partial\Omega_d} = \sigma_d \cdot (\nabla \cdot \hat{\mathbf{n}}). \tag{31b}$$

As in the liquid layer analysis, all physical properties of the fluids have been assumed independent of temperature with the exception of surface tension. Surface tension at the droplet surface is also assumed to vary linearly with temperature.

$$\sigma_d(T) = \bar{\sigma_d} + \sigma_d'(T - T_0), \tag{32}$$

where $\bar{\sigma_d}$ is the value of the surface tension at reference temperature T_0 (the instantaneous temperature at the origin) and σ_d' is the corresponding temperature coefficient.

3.3 Flow Far From The Droplet

The introduction of a droplet of characteristic size r_0, small when compared with both l_0 (13) and the depth of the substrate H, will distort the temperature and velocity fields near the droplet. Far from the droplet (i. e. , for $r_0 \ll |\mathbf{x}| \lesssim l_0$) the fields are that of the liquid layer (found in Chapter 2). These fields are therefore well suited to serve as the solution for the fields far from the droplet. Dimensionalizing the temperature field (24) and velocity field (25) of the of the substrate yeilds:

$$T_2^\infty = T_0 + \Theta x, \tag{33}$$

$$V_2^\infty = \frac{\sigma_p' \Theta}{\mu_2} \left(\frac{3}{4H}(z-d)^2 + (z-d) + \frac{H}{4} \right) \hat{\mathbf{x}}, \tag{34}$$

where the ∞ superscript is used to designate these fields as asymptotic. For convenience, the reference frame is chosen to move at the steady-state migration velocity of the droplet. The symmetry of the system with respect to the y axis and the symmetry of the asymptotic fields (assuming constant d) implies that the droplet moves along the x axis. Switching to a reference frame moving with velocity $\mathbf{U_0} = U_0\hat{\mathbf{x}}$, the following boundary conditions are obtained

$$T_2 \to T_2^\infty, \qquad |\mathbf{x}| \to \infty, \tag{35a}$$

$$\mathbf{V}_2 \to \mathbf{V}_2^\infty - \mathbf{U_0}, \qquad |\mathbf{x}| \to \infty, \tag{35b}$$

In this reference frame all fluid-fluid interfaces are stationary. It now remains only to specify the hydrodynamic force on the droplet.

3.4 Important Scales and The Hydrodynamic Force

Solutions for the velocity and temperature fields far from the droplet are valid for small Reynolds and thermal Péclet numbers, which is usually the case when length and velocity scales are small. There are several such length and velocity scales characterizing this system. For the flow far from the droplet the characteristic scales are

H and v_0^∞, where

$$v_0^\infty = -\frac{\sigma_p' \Theta H}{4\mu_2} \tag{36}$$

is the asymptotic velocity field evaluated at the planar interface. Near the droplet the scales are r_0 and v_0, where

$$v_0 = -\frac{\sigma_d' r_0}{\mu_2}\Theta. \tag{37}$$

Using these scales for each fluid, the Reynolds numbers are defined as

$$Re_i = \frac{l_i v_i \rho_i}{\mu_i}, \tag{38}$$

and thermal Péclet numbers are defined as

$$Pe_i = \frac{l_i v_i \rho_i C_{p,i}}{k_i}. \tag{39}$$

In both definitions the respective values of the densities ρ_i, viscosities μ_i, thermal conductivities k_i, and heat capacities $C_{p,i}$ are used for each fluid. The corresponding length scales are $l_2 = H$, $l_3 = r_0$ and the velocity scales are $v_2 = v_2^\infty$, $v_3 = v_0$.

The variations in the length and velocity scales of different fluids mean that the Reynolds and Péclet numbers, in different fluids, can differ by orders of magnitude. For instance, even assuming all the densities, viscosities and temperature coefficients of surface tension are comparable, we find

$$\frac{Re_2}{Re_3} = \frac{1}{4}\frac{\rho_2}{\rho_3}\frac{\mu_3}{\mu_2}\frac{\sigma_{12}'}{\sigma_{23}'}\frac{H^2}{r_0^2} \sim \left(\frac{H}{r_0}\right)^2. \tag{40}$$

However, both v_0^∞ and v_0, and with them Re_i and Pe_i for each fluid, become arbitrarily small as the imposed temperature gradient Θ is reduced. Any requirement on the smallness of the dimensionless parameters can thus be completely justified in the limit of a small imposed temperature gradient.

Characterization of the droplet shape, and the effect of the droplet on the shape of the interface $\partial\Omega_p$, requires the introduction of additional nondimensional numbers.

In particular, these are the capillary and Bond number. For each fluid the capillary numbers are given by

$$Ca_i = \frac{\mu_i v_0}{\bar{\sigma}_i}, \qquad i = 2, 3 \tag{41}$$

where $\bar{\sigma}_2 = \bar{\sigma}_p$ and $\bar{\sigma}_3 = \bar{\sigma}_d$. Both capillary numbers are of the same order of magnitude for a typical case in which the surface tensions and viscosities of both fluids are comparable. The condition for the smallness of the capillary numbers is equivalent to the condition $l_0 \gg r_0$. For instance, for fluid 3

$$Ca_3 = \frac{-\sigma_d' r_0 \Theta}{\bar{\sigma}_d} = \frac{\sigma_d'}{\bar{\sigma}_d} \frac{\bar{\sigma}_p}{\sigma_p'} \frac{r_0}{l_0} \sim \frac{r_0}{l_0}. \tag{42}$$

Similarly, the Bond numbers are defined as

$$Bo_i = \frac{\rho_i g r_0^2}{\bar{\sigma}_i}, \qquad i = 2, 3, \tag{43}$$

where g is the acceleration due to gravity. The Bond numbers are also all of the same order of magnitude for fluids with comparable densities and surface tensions. For most fluids they become very small as the droplet size decreases (e. g., $Bo \sim 0.1$ for a 1 mm aqueous water droplet).

The position of the fluid interfaces, which determine both the droplet shape and the shape of the air substrate surface, are found by solving the normal stress balance equation (31b). In the limit ($Bo = Ca = 0$), and assuming the temperature variation to be small near the droplet (where the curvature $\nabla \cdot \hat{\mathbf{n}}$ is large), the normal component of the stress reduces to a constant pressure. As a consequence, both interfaces become surfaces of constant curvature. Since the air-substrate interface is flat far from the droplet, it has to be a horizontal flat plane $z = d$. Similarly, the droplet substrate interface will be spherical with radius r_0.

With the positions of the boundaries determined, the temperature and velocity fields can be found independently by solving (27) and (28). Having specified the position/shape of all free interfaces, it is not necessary to satisfy the normal stress

balance boundary condition (31b) at each interface. Furthermore, the boundary condition (7) at the solid bottom boundary is not explicitly enforced which is justified in the $H \gg r_0$ limit, where no-slip is sufficiently satisfied as a consequence of (35).

The steady-state assumption, which requires that the migration velocity be constant, determines that the total force on the droplet vanish.

$$\mathbf{f} = \mathbf{f}_{\text{body}} + \mathbf{f}_{\text{surface}} = 0. \tag{44}$$

In the $Bo = 0$ limit, the body force $\mathbf{f}_{\text{body}}$ is absent. The surface force is given by

$$\mathbf{f}_{\text{surface}} = \int_{\partial\Omega_d} \mathbf{\Sigma}_2 \cdot \hat{\mathbf{r}} dS. \tag{45}$$

The force constraint (44) closes the system of equations for the velocity fields, allowing the computation of the migration velocity $\mathbf{U_0}$ of the droplet relative to the solid bottom boundary.

To reduce the number of parameters describing the problem to a minimum, the governing equations and boundary conditions were nondimensionalized: lengths were scaled by r_0; temperature was scaled by subtracting the instantaneous temperature at the origin T_0 and dividing by the characteristic temperature scale Θr_0; velocities were scaled by the characteristic velocity of the droplet, v_0; stresses, including pressure, were scaled by the typical viscous stress $\Sigma_0 = -\sigma_d' \Theta$; viscosities, thermal conductivities, reference surface tensions, and temperature coefficients of surface tension were scaled by μ_2, k_2, $\bar{\sigma}_d$, and σ_d', respectively. The corresponding nondimensional quantities are summarized in Table 1. In addition to these parameters, there are three length scales of importance: the nondimensional temperature length scale $\lambda = l_0/r_0$; the scaled substrate depth $\chi = H/r_0$; and the scaled submerged depth of the droplet $\delta = d/r_0$.

Table 1: Dimensionless parameters describing thermocapillary migration of a submerged droplet subject to a horizontal temperature gradient.

	Fluid 2	Fluid 3
Viscosity	$\alpha_2 = 1$	$\alpha_3 = \mu_3/\mu_2$
Thermal conductivity	$\beta_2 = 1$	$\beta_3 = k_3/k_2$
Surface tension	$\gamma_{12} = \bar{\sigma}_p/\bar{\sigma}_d$	$\gamma_{23} = 1$
Temperature coefficient	$\tau_{12} = \sigma'_p/\sigma'_d$	$\tau_{23} = 1$

3.5 A Solution Procedure Using The Method of Reflections

The method of reflections provides an approximate solution to the Laplace's and Stokes equations, when considering an interaction between two objects. This procedure is outlined in the book by Happel and Brenner [13] for a case of two hydrodynamically interacting spheres. The same procedure, extended to the interaction between a sphere and infinite plane, was first used by Chen [6] for analyzing the motion of a droplet migrating due to surface tension gradients. An intuitive description of this procedure is provided below, and the solution for the temperature field is worked out in full detail in the following section.

The method of reflections permits a solution by adding corrections to successively satisfy the boundary conditions at one and then the other interface, instead of simultaneously satisfying boundary conditions at both interfaces. In the case of the droplet surface $\partial\Omega_d$ and the air-substrate interface $\partial\Omega_p$, this process will begin by choosing to first satisfy boundary conditions at $\partial\Omega_d$, called a reflection about the droplet. The solution, found using the general solution for Laplace's or Stokes equation, will satisfy boundary conditions everywhere except at $\partial\Omega_p$. The field exterior to the droplet is then reflected about interface $\partial\Omega_p$ by an appropriate transformation on the field external to the droplet. The transformation is chosen to exactly satisfy boundary conditions at $\partial\Omega_p$.

The field exterior to the droplet is updated by taking the linear superposition of the field satisfying boundary conditions at $\partial\Omega_d$ and its reflection about the air-substrate interface. In the case of the temperature and velocity fields, this is expressed analytically as

$$T_2 = T_2^0 + T_{out}^{1d} + T_{out}^{1p}, \tag{46a}$$

$$T_3 = T_{in}^{1d}, \tag{46b}$$

$$\mathbf{V_2} = \mathbf{V_2^0} + \mathbf{V_{out}}^{1d} + \mathbf{V_{out}}^{1p} - \mathbf{u}, \tag{46c}$$

$$\mathbf{V_3} = \mathbf{V_{in}}^{1d} - \mathbf{u}. \tag{46d}$$

where, the superscripts $1d$ and $1p$ stand for the 1^{st} reflection about the (d)rop and (p)lane interface respectively. The subscripts *in* and *out* distinguish the interior and exterior solutions for the temperature and velocity field, the general form of which is given later in the chapter. Any external fields, T_2^0 and $\mathbf{V_2^0}$, will either be identically zero or imposed *a priori*. All fields determined in the reference frame of the droplet which is migrating with a scaled velocity $\mathbf{u}$.

$$\mathbf{u} = \left(\frac{U_0}{v_0}\right)\hat{\mathbf{x}} = \mathbf{u}^{1d}. \tag{47}$$

Because the migration velocity is constant, only reflections from the surface of the droplet will contribute to the overall migration velocity.

The added contributions, T_{out}^{1p} and $\mathbf{V_{out}^{1p}}$, to the updated fields will not satisfy boundary conditions at the droplet surface. A new contribution (i. e., a reflection about the droplet surface) to the interior and exterior fields is required to correct for this. It is not possible to exactly satisfy the boundary conditions at $\partial\Omega_d$ using a finite number of terms in the general solution. To calculate the reflection an approximation to T_{out}^{1p} and $\mathbf{V_{out}^{1p}}$ is made at the droplet surface that allows the boundary conditions at $\partial\Omega_d$ to be satisfied up to an arbitrary order in the small parameter ϵ. This results in a correction, expressed as a superposition of a finite number of terms of the general solution.

Specifically, the approximation to reflections from $\partial\Omega_p$ is found by locally expanding each reflection in powers of ϵ, where:

$$\epsilon = \frac{1}{2\delta}. \tag{48}$$

Near the surface of the droplet $r = \mathcal{O}(1)$. For values of $\delta \gg 1$, the expansion parameter ϵ will be small enough that the series can be truncated with minimal error. The boundary conditions are then evaluated using the truncated field and a new contribution to the interior and exterior field (i. e. reflections about $\partial\Omega_d$) is found that satisfies the boundary conditions at the droplet surface. Since these boundary conditions were satisfied with truncated fields, some error still remains in the solution. This error is proportional to ϵ^N, where N is the the truncation order, and can be made arbitrarily small for small ϵ by increasing N.

The new contribution to the exterior field will not satisfy the boundary conditions at the interface $\partial\Omega_p$. This field contribution must be reflected and the entire procedure repeated, with alternating reflections about each interface, until the lowest order term in the expansion of the last reflection is equal to the truncation order. At this point, the combined contributions to the velocity field will simultaneously satisfy boundary conditions at $\partial\Omega_p$ exactly and up to the truncation order of the expansion at $\partial\Omega_d$.

This method of reflections is only useful for obtaining a solution if the new contributions to the total field become successively smaller with each reflection. In the next section, the order of the lowest term in the expansion of the reflection about $\partial\Omega_p$ is shown to grow with each successive reflection as a consequence of the decay rate of the exterior field. So once the truncation order for the field is specified, the process of successive reflections will end after a finite number of reflections.

The final result for the field is given by a linear superposition of each reflection

about $\partial\Omega_p$ and $\partial\Omega_d$. In the case of the temperature and velocity fields, this is expressed analytically as

$$T_2 = T_2^0 + \sum_{n=1}^{N_r} \left(T_{out}^{nd} + T_{out}^{np} \right), \tag{49a}$$

$$T_3 = \sum_{n=1}^{N_r} T_{in}^{nd}, \tag{49b}$$

$$\mathbf{V_2} = \mathbf{V_2^0} + \sum_{n=1}^{N_r} \left(\mathbf{V_{out}^{nd}} + \mathbf{V_{out}^{np}} \right) - \mathbf{u}, \tag{49c}$$

$$\mathbf{V_3} = \sum_{n=1}^{N_r} \mathbf{V_{in}}^{nd} - \mathbf{u}. \tag{49d}$$

Here the superscripts nd and np stand for the n^{th} reflection, and N_r is the total number of reflections and is determined required to satisfy boundary conditions up to ϵ^N. Each element in the sum is given by general solution for the fields governing equation. The coefficients of that solution are found independently by satisfies boundary conditions at the respective interface. Similarly, the steady-state migration velocity of the droplet is given by

$$\mathbf{u} = \sum_{n=1}^{N} \mathbf{u}^{nd}. \tag{50}$$

Since the specification of the truncation order only determines the total number of required reflections, the field may be approximated to any reasonable order.

3.6 A Solution for the Temperature Field

Although the temperature field is not of direct interest, it is important for describing the relative magnitudes of thermocapillary stresses at the surfaces of the droplet and planar interface. Compared with the velocity field, the number of equations determining the temperature field are relatively small. This makes the temperature field an ideal test case for illustrating a solution procedure by the method of reflections. Moreover, since the solution procedure for the temperature and velocity fields are very similar, little modification is required to later solve for the velocity field.

The general solution to Laplace's equation (27), which governs the temperature field, is expressed in terms of spherical harmonics. The interior temperature must be bounded at the origin and the exterior temperature must be bounded at infinity. The temperature field must also be symmetric in y and antisymmetric in x, as determined by the geometry of the system and asymptotic boundary conditions. These constraints, coupled with the boundary condition (35a), yield a general solution for the nondimensional temperature field of the submerged drop system.

$$T_{out}^{n} = \sum_{l=1}^{\infty} A_{out}^{n,l} \frac{1}{r^{l+1}} P_l^1(\cos\theta)\cos\phi, \tag{51a}$$

$$T_{in}^{n} = \sum_{l=1}^{\infty} A_{in}^{n,l} r^{l} P_l^1(\cos\theta)\cos\phi, \tag{51b}$$

where $A_{in}^{n,l}$ and $A_{out}^{n,l}$ are the unknown coefficients for the temperature field interior and exterior to the drop, and the $P_l^1(\cdot)$'s are the normalized associated Legendre functions.

The method of reflections procedure begins by specifying the 0^{th} term in (49) as the imposed temperature field exterior to the droplet.

$$T_2^0 = T^{\infty}, \tag{52a}$$

$$T_3^0 = 0. \tag{52b}$$

By construction, this choice for T_2^0 conveniently satisfies the asymptotic boundary conditions (35a). A general solution for T_{in}^{1d} and T_{out}^{1d} is given by (51). This solution is then added to (52) and substituted into the boundary conditions at the droplet surface. The orthogonality of the spherical harmonics are used to derive a linear system of equations for the unknown coefficients. Only one mode in the general solution is found to be non-zero. The coefficients of this mode are given by:

$$A_{out}^{1} = -\frac{\beta_3 - 1}{\beta_3 + 2}, \tag{53a}$$

$$A_{in}^{1} = \frac{3}{\beta_3 + 2}. \tag{53b}$$

The first reflection from the interface $\partial\Omega_d$, T_{in}^{1d} and T_{out}^{1d}, is given by direct substitution of (53) into the general solution (51).

To enforce the boundary conditions everywhere at $\partial\Omega_d$, the exterior solution is superimposed with the reflected field using the transformation $z = 2\delta - z$

$$T_{out}^{1p} = T_{out}^{1d}\big|_{z=2\delta-z}\,. \tag{54}$$

This is precisely the temperature field of an identical droplet placed at a distance 2δ above the submerged drop. The transformation simply reduces to a coordinate transformation that helps satisfy the zero heat flux boundary condition at the air-substrate interface for an arbitrary T_{out}^{1d}.

To determine T_{in}^{2d} and T_{out}^{2d}, T_{out}^{1p} is first expanded in powers of ϵ up to $\mathcal{O}\left(\epsilon^9\right)$. This truncation order was chosen so that a direct comparison with Chen's results [6] can be made later in the chapter.

$$T_{out,\epsilon}^{1p} = \left(-\frac{\beta_3 - 1}{\beta_3 + 2}\right) \sum_{l=3}^{8} \left(r^{l-2} P_{l-2}^{1}(\cos\theta)\cos\phi\right) \epsilon^l, \tag{55}$$

where the subscript ϵ is used to denote that the field has been asymptotically expanded and truncated. The reflection from the droplet is found by substituting $T_{out,\epsilon}^{1p}$ and T_{out}^{2d} (for the exterior field) and T_{in}^{2d} (for the interior field) into the boundary conditions at the droplet surface. The orthogonality of the spherical harmonics is used to derive a linear system of equations for the unknown coefficients. This time however, six modes of the general solution are found to be non-zero. The coefficients of these modes are given by

$$A_{out}^{l} = \left(\frac{(\beta_3 - 1)l}{(\beta_3 + 2)(l(\beta_3 + 1) + 1)}\right) \epsilon^{(l+2)}, \quad l = 1..6 \tag{56a}$$

and

$$A_{in}^{l} = -\left(\frac{(\beta_3 - 1)(2l + 1)}{(\beta_3 + 2)(l(\beta_3 + 1) + 1)}\right) \epsilon^{(l+2)}, \quad l = 1..6 \tag{56b}$$

T_{in}^{2d} and T_{out}^{2d} are given by direct substitution of (56) into the general solution (51).

To satisfy the boundary conditions at the air-substrate interface T_{out}^{2d} is again reflected and the result

$$T_{out}^{2p} = T_{out}^{2d}\big|_{z=2\delta-z}\,, \tag{57}$$

is locally expanded in powers of ϵ and once again truncated at $\mathcal{O}\left(\epsilon^9\right)$

$$\begin{aligned} T_{2,\epsilon}^{2p} = \sum_{l=1}^{3} \Bigg[& \left(r^l \left(\frac{\beta_3 - 1}{\beta_3 + 2} \right)^2 P_l^1(\cos\theta)\cos\phi \right) \epsilon^{l+5} + \\ & + \left(r^l \left(\frac{6(\beta_3 - 1)^2}{(\beta_3 + 2)(2\beta_3 + 3)} \right) P_1^1(\cos\theta)\cos\phi \right) \epsilon^8 \Bigg]. \end{aligned} \tag{58}$$

Due to the presence of ϵ in all of the coefficients of T_{out}^{2d}, this local expansion contains fewer terms then $T_{1,\epsilon}^{1p}$. The solution for T_{in}^{3d} and T_{out}^{3d} will only requires three modes of the general solution. The coefficient of these corrections are given by

$$A_{out}^1 = -\left(\frac{\beta_3 - 1}{\beta_3 + 2} \right)^3 \epsilon^6 - \left(\frac{6(\beta_3 - 1)^3}{(\beta_3 + 2)^2(2\beta_3 + 3)} \right) \epsilon^8, \tag{59a}$$

$$A_{out}^l = -\left(\frac{l(\beta_3 - 1)^3}{(\beta_3 + 2)^2(l(\beta_3 + 1) + 1)} \right) \epsilon^{(l+5)}, \quad l = 2, 3 \tag{59b}$$

$$A_{in}^1 = \left(3\frac{(\beta_3 - 1)^2}{(\beta_3 + 2)^3} \right) \epsilon^6 + \left(\frac{18(\beta_3 - 1)^2}{(\beta_3 + 2)^2(2\beta_3 + 3)} \right) \epsilon^8, \tag{59c}$$

$$A_{in}^l = \left(\frac{(2l + 1)(\beta_3 - 1)^2}{(\beta_3 + 2)^2(l(\beta_3 + 1) + 1)} \right) \epsilon^{(l+5)}, \quad l = 2, 3 \tag{59d}$$

A final reflection of T_{out}^{3d} about interface $\partial\Omega_p$ is repeated and T_{out}^{3p} is expanded in powers of ϵ. This time, however, the lowest order term in the expansion is $\mathcal{O}\left(\epsilon^9\right)$, so that

$$T_{2\epsilon}^{3p} = 0. \tag{60}$$

Because the expansion of the third and final reflection from $\partial\Omega_p$ is zero it will not affect the boundary conditions at the droplet surface. Since these boundary conditions have already been satisfied to $\mathcal{O}\left(\epsilon^9\right)$, no further reflections are necessary. When computing local expansions of the reflected field, the truncation order was chosen to facilitate comparison with the results of ([6]) in Section 3.7.1. However, nothing prevents choosing a higher truncation order besides a distaste for algebra.

A different truncation order only changes the total number of reflections required to satisfy all boundary conditions to that given order. This is perhaps the most attractive feature of the method of reflections.

The final form of the interior temperature field is a linear superposition (49) of all reflections. As an alternative, the interior field may be represented in the form of the general solution (51b) with each of the coefficients A_{in}^{l} expressed as a power series in ϵ. For convenience, the result for the interior temperature field is summarized in Table 2. Unlike the interior portion of the temperature field, the final form of the exterior field is a superposition of its general solution (51a) with its reflection about $\partial\Omega_p$ (i. e., the general solution evaluated at $z = 2\delta - z$). Like the interior field, the coefficients A_{out}^{l} can be conveniently expressed as a power series in ϵ. These coefficients are summarized in Table 3.

The accuracy of this solution is found by computing the error in the boundary conditions. This error is defined as the sum of the squares of each boundary condition evaluated with a solution found by the method of reflections.

$$E_i = \frac{1}{E_0} \sum_j |B.C._j|^2. \tag{61}$$

where $B.C._j$ is the j^{th} boundary condition evaluated at the i^{th} interface. The term E_0 in (61) is a normalization constant, and is defined as

$$E_0 = \sum_{i,j} \int_{\partial\Omega_i} |\bar{B.C}._j|^2 dS_i. \tag{62}$$

The bar over $\bar{B.C}._j$ is used to designate that the boundary conditions have been evaluated with a particular solution. When calculating solutions by the method of reflections, this will be the temperature or velocity field found if no reflections about the air-substrate interface are taken into account. In other words, E_0 uses the solution for a droplet in an unbounded substrate.

The method of reflections procedure is terminated with a final reflection about the air-substrate interface. As a result, the error at that interface is exactly zero and

Table 2: The coefficients for the interior temperature field (51b). To find the value of the coefficient to a given order, each element in the table is first multiplied by the power of ϵ corresponding to that elements column. The resultant products are then added up across that coefficients row to the desired order. The total interior temperature field is given by substituting the resultant coefficients into the general solution.

	$\epsilon^{\mathbf{0}}$	$\epsilon^{\mathbf{1}}$	$\epsilon^{\mathbf{2}}$	$\epsilon^{\mathbf{3}}$	$\epsilon^{\mathbf{4}}$
$\mathbf{A^1_{in}}$	$\frac{3}{\beta_3+3}$	0	0	$-\frac{3(\beta_3-1)}{(\beta_3+2)^2}$	0
$\mathbf{A^2_{in}}$	0	0	0	0	$-\frac{5(\beta_3-1)}{(\beta_3+2)(2\beta_3+3)}$
$\mathbf{A^3_{in}}$	0	0	0	0	0
$\mathbf{A^4_{in}}$	0	0	0	0	0
$\mathbf{A^5_{in}}$	0	0	0	0	0
$\mathbf{A^6_{in}}$	0	0	0	0	0

	$\epsilon^{\mathbf{5}}$	$\epsilon^{\mathbf{6}}$	$\epsilon^{\mathbf{7}}$	$\epsilon^{\mathbf{8}}$
$\mathbf{A^1_{in}}$	0	$\frac{3(\beta_3-1)^2}{(\beta_3+2)^3}$	0	$\frac{18(\beta_3-1)^2}{(\beta_3+2)^2(2\beta_3+3)}$
$\mathbf{A^2_{in}}$	0	0	$\frac{5(\beta_3-1)^2}{(\beta_3+2)^2(2\beta_3+3)}$	0
$\mathbf{A^3_{in}}$	$-\frac{7(\beta_3-1)}{(\beta_3+2)(3\beta_3+4)}$	0	0	$\frac{7(\beta_3-1)^2}{(\beta_3+2)^2(3\beta_3+4)}$
$\mathbf{A^4_{in}}$	0	$-\frac{9(\beta_3-1)}{(\beta_3+2)(4\beta_3+5)}$	0	0
$\mathbf{A^5_{in}}$	0	0	$-\frac{11(\beta_3-1)}{(\beta_3+2)(5\beta_3+6)}$	0
$\mathbf{A^6_{in}}$	0	0	0	$-\frac{13(\beta_3-1)}{(\beta_3+2)(6\beta_3+7)}$

Table 3: The coefficients for the exterior temperature field (51b). To find the value of the coefficient to a given order, each element in the table is first multiplied by the power of ϵ corresponding to that elements column. The resultant products are then added up across that coefficients row to the desired order. The total exterior temperature field is given by substituting the resultant coefficients into the general solution and adding its reflection about the planar interface ($z = 2\delta - z$).

	$\epsilon^{\mathbf{0}}$	$\epsilon^{\mathbf{1}}$	$\epsilon^{\mathbf{2}}$	$\epsilon^{\mathbf{3}}$	$\epsilon^{\mathbf{4}}$
$\mathbf{A^1_{out}}$	$-\frac{\beta_3-1}{\beta_3+2}$	0	0	$\frac{(\beta_3-1)^2}{(\beta_3+2)^2}$	0
$\mathbf{A^2_{out}}$	0	0	0	0	$\frac{2(\beta_3-1)^2}{(\beta_3+2)(2\beta_3+3)}$
$\mathbf{A^3_{out}}$	0	0	0	0	0
$\mathbf{A^4_{out}}$	0	0	0	0	0
$\mathbf{A^5_{out}}$	0	0	0	0	0
$\mathbf{A^6_{out}}$	0	0	0	0	0

	$\epsilon^{\mathbf{5}}$	$\epsilon^{\mathbf{6}}$	$\epsilon^{\mathbf{7}}$	$\epsilon^{\mathbf{8}}$
$\mathbf{A^1_{out}}$	0	$-\frac{(\beta_3-1)^3}{(\beta_3+2)^3}$	0	$-\frac{6(\beta_3-1)^3}{(\beta_3+2)^2(2\beta_3+3)}$
$\mathbf{A^2_{out}}$	0	0	$-\frac{2(\beta_3-1)^3}{(\beta_3+2)^2(2\beta_3+3)}$	0
$\mathbf{A^3_{out}}$	$\frac{3(\beta_3-1)^2}{(\beta_3+2)(3\beta_3+4)}$	0	0	$-\frac{3(\beta_3-1)^3}{(\beta_3+2)^2(3\beta_3+4)}$
$\mathbf{A^4_{out}}$	0	$\frac{4(\beta_3-1)^2}{(\beta_3+2)(4\beta_3+5)}$	0	0
$\mathbf{A^5_{out}}$	0	0	$\frac{5(\beta_3-1)^2}{(\beta_3+2)(5\beta_3+6)}$	0
$\mathbf{A^6_{out}}$	0	0	0	$\frac{6(\beta_3-1)^2}{(\beta_3+2)(6\beta_3+7)}$

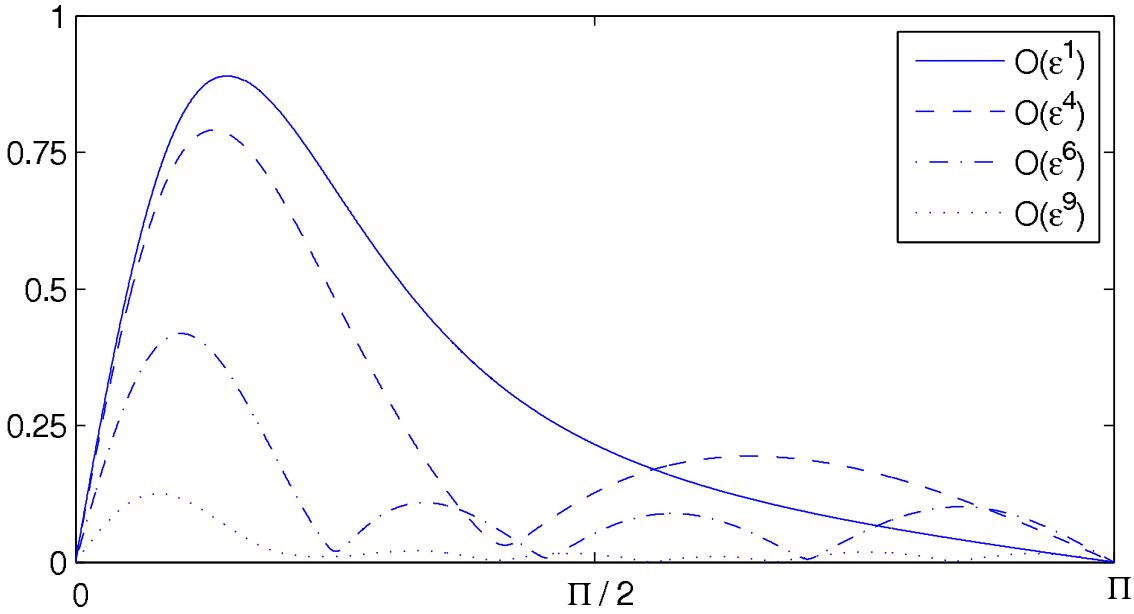

Figure 6: The error in the temperature boundary conditions at the drop-substrate interface, $\beta_3 = 0.01$ and $\delta = 1.25$, as a function of θ for solutions with increasing truncation order.

only the error at the droplet surface needs to be considered. In Fig. 6, E_d is plotted as a function of θ for different truncation orders at a specific value of submersion depth δ and thermal conductivity ratio β_3. Due to the azimuthal symmetry of the system, the ϕ dependence has been factored out. As illustrated in Fig. 6, increasing the truncation order localizes and decreases the error.

As a measure of the total error in a given solution, the residual is defined as the sum of the i^{th} errors (61), integrated over their corresponding surfaces.

$$R_T = \left[\sum_i \int_{\partial\Omega_i} E_i dS_i \right]^{1/2} . \tag{63}$$

The residual (63) as a function of δ and β_3 is plotted in Fig. 7. As illustrated by Fig. 7a, the residual decays very quickly for increasing δ. For a value of $\beta_3 = 0.01$ and $\delta = 1.25$, satisfying the boundary conditions to $\mathcal{O}(\epsilon^9)$ reduced the residual by 93% when compared to the solution of an unbounded drop. This value of δ has been used as the value that gives the maximum acceptable residual for a solution.

Variations in the temperature field occur primarily in the $\hat{\mathbf{x}}$ direction, making the

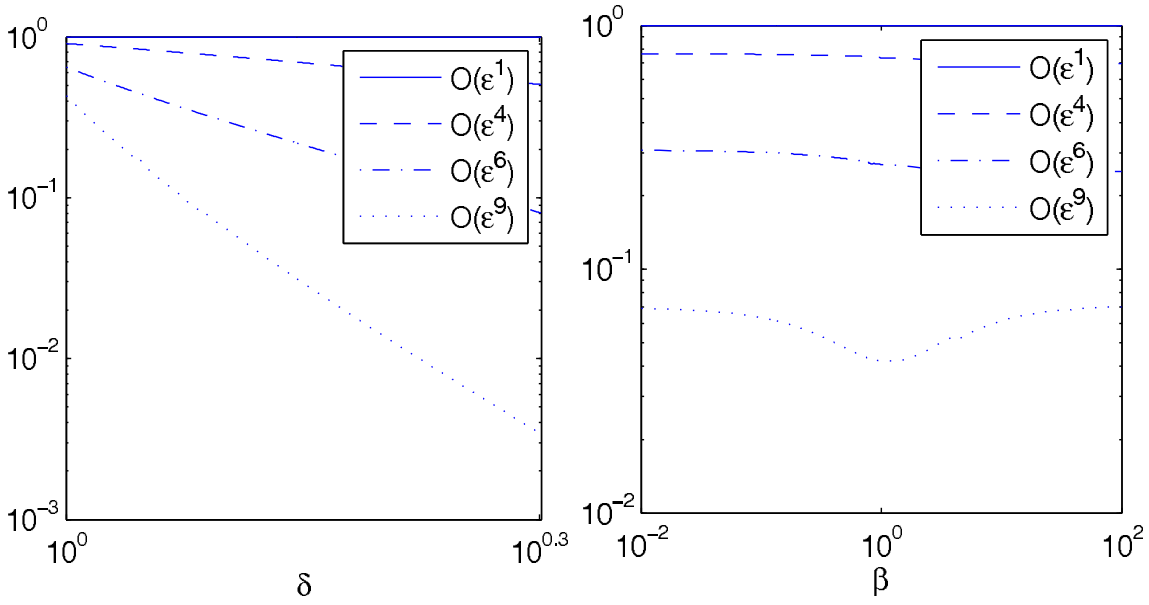

(a) (b)

Figure 7: The integrated residual at the drop-substrate interface for solutions with increasing truncation order. (a) is the Residual as a function of δ, evaluated at $\beta_3 = 0.01$. At a value of $\delta = 1.25$ the residual at $\mathcal{O}(\epsilon^9)$ is reduced by 93% when compared with the residual at $\mathcal{O}(\epsilon^1)$. (b) Residual as a function of β_3, evaluated at $\delta = 1.25$.

$y = 0$ plane a favorable slice for visualization. The level sets (i. e., isocontours) of the temperature field for a droplet in an unbounded substrate are displayed in Fig. 8 for two different values of β_3. When β_3 is very small, as seen in Fig. 8a, the temperature gradient near the drop is increased. When β_3 becomes very large the temperature gradient is considerably reduced (Fig. 8b).

When the submerged droplet approaches the air-substrate interface, an asymmetry in the relative magnitude of the temperature gradient between the drop's top and bottom surface develops, this asymmetry is just visible in Fig. 9. There, the level sets of the temperature field are shown for small and large values of the thermal conductivity ratio β_3, for a scaled submersion depth $\delta = 1.25$. If the droplet is located near the planar interface, this effect results in a very nonuniform temperature gradient near the surface of the droplet. This differs from the case of the unbounded drop of Fig. 8, which has the same temperature gradient on the top and bottom

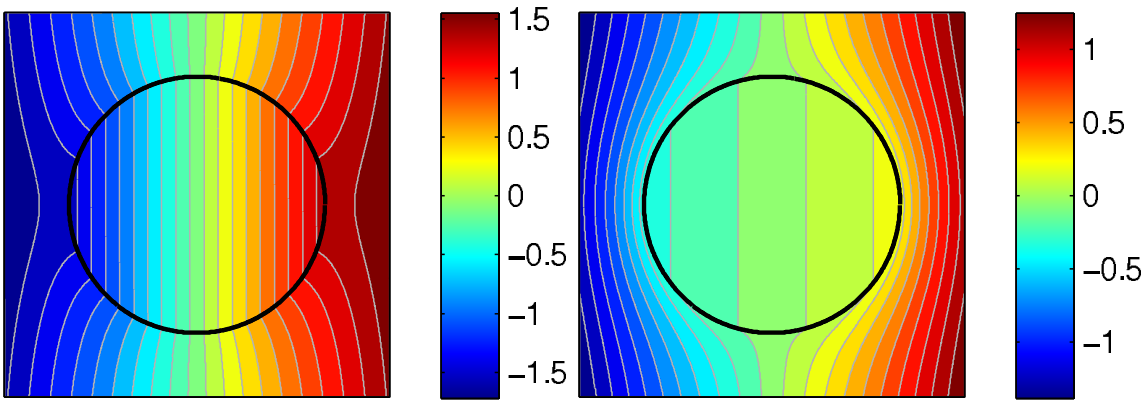

(a) (b)

Figure 8: The temperature field for a droplet in an unbounded substrate in the $y = 0$ plane. The contour levels are scaled with the maximum value corresponding to red (hot) and the minimum value corresponding to blue (cold). Panel (a) corresponds to a value of $\beta_3 = 0.01$ and panel (b) to the value $\beta_3 = 10$.

surface of the droplet.

For a droplet submerged near the planar interface ($\delta = 1.25$), it was found that β_3 determines the strength of the temperature gradient, just as with the unbounded drop. However, unlike the unbounded drop, β_3 also determines the location of the maximum temperature gradient. To illustrate this last point, the component of the temperature gradient tangent to the interface is plotted as a function of position in Fig. 10. As seen in Fig. 10d, increasing β_3 shifted the location of the maximum gradient from the top of the drop to the bottom. The same effect is seen at the interface $\partial\Omega_p$ in Fig. 10b, where increasing β_3 shifted the maximum from directly over the droplet to off-center.

Because the thermocapillary stress at an interface is proportional to the local temperature gradient, these results provide valuable information when attempting to understand the velocity field in and around the drop. For example, we can determine from Fig. 10a that the non-uniformity in the temperature gradient at the air-substrate interface is almost entirely contained within three drop radii of the origin.

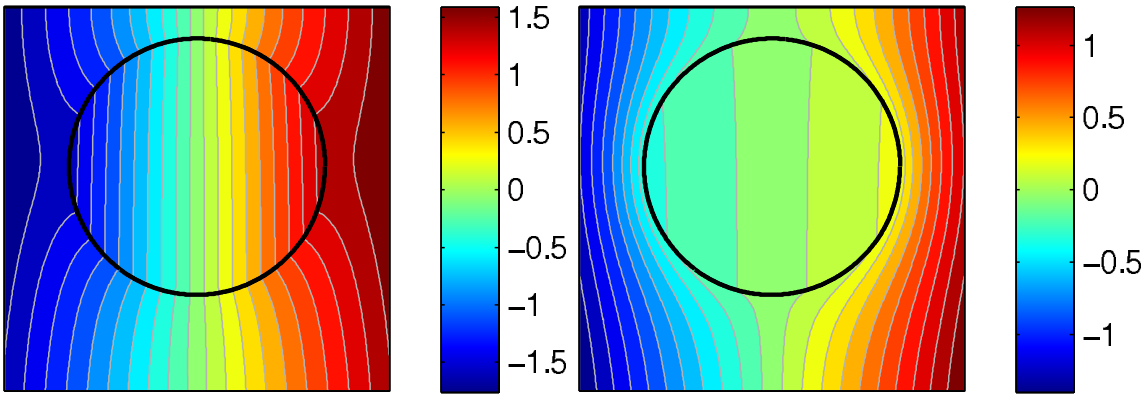

(a) (b)

Figure 9: Temperature field for a submerged droplet in the $y = 0$ plane for $\delta = 1.25$. The interface $\partial\Omega_p$ is located at the top of each panel. Panel (a) corresponds to a value of $\beta_3 = 0.01$ and panel (b) to the value $\beta_3 = 10$.

3.7 A Solution for The Velocity Field

The general solution to the Stokes equation in spherical coordinates is known as Lamb's solution [20] and is based on the spherical harmonic expansion for the pressure field. Employing the requirements on boundedness and symmetry analogous to the temperature field allows us to simplify Lamb's solution to

$$V^n_{out,r} = \sum_{l=1}^{\infty} \left(B^{n,l}_{out} \frac{l+1}{2(2l-1)} - C^{n,l}_{out} \frac{l+1}{r^2} \right) r^{-l} P^1_l \cos\phi, \tag{64a}$$

$$V^n_{out,\theta} = \sum_{l=1}^{\infty} \left(B^{n,l}_{out} \frac{2-l}{2l(2l-1)} \frac{dP^1_l}{d\theta} + C^{n,l}_{out} \frac{1}{r^2} \frac{dP^1_l}{d\theta} + D^{n,l}_{out} \frac{P^1_l}{r\sin\theta} \right) r^{-l} \cos\phi, \tag{64b}$$

$$V^n_{out,\phi} = \sum_{l=1}^{\infty} \left(B^{n,l}_{out} \frac{(l-2)P^1_l}{2l(2l-1)\sin\theta} - C^{n,l}_{out} \frac{P^1_l}{r^2\sin\theta} - D^{n,l}_{out} \frac{1}{r} \frac{dP^1_l}{d\theta} \right) r^{-l} \sin\phi, \tag{64c}$$

$$p_{out} = \sum_{l=1}^{\infty} B^{n,l}_{out} P^1_l r^{-l-1} \cos\phi, \tag{64d}$$

for the nondimensional velocity and pressure fields in the substrate. Similarly the general solution for the interior field is given by

$$V^n_{in,r} = \sum_{l=1}^{\infty} \left(B^{n,l}_{in} \frac{lr}{2\alpha_3(2l+3)} + C^{n,l}_{in} \frac{l}{r} \right) r^l P^1_l \cos(\phi), \tag{65a}$$

$$V^n_{in,\theta} = \sum_{l=1}^{\infty} \left(B^{n,l}_{in} \frac{l+3}{2\alpha_3(l+1)(2l+3)} \frac{dP^1_l}{d\theta} + C^{n,l}_{in} \frac{1}{r} \frac{dP^1_l}{d\theta} + D^{n,l}_{in} \frac{P^1_l}{\sin\theta} \right) r^l \cos(\phi), \tag{65b}$$

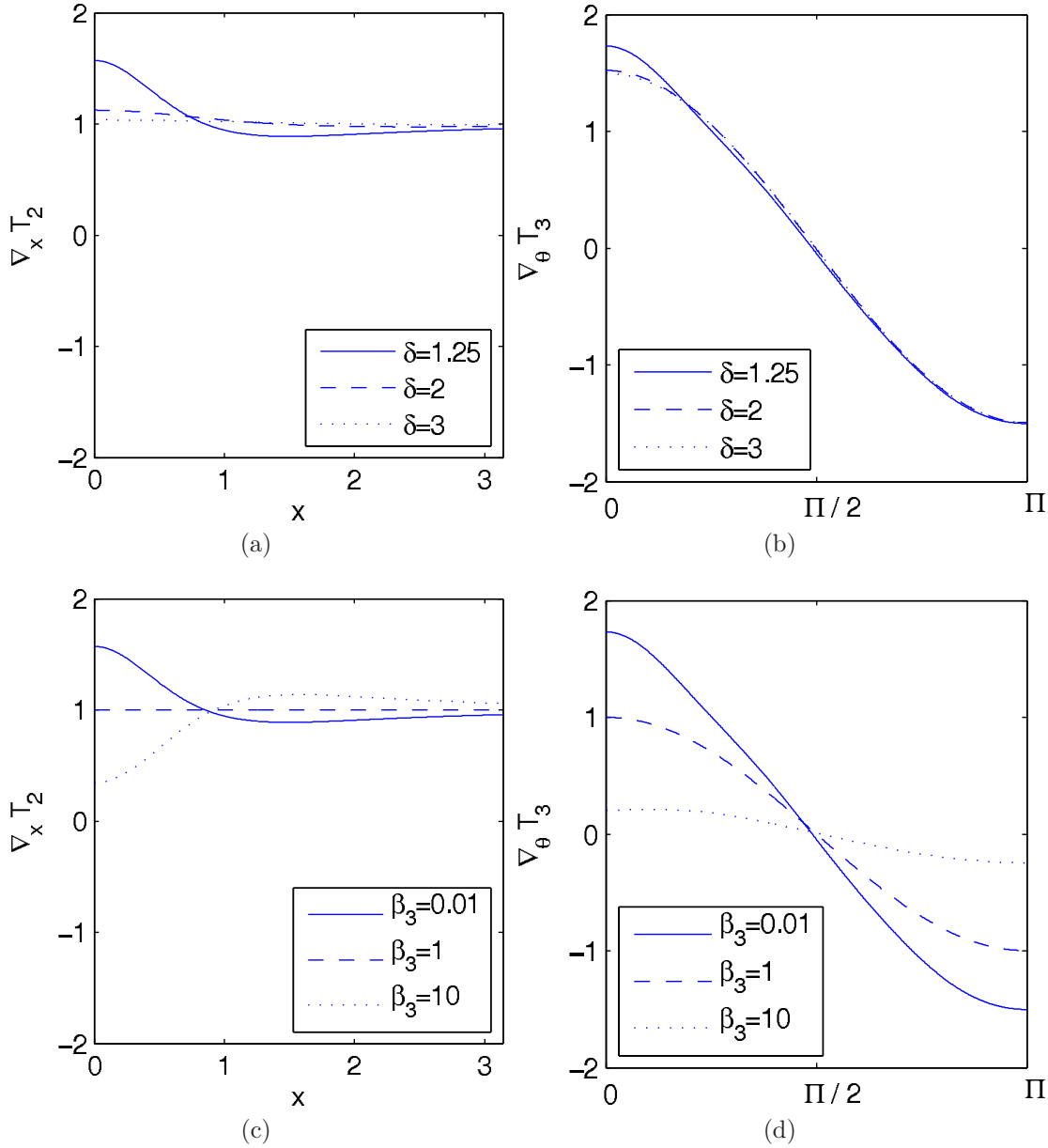

Figure 10: Temperature gradient components along the planar (a), (c) and droplet (b), (d) interfaces for various values of δ and β_3. (a) $\beta_3 = 0.01$, (b) $\beta_3 = 0.01$, (c) $\delta = 1.25$ and (d) $\delta = 1.25$.

$$V^n_{in,\phi} = \sum_{l=1}^{\infty} \left(B^{n,l}_{in} \frac{-(l+3) r P^1_l}{2\alpha_3 l(2l+3)(l+1)\sin\theta} - C^{n,l}_{in} \frac{P^1_l}{r\sin\theta} - D^l_{in} \frac{dP^1_l}{d\theta} \right) r^l \sin(\phi), \quad (65c)$$

$$p_{in} = p_0 + \sum_{l=1}^{\infty} B^{n,l}_{in} P^1_l r^l \cos(\phi). \quad (65d)$$

where $B^{n,l}_i$, $C^{n,l}_i$, and $D^{n,l}_i$ are the unknown coefficients. For brevity, the $\cos\theta$ dependence of the associated Legendre functions was omitted. The hydrostatic pressure p_0 is determined from the Young-Laplace equation as

$$p_0 = \frac{2}{\gamma_{12} Ca_2}. \quad (66)$$

Like the temperature field solution, the same process of successive reflections is used here to find the contributions to the velocity field (49) for the submerged droplet system. A minor difference between the procedures for the temperature and velocity fields is that one is a scalar field, while the other is a vector field, and this difference is only manifest in the transformation used when reflecting about the planar interface. For the velocity field, this transformation (reflection) is given by

$$V^{np}_{out,x} = V^{nd}_{out,x}\big|_{z=2\delta-z}, \quad (67a)$$

$$V^{np}_{out,y} = V^{nd}_{out,y}\big|_{z=2\delta-z}, \quad (67b)$$

$$V^{np}_{out,z} = -V^{nd}_{out,z}\big|_{z=2\delta-z}, \quad (67c)$$

$$p^{np}_{out} = p^{nd}_{out}\big|_{z=2\delta-z}. \quad (67d)$$

The difference in sign for the $\hat{\mathbf{z}}$ component of the exterior velocity ensures that the field remains divergence-free and satisfies the stress-free boundary condition at $\partial\Omega_p$. Moreover, the pressure field must similarly be reflected to satisfy the governing equations (28), and is used when calculating the surface force on the droplet (45).

3.7.1 Velocity Contributions from Surface Tension Gradients At The Substrate-Drop Interface

When the ratio of the temperature coefficients of surface tension is zero, $\tau_{12} = 0$, the thermocapillary stress at the interface $\partial\Omega_p$ is also zero. In this limit, only the

thermocapillary stress from the droplet surface will drive the velocity field. The role of the air-substrate interface is reduced to constraining the normal component of the exterior velocity to zero everywhere along $\partial\Omega_p$. This constraint impacts the migration velocity and flow field when the droplet is near the planar interface. The inclusion of thermocapillary stress at the planar interface $\partial\Omega_p$, (i. e. $\tau_{12} \neq 0$) is considered in Section 3.7.2.

In addition to differences in the reflection transformation for the velocity field, there is a fair amount of bookkeeping required when converting between the Cartesian and spherical coordinate systems. These cumbersome conversions are omitted here and only the final result for the velocity and pressure fields are listed.

The process of reflection begins again by specifying the 0^{th} order contribution. In the limit $\tau_{12} = 0$, the velocity field decays to zero far from the drop and

$$\mathbf{V_2^0} = 0. \tag{68}$$

The first reflection about the droplet surface is found by substituting the solution for the temperature field (summarized in Tables 2 & 3), along with the general solution for the velocity field, into the boundary conditions given in Eqs. (30),(31a). The solution must also satisfy the zero force constraint (45). By direct substitution of the general solution (64), the zero force constraint reduces to the condition

$$B_{out}^1 = 0. \tag{69}$$

The orthogonality of the spherical harmonics is again used to reduce the remaining boundary conditions to a system of linear equations for the unknown coefficients, yielding the corrections. The solution for the exterior field $\mathbf{V_{out}^{1d}}$ is then reflected about the interface $\partial\Omega_p$ and locally expanded in powers of ϵ. In keeping with the order of approximation made in the temperature field, the velocity and pressure field are truncated at $\mathcal{O}(\epsilon^9)$.

Since the thermocapillary stress contribution to the jump in surface stress at $\partial\Omega_d$ has already been accounted for in the first reflection, this boundary condition is reduced to requiring continuity in the tangential surface stress at the droplet surface. In addition, by direct substitution of $\mathbf{V}^{\mathbf{1p}}_{\mathbf{out},\epsilon} + \mathbf{V}^{\mathbf{2d}}_{\mathbf{out}}$ and $p^{1p}_{out,\epsilon}$ into (45) the zero force constraint again reduces to (69). The remaining boundary conditions are again reduced to a linear system by exploiting the orthogonality of the spherical harmonics. Corrections from the second reflection about the droplet surface that satisfy the boundary conditions at the droplet surface are found.

This process is repeated again and the reflected fields are expanded, truncated and substituted into the boundary conditions. The force constraint again reduces to (69) and the remaining boundary conditions are solved.

The third reflection about $\partial\Omega_p$ is locally expanded. Similar to the derivation process of the temperature field, this process is completed when the lowest order term are found to be of $\mathcal{O}(\epsilon^9)$. The interior velocity field is represented in the form of the general solution, with each of the coefficients expressed as a power series in ϵ. The final form of the exterior velocity field is a superposition of its general solution with its reflection. The coefficients are listed in Appendix A.

Like the solution for the temperature field, the accuracy of this solution can be judged by an examination of the error (61) and residual (63). The error on the surface of the droplet is shown in Fig. 11a. Unlike the temperature field, the maximum error in the boundary conditions is located at the top of the droplet. The variation in the residual for different values of δ, α_3 and β_3 is illustrated in Fig. 11. As seen in Fig. 11b, the residual in the boundary conditions is found to decrease with increasing distance from the air-substrate interface.

The velocity field found from the first reflection about the droplet and in the reference frame of the droplet simplify to

$$V_{3,r} = -3\,\frac{\sin(\theta)\cos(\phi)\,(r^2-1)}{(3\,\alpha_3+2)\,(\beta_3+2)}, \tag{70a}$$

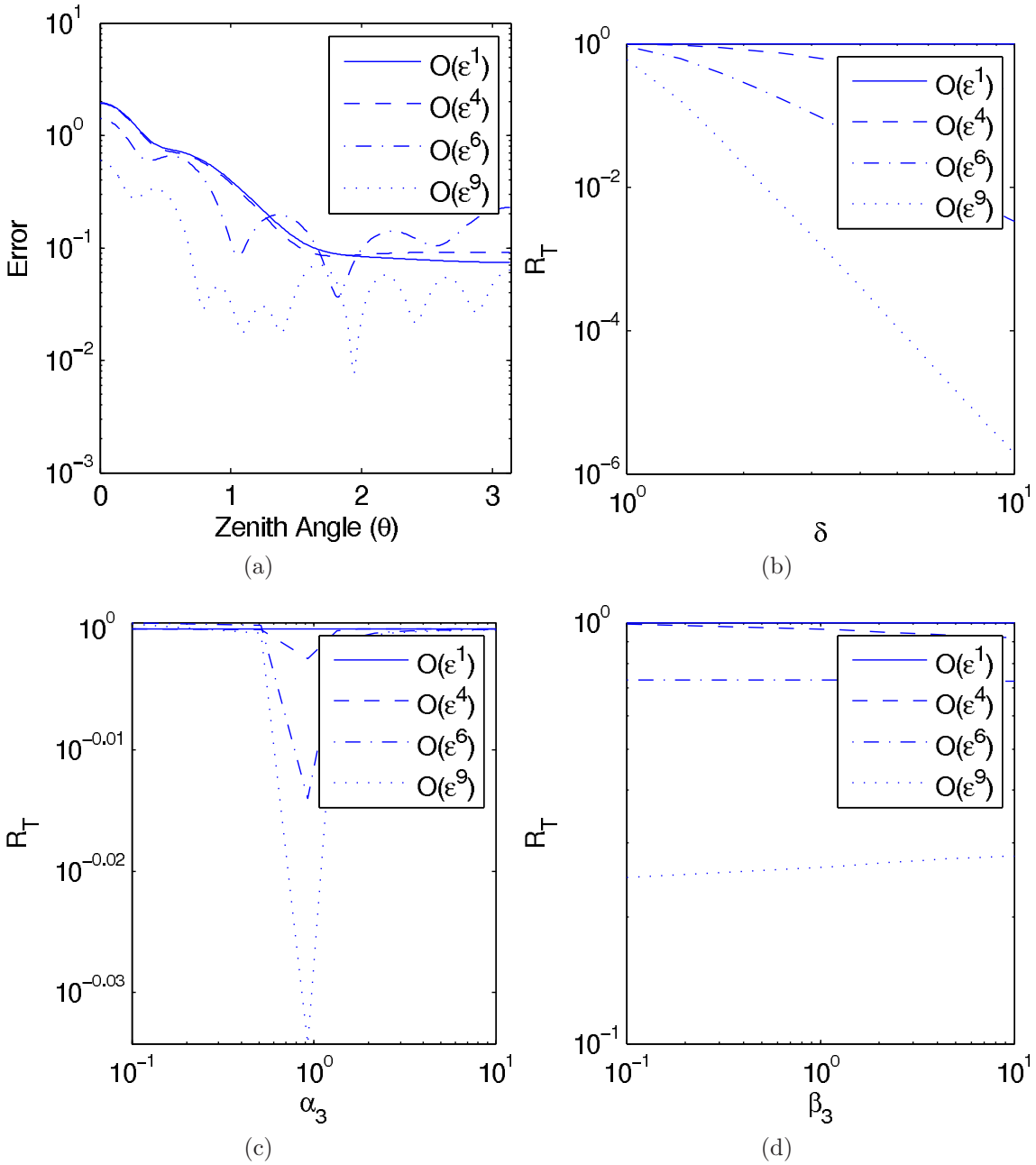

Figure 11: Variations in the error and residual at the drop-substrate interface for solutions containing an increasing number of reflections. Panel (a) is the error at the surface of the droplet as a function of the zenith angle, evaluated at $\alpha_3 = \beta_3 = 1$ and $\delta = 1.25$. Panel (b) is the residual as a function of δ, evaluated at $\alpha_3 = \beta_3 = 1$. Panel (c) is the residual as a function of α_3, evaluated at $\delta = 1.25$ and $\beta_3 = 1$. Panel (d) is the residual as a function of β_3, evaluated at $\delta = 1.25$ and $\alpha_3 = 1$.

$$V_{3,\theta} = -3\,\frac{(-1+2\,r^2)\cos(\theta)\cos(\phi)}{(3\,\alpha_3+2)\,(\beta_3+2)}, \tag{70b}$$

$$V_{3,\phi} = 3\,\frac{(-1+2\,r^2)\sin(\phi)}{(3\,\alpha_3+2)\,(\beta_3+2)}, \tag{70c}$$

and

$$V_{2,r} = -2\,\frac{(r^3-1)\sin(\theta)\cos(\phi)}{(\beta_3+2)\,(3\,\alpha_3+2)\,r^3}, \tag{70d}$$

$$V_{2,\theta} = -\frac{(2\,r^3+1)\cos(\theta)\cos(\phi)}{(\beta_3+2)\,(3\,\alpha_3+2)\,r^3}, \tag{70e}$$

$$V_{2,\phi} = \frac{(2\,r^3+1)\sin(\phi)}{r^3\,(3\,\alpha_3+2)\,(\beta_3+2)}. \tag{70f}$$

This result exactly matches the Young *et al.* [50] solution for a spherical droplet in an unbounded substrate that moves in a constant temperature gradient and has negligible Re and Pe [42]. The complete flow field for the submerged drop is three-dimensional. However because of the natural symmetry of the system, the $\hat{\mathbf{y}}$ component of the velocity field will vanish when $y = 0$, making the velocity two-dimensional in this limit. On the other hand, the $\hat{\mathbf{y}}$ and $\hat{\mathbf{z}}$ components of the velocity field are zero when $x = 0$. These two planes provide a convenient slice plane for visualizing the velocity field. The interior flow was found to be the familiar Hill's spherical vortex, as observed from the stream lines of Fig. 12.

Two limiting cases for the velocity field are of particular interest because they correspond to cases previously studied by Meyyappan *et al.* [27] and Chen [6]. The first case is when the thermal conductivity and viscosity of the droplet are very small (i. e. $\alpha_3 = \beta_3 = 0$), such as in the case of a gas bubble. The second case is when the thermal conductivity of the drop is equal to that of the substrate (i. e. $\beta_3 = 1$). In this case the interaction between the droplet and the planar interface have no effect on the temperature field, which remains equal to the imposed field and is linear in x.

For both cases, the flow fields look similar to the recirculating dipole flow of a drop in an inbounded substrate as seen in Fig. 12. The differences that do exist are only discernible by comparing level sets of the velocity fields. Fig. 13 shows a series

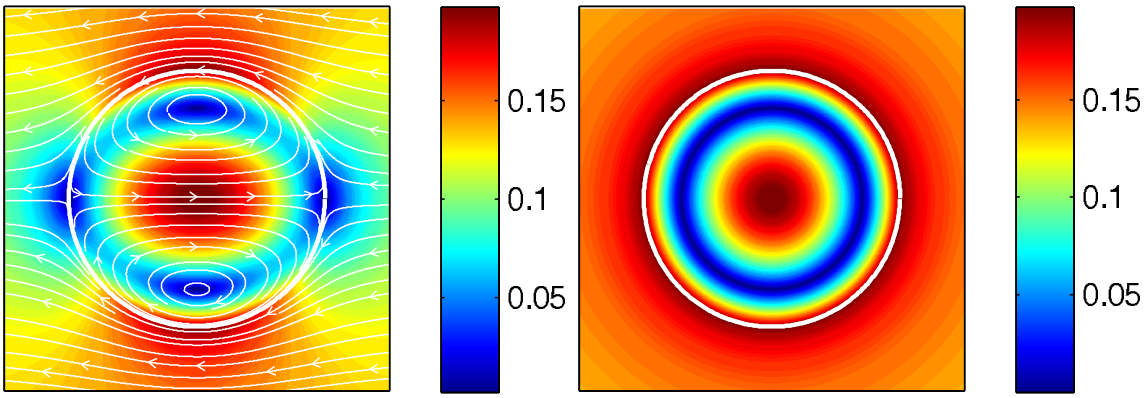

(a) (b)

Figure 12: The velocity field for an unbounded droplet ($\delta \to \infty$) with $\alpha_3 = \beta_3 = 1$. This counter-rotating flow is known as Hill's spherical vortex. (a) Streamlines and magnitude of the velocity field in the $y = 0$ plane. (b) Magnitude of the velocity field in the $x = 0$ plane.

of stream plots for various values of the scaled submersion depth δ. The interior streamlines resemble that of the unbounded drop; only variation in the contours is discernable.

The scaled migration velocity of the droplet provides a better rubric for comparing the solution at different parameter values than the comparison of streamlines for different velocity fields. It is even more illuminating to examine the ratio of migration velocities between the submerged droplet and a similar droplet in an unbounded substrate, known as the mobility function.

$$M \equiv \frac{u}{u^{1d}}. \tag{71}$$

When $\epsilon \to 0$, the mobility function approaches one. As ϵ increases from zero, the effect of the neighboring planar interface on the droplet coincides with a deviation in the mobility function from unity. Hence the mobility function provides a direct measure of the effect of the planar interface on the migration velocity of the droplet.

The first correction to the scaled migration velocity determined for the submerged droplet is

$$u^{1d} = \frac{2}{(\beta_3 + 2)\,(3\,\alpha_3 + 2)}. \tag{72}$$

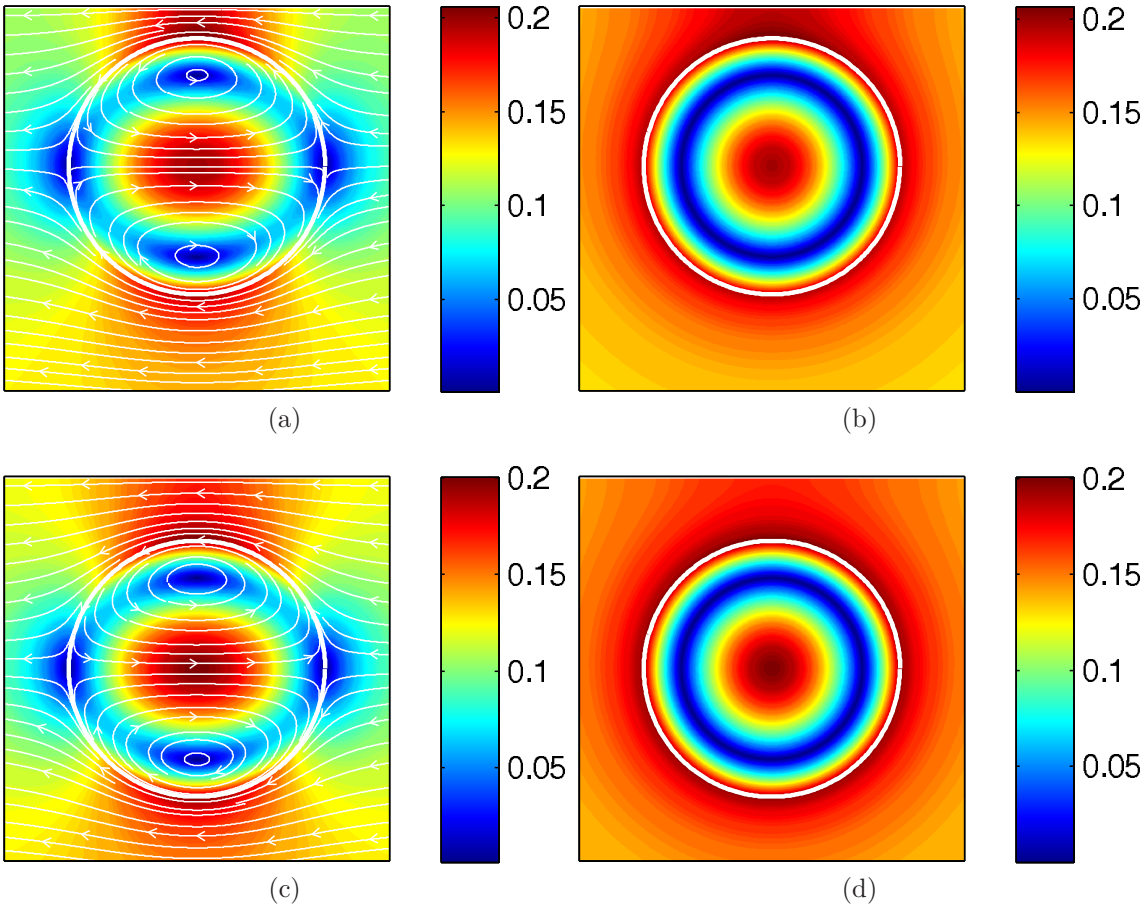

Figure 13: Velocity field for a submerged droplet with at different submersion depths and $\alpha_3 = \beta_3 = 1$. (a), (b) Correspond to $\delta = 1.25$. (c), (d) Correspond to $\delta = 1.5$.

This is in exact agreement with that first derived by Young *et al.* [50] for the drop in an unbounded substrate. Upon substituting this correction into (71), the mobility function for the submerged droplet is derived

$$\begin{aligned} M = 1 &- \left(\frac{3}{2(\beta_3+2)}\right)\beta_3\epsilon^3 + \left(\frac{3(\beta_3-1)}{2(\beta_3+2)^2}\right)\beta_3\epsilon^6 + \\ &+ \left(\frac{474\,\beta_3 + 288 + 1641\,{\beta_3}^2 + 1062\,{\beta_3}^3}{8(\alpha_3+1)(3\beta_3+4)(3\alpha_3+2)(\beta_3+2)(2\beta_3+3)}\right){\alpha_3}^2\epsilon^8 + \\ &+ \left(\frac{-192 + 1008\,{\beta_3}^3 - 36\,{\beta_3}^2 - 2040\,\beta_3}{8(\alpha_3+1)(3\beta_3+4)(3\alpha_3+2)(\beta_3+2)(2\beta_3+3)}\right)\alpha_3\epsilon^8 + \\ &+ \left(\frac{12\,\beta_3\,\left(-37\,\beta_3 + 22\,{\beta_3}^2 - 90\right)}{8(\alpha_3+1)(3\beta_3+4)(3\alpha_3+2)(\beta_3+2)(2\beta_3+3)}\right)\epsilon^8 + \mathcal{O}\left(\epsilon^9\right). \end{aligned} \tag{73}$$

The first correction to the scaled migration velocity is in the ϵ^3 term, because the exterior velocity field and temperature gradient decay as r^{-3}. This effect is much smaller then the $\mathcal{O}(\epsilon^1)$ interaction found between a plane boundary and a droplet when the motion is driven by a body force [13, 42]. In addition, examination of (73) reveals that the first contribution from thermal conductivity ratio β_3 is in the ϵ^3 term, whereas the first contribution from the viscosity ratio α_3 occurs in the ϵ^8 term.

The mobility function is plotted in Fig. 14 for different values of α_3, β_3 and δ. The effect of the air-substrate interface on the velocity field becomes negligible for $\delta > 3$, similar to what happens for the temperature field. When $\delta < 3$, the planar interface in general retards the migration of the droplet. The migration velocity is observed to monotonically decrease with increasing β_3, similar to the case of a simple droplet in an unbounded substrate Fig. 14c. A very gentle increase in the migration velocity is observed as the viscosity ratio is increased (Fig. 14d). This effect is more pronounced for large values of the thermal conductivity ratio, and is the complete opposite of what would be observed if the droplet were in an unbounded substrate.

In general, the submerged droplet migrates more slowly than an unbounded droplet. When the thermal conductivity of the drop is zero, as would be the case

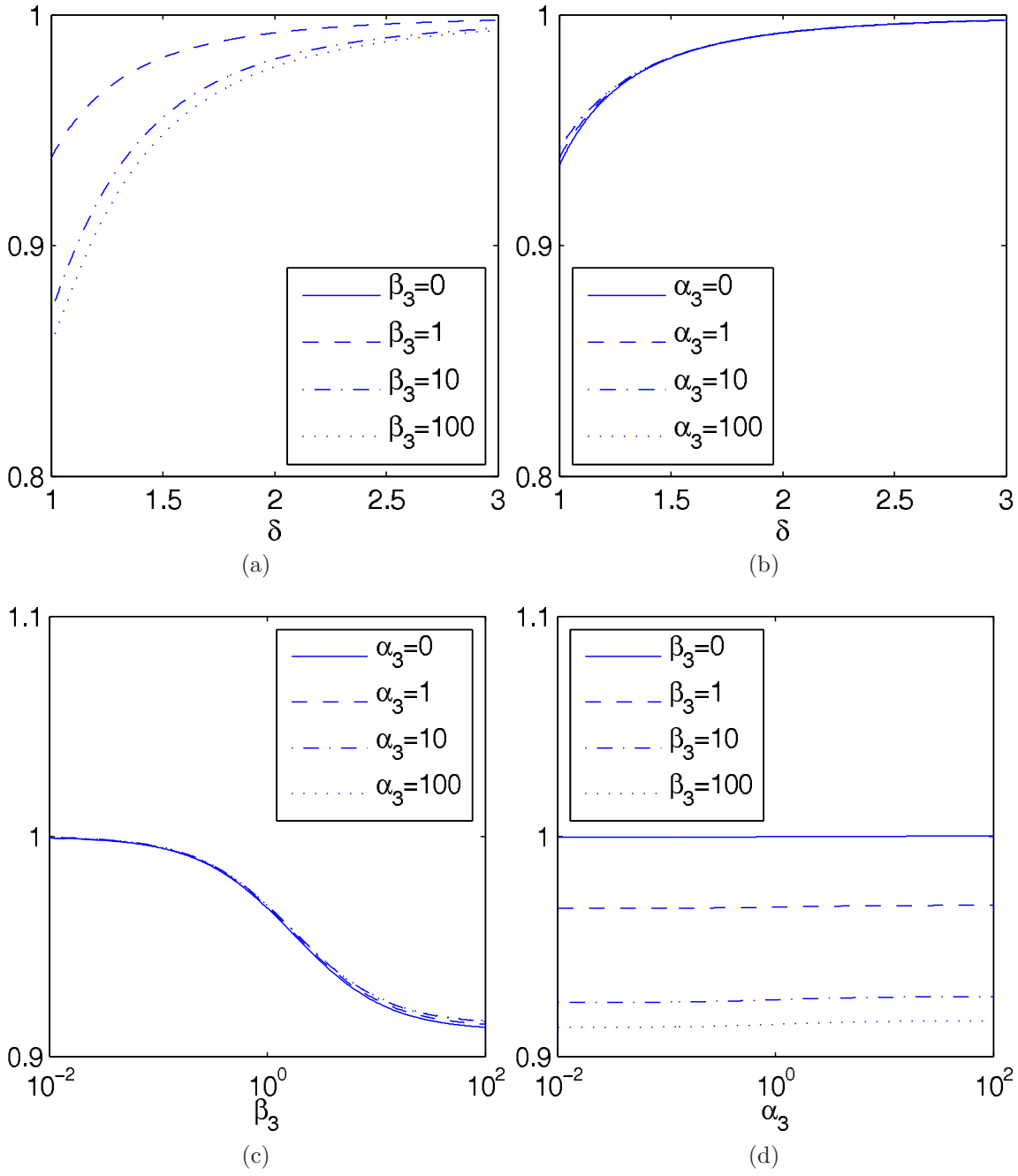

Figure 14: The mobility function. (a) $\alpha_3 = 1$, (b) $\beta_3 = 1$, (c) $\delta = 1.25$ and (d) $\delta = 1.25$

for a bubble, the mobility function reduces to

$$M = 1 + \left(\frac{-64\,\alpha + 96\,\alpha^2}{64\,(\alpha+1)\,(3\,\alpha+2)} \right) \epsilon^8 + \mathcal{O}\left(\epsilon^9\right). \tag{74}$$

In this limit, for $\alpha_3 = 2/3$, the submerged droplet migrates with the exact speed as its unbounded counterpart. For values of $\alpha_3 > 2/3$, the submerged droplet migrates faster than the unbounded droplet.

Chen's mobility function, written in the nondimensional units of this chapter, is given by.

$$\begin{aligned} M_{chen} = 1 - \left(\frac{3\beta_3}{2(2+\beta_3)} \right) \epsilon^3 - \left(\frac{3\beta_3\,(1-\beta_3)}{2(2+\beta_3)^2} \right) \epsilon^6 + \frac{3}{4} \Bigg(8\,\frac{(1-\beta_3)^2}{(2+\beta_3)\,(3+2\,\beta_3)} + \\ + 4\,\frac{1-\beta_3}{(3+2\,\beta_3)\,(1+\alpha_3)} - \frac{\alpha_3\,\,(2-\alpha_3)}{(1+\alpha_3)\,(2+3\,\alpha_3)} \Bigg) \epsilon^8 + \mathcal{O}\left(\epsilon^9\right). \end{aligned} \tag{75}$$

It agrees with the mobility function (73) up to $\mathcal{O}\left(\epsilon^8\right)$. To understand the consequence of these differences, Chen's mobility function is examined in the limit $\beta_3 = 0$

$$M_{chen} = 1 + \left(\frac{16 + 26\,\alpha + 15\,\alpha^2}{4\,(1+\alpha)\,(2+3\,\alpha)} \right) \epsilon^8 + \mathcal{O}\left(\epsilon^9\right), \tag{76}$$

which predicts that a droplet will migrate faster near the air-substrate interface, regardless of its viscosity. In particular, in the gas bubble limit ($\alpha_3 = 0$), Chen's mobility function reduces to

$$M_{chen} = 1 + 2\epsilon^8 + \mathcal{O}\left(\epsilon^9\right), \tag{77}$$

which incorrectly predicts that the droplet will migrate faster near the air-substrate interface while (73) correctly predicts no change in migration velocity. Chen's results for the droplet migration velocity were determined using a modified Faxen's law [2, 1], which only requires knowledge of the temperature and velocity field exterior to the droplet. It also relies on an approximation to the velocity field that is not consistent with the truncation order used with the mobility function. Furthermore, Chen's analysis only used two reflections about the planar interface $\partial\Omega_p$ and failed to correctly determine higher order corrections to the mobility function.

3.7.2 Velocity Contributions from Surface Tension Gradients At The Air-Substrate interface

In this section, contributions to the velocity field from surface tension gradients at the air-substrate interface $\partial\Omega_p$ are determined by the method of reflections. In the previous section, during the process of satisfying boundary conditions at the droplet surface, variations in surface tension at $\partial\Omega_p$ were ignored. In this section the variation in the surface tension at the drop surface $\partial\Omega_d$ are neglected. Due to the linear nature of Stokes flow, the solution for the velocity field in these two limits can be superimposed to obtain the full solution accounting for thermocapillary stresses at both interfaces. An analysis of the superimposed velocity field is presented in Section 3.7.3.

The gradient of the temperature field at interface $\partial\Omega_p$ is nonuniform for $\beta_3 \neq 1$. Using the solution for the temperature field from Section 3.6, it was determined that using a finite number of terms in the truncated Lamb's solution (65) did not satisfy boundary conditions at $\partial\Omega_p$. Without a base solution, the method of reflection will be of no help in determining the velocity field. Instead the base solution for the velocity field can be computed using boundary integrals (see for example Pozrikidis [32]). For the particular form of the temperature field exterior to the droplet, evaluating the boundary integrals remains a significant hurdle net yet cleared.

For a special case where the thermal conductivities are equal, $\beta_3 = 1$, the truncated Lamb's general solution does satisfy the boundary conditions at $\partial\Omega_p$. In this case, the temperature gradient at $\partial\Omega_p$ is constant and the solution for the asymptotic velocity field in the substrate is given by (34). Scaling the asymptotic velocity field, as outlined at the beginning of this chapter, yields

$$V_2^{\infty} = \left(-\frac{3\tau_{12}}{4\chi}\right) z^2 + \tau_{12}\left(\frac{3\delta}{2\chi} - 1\right) z - \tau_{12}\left(\frac{\chi}{4} - \delta + \frac{3\delta^2}{4\chi}\right). \tag{78}$$

The asymptotic velocity field can is simplified further by recalling that $\chi \gg 1$, and the nonlinearity in the shear ($\propto z^2$) can be neglected near the droplet. The

remaining terms containing negative powers of χ may not be neglected because there is no restriction placed on the size of the scaled submersion depth δ. In this limit, the asymptotic velocity field (78) reduces to a shear flow with constant shear rate.

By construction, equation (78) exactly satisfies boundary conditions at the air-substrate interface. Therefore, it is suitable to use as an imposed field (i. e., the 0^{th} reflection) for the method of reflection. The solution procedure is similar to that of Section 3.7.1, however, the boundary conditions at the surface of the drop are different since there is no longer a discontinuity in the tangential shear stress.

The first reflection about the droplet surface yields a correction to the imposed shear flow (78). In the reference frame of the droplet, the superposition of the imposed shear and corrections is given by

$$V_{in,r} = \tau_{12}\frac{3\,(3\,\delta - 2\,\chi)}{8\chi\ (\alpha_3+1)}\left(r^3 - r\right)\sin(2\theta)\cos(\phi)\,, \tag{79a}$$

$$V_{in,\theta} = \tau_{12}\frac{(3\,\delta - 2\,\chi)}{8\chi\ (\alpha_3+1)}\left(5r^3\cos(2\theta) - r\,(3\cos(2\theta) - 2(\alpha_3+1))\right)\cos(\phi), \tag{79b}$$

$$V_{in,\phi} = -\tau_{12}\frac{(3\,\delta - 2\,\chi)}{8\chi\ (\alpha_3+1)}\left(5r^3 + r(2\alpha_3 - 1)\right)\cos(\theta)\sin(\phi), \tag{79c}$$

and

$$V_{out,r} = \tau_{12}\frac{(3\,\delta - 2\,\chi)}{8\chi}\left(2r - \frac{(5\,\alpha_3+2)}{r^2\,(\alpha_3+1)} + \frac{3\alpha_3}{r^4\,(\alpha_3+1)}\right)\sin(2\theta)\cos(\phi)\,, \tag{79d}$$

$$V_{out,\theta} = \tau_{12}\frac{(3\,\delta - 2\,\chi)}{4\chi}\left(r\,(1+\cos(2\theta)) - \frac{\alpha_3\ \cos(2\theta)}{r^4\,(\alpha_3+1)}\right)\cos(\phi)\,, \tag{79e}$$

$$V_{out,\phi} = -\tau_{12}\frac{(3\,\delta - 2\,\chi)}{4\chi}\left(2r - \frac{\alpha_3}{r^4\,(\alpha_3+1)}\right)\cos(\theta)\sin(\phi)\,, \tag{79f}$$

Exterior to the droplet, the magnitude of the first reflection decays radially as r^{-2}. For a scaled substrate depth of $\chi = 10$, this corresponds to a decrease in the field by 99% at the bottom of the substrate, compared to the value of the field at the surface of the drop. Therefore, the minimum value of χ that satisfies the assumption $\chi \gg 1$ was chosen to be 10, and has been used throughout this thesis unless otherwise specified.

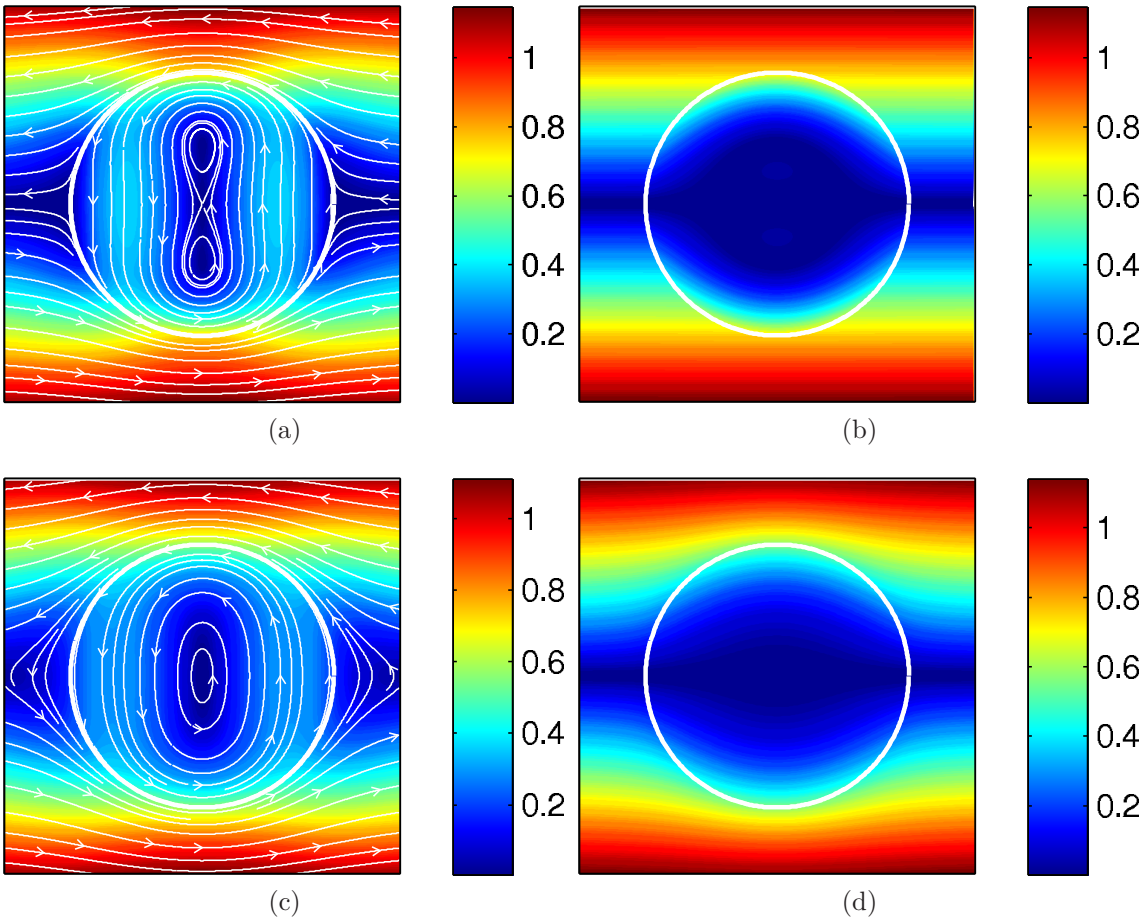

Figure 15: Streamlines and magnitude of the velocity field for an unbounded droplet in a shear flow with $\tau_{12} = 1$ and $\delta = 1.5$. Panels (a) and (b) show the streamlines and magnitude of the velocity field in the $y = 0$ and $x = 0$ plane for $\alpha_3 = 0.01$. Panels (a) and (b) show the streamlines and magnitude of the velocity field in the $y = 0$ and $x = 0$ plane for $\alpha_3 = 1$.

As illustrated by the streamlines of Fig. 15, the topology of the interior flow (79) is solely determined by the viscosity ratio of the droplet and substrate α_3. For values of $\alpha_3 \ll 1$, there are three fixed points aligned along the z-axis (e. g. Fig. 15a). As α_3 is increased, the two elliptic fixed points approach the hyperbolic fixed point at the center of the drop. This behavior continues until, for values of $\alpha_3 \approx \mathcal{O}(1)$, there remains only one fixed point at the center of the droplet which is an elliptic fixed point. Changes to any of the other parameters, such as τ_{12}, only affect the magnitude of the velocity field and not its topology.

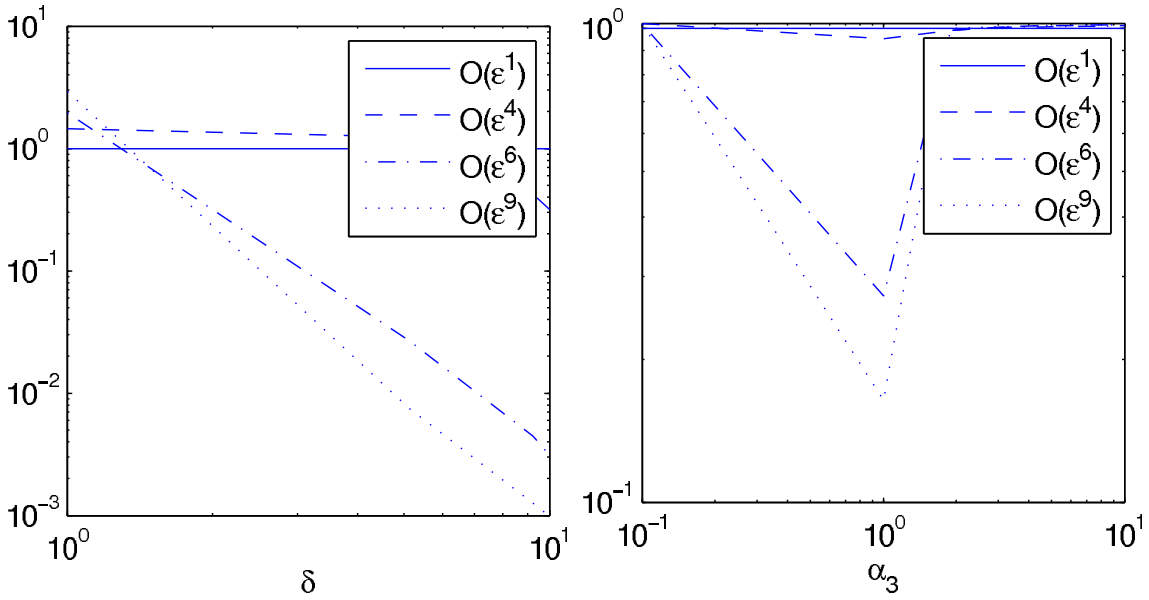

(a) (b)

Figure 16: Variations in the integrated residual at the drop-substrate interface for solutions with increasing truncation order. (a) Residual as a function of δ, evaluated at $\alpha_3 = \tau_{12} = 1$. (b) Residual as a function of α_3, evaluated at $\delta = 1.25$ and $\tau_{12} = 1$.

The contributions to the velocity field from the first reflection do not satisfy boundary conditions at interface $\partial\Omega_p$. To simultaneously satisfy boundary conditions up to $\mathcal{O}(\epsilon^9)$ at both interfaces, a total of eight modes in Lamb's solution and four reflections about each interface were required. The coefficients of Lamb's solution are listed in the Appendix A. Once again, the velocity field inside of the droplet is determined by direct substitution of the coefficients into Lamb's solution. The velocity field exterior to the droplet is determined by substitution of the coefficients into Lamb's solution, and then superimposing that expression with its reflection about $\partial\Omega_p$.

The accuracy of this solution is judged by an examination of the error (61) and residual (63). The variation in the residual for different values of δ and α_3 is illustrated in Fig. 16.

The effect of the interface $\partial\Omega_p$ on the velocity field inside the droplet is determined by evaluation of the field with different values of the scaled submersion depth δ. For $\alpha_3 = 1$, as the droplet approaches $\partial\Omega_p$, the velocity field directly above the droplet

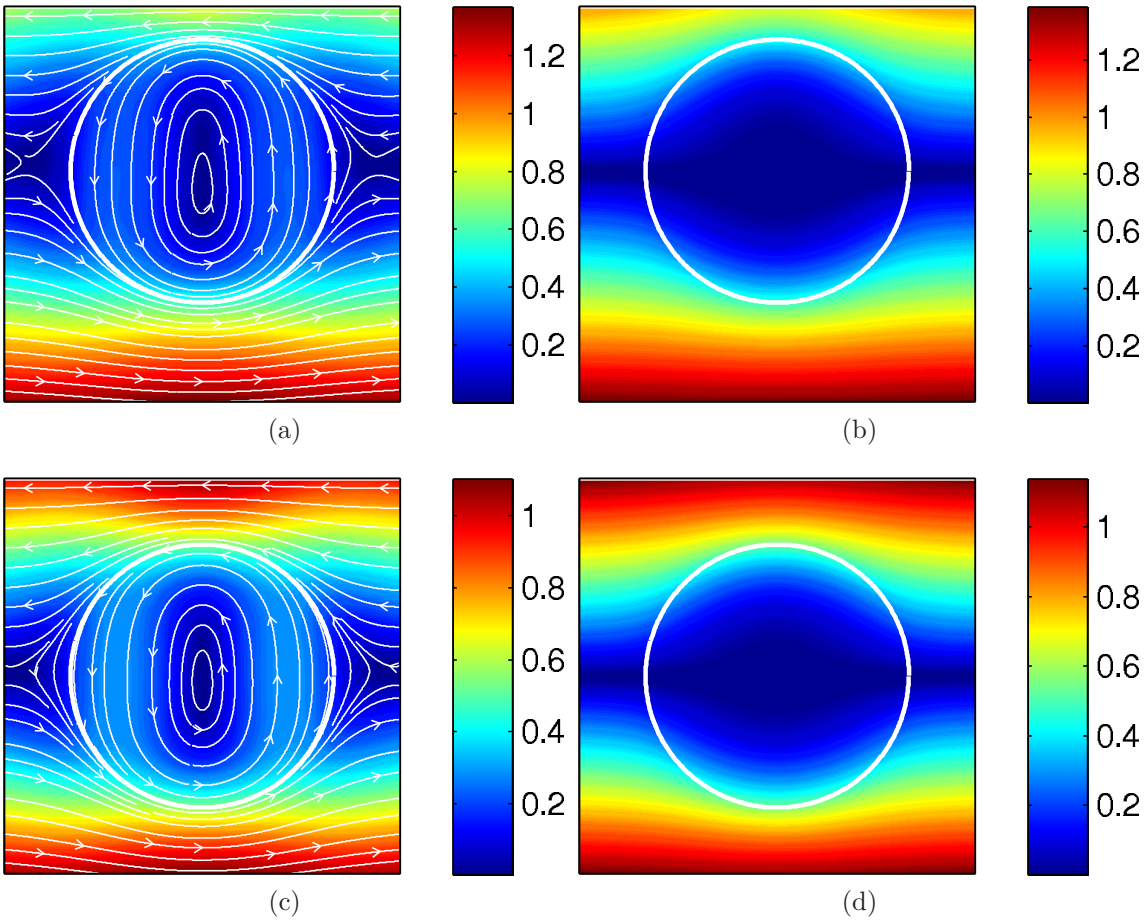

Figure 17: The effect of δ on the velocity field, as illustrated with streamlines (y=0) and level sets (x=0) for $\alpha_3 = \tau_{12} = 1$. Panels (a) and (b) correspond to $\delta = 1.25$. Panels (c) and (d) are for the value of $\delta = 1.5$.

decreases in magnitude. This is illustrated in Fig. 17, where streamlines and level sets of the velocity field are shown for two different values of δ. The interior streamlines of the droplet resemble that of an unbounded drop in a constant shear flow. The only visible difference is the slight shift of the elliptic fixed point below the center of the drop for $\delta = 1.25$, as seen in Fig. 17a.

For smaller values of α_3, the effect of the interface $\partial\Omega_p$ on the interior velocity field appears similar to that for larger values of $\alpha_3 = 1$, a slight shift in the location of the fixed points (Fig. 18). However, the streamlines external to the droplet show regions of recirculation to the left and right of the droplet. Inside the droplet, where this region contacts the surface of the drop, are found spiral fixed points. The left

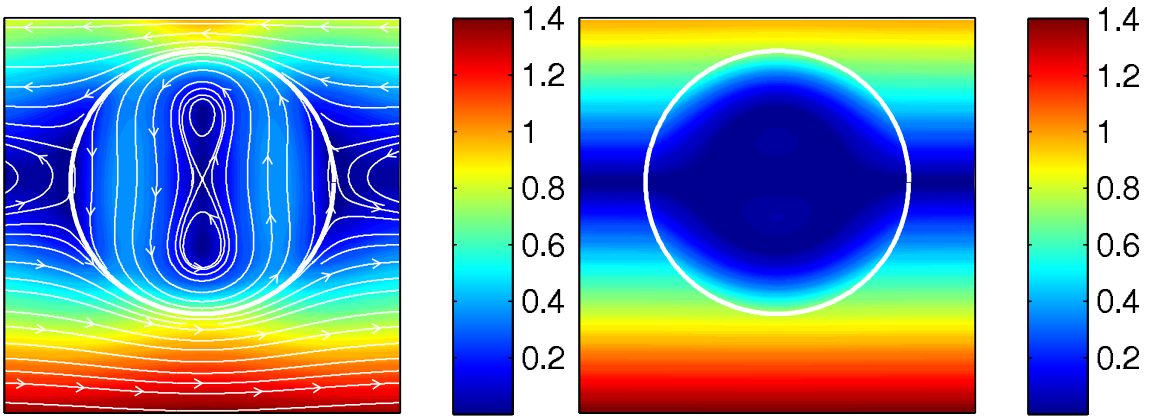

(a) (b)

Figure 18: The effect of δ on the velocity field, as illustrated with streamlines (y=0) and level sets (x=0) for $\alpha_3 = 0.01$ and $\tau_{12} = 1$. The recirculation zones to the left and right of the drop are clearly visible. (a) Streamlines and magnitude of the velocity field in the $y = 0$ plane. (b) Level sets of the velocity field in the $x = 0$ plane.

unstable spiral fixed point is shown in Fig. 19b. Fig. 19a shows this same region for an unbounded drop in a shear flow, which does not contain a spiral fixed point.

The migration velocity of an unbounded droplet, subject to the shear flow (78), is given by

$$u^{1d} = -\tau_{12}\left(\frac{\chi}{4} - \delta + \frac{3\delta^2}{4\chi}\right). \tag{80}$$

Not surprisingly, the droplet is simply advected by the asymptotic shear flow of the liquid layer. The dominant contribution to the migration velocity is thus determined by the scaled substrate thickness χ. The physical properties of the droplet have no impact on the migration velocity, and will only become important when considering additional reflections from the interfaces.

When the interaction between the air-substrate interface and the droplet are taken into account, the mobility function is used to determine the effect of the interface on

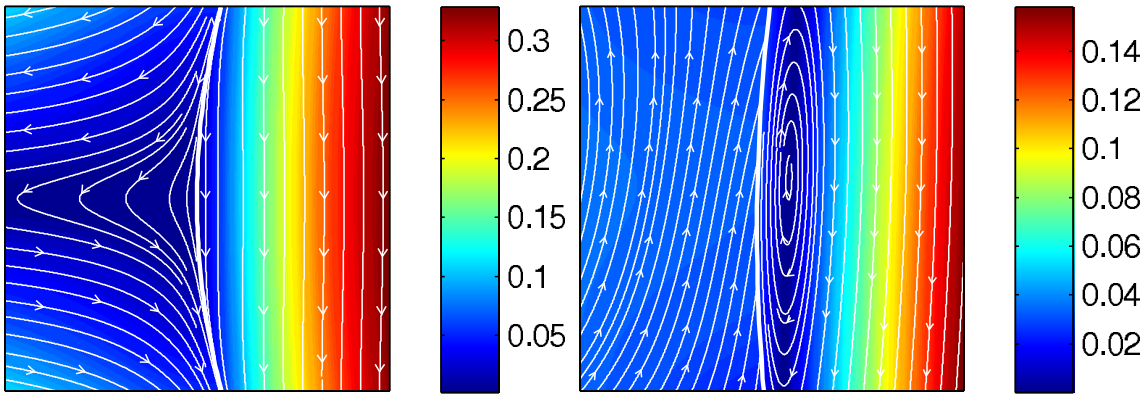

(a) (b)

Figure 19: The velocity field near the left side of the droplet. For small droplet viscosity, a submerged droplet will contain to spiral fixed points. (a) A droplet in an unbounded substrate. (b) A small spiral is observed when a droplet migrates near teh air-substrate interface $\partial\Omega_p$. For both cases common values of $\alpha_3 = 0.01$ and $\tau_{12} = 1$ were used.

the migration velocity of the droplet. Here the mobility function is given by

$$\begin{aligned} M = 1 + \Bigg[& \left(2\,\frac{(5\,\alpha_3+2)^2\,(13\,\alpha_3+2)\,\chi}{(3\,\alpha_3+2)\,(\alpha_3+1)^2} - 3\,\frac{(\alpha_3+4)\,(24\,\alpha_3+11)\,\alpha_3}{(\alpha_3+1)^2\,(2\,\alpha_3+5)} \right)\epsilon^8 + \\ & + \left(-8\,\frac{\alpha_3\,(5\,\alpha_3+2)\,(\alpha_3-1)^2\,\chi}{(\alpha_3+4)\,(3\,\alpha_3+2)\,(\alpha_3+1)^2} - 3/2\,\frac{(5\,\alpha_3+2)^2\,(13\,\alpha_3+2)}{(3\,\alpha_3+2)\,(\alpha_3+1)^2} \right)\epsilon^7 + \\ & + \left(6\,\frac{\alpha_3\,(5\,\alpha_3+2)\,(\alpha_3-1)^2}{(\alpha_3+4)\,(3\,\alpha_3+2)\,(\alpha_3+1)^2} \right)\epsilon^6 + \left(32\,\frac{(1+2\,\alpha_3)\,\alpha_3\,\chi}{(\alpha_3+1)\,(3\,\alpha_3+2)} \right)\epsilon^4 - \\ & - \left(24\,\frac{\alpha_3\,(1+2\,\alpha_3)}{(\alpha_3+1)\,(3\,\alpha_3+2)} \right)\epsilon^3 \Bigg] \times \left(\frac{\epsilon^2}{-3+8\,\chi\,\epsilon-4\,\chi^2\epsilon^2} \right) + \mathcal{O}\left(\epsilon^9\right). \end{aligned} \tag{81}$$

The migration velocity of the unbounded drop and its corrections are proportional to τ_{12}. As a result, the mobility function will be independent of this parameter. The dependence of the mobility function (81) on the remaining parameters (δ, χ and α) is illustrated in Fig. 20.

Regardless of the choice of parameters, the effect of reflections is to retard the migration velocity of the droplet; in some cases by as much as five percent. This effect is more pronounced for a droplet that moves closer to $\partial\Omega_p$ (e. g., for smaller values of δ) and less pronounced for deeper substrates (e. g., for larger values of χ).

Of all the parameters, the viscosity ratio (α_3) is found to have the largest effect

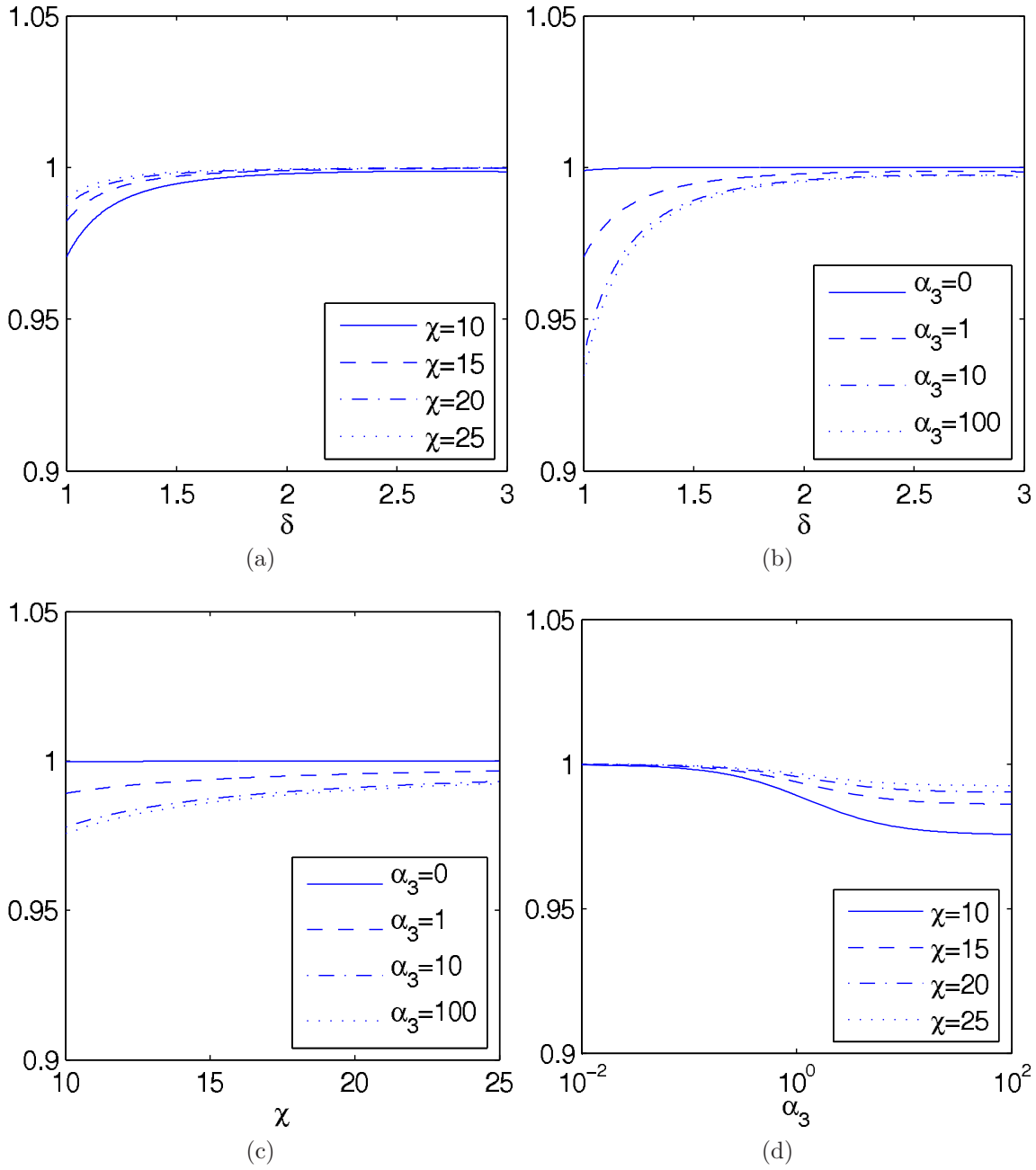

Figure 20: The dependence of the mobility function on δ, χ and α. Panel (a) $\alpha_3 = 1$, Panel (b) $\chi = 10$, Panel (c) $\delta = 1.25$ and Panel (d) $\delta = 1.25$

on the mobility function. Fig. 20b and 20d indicate that droplets with large viscosity ratios tend to move more slowly than those with small ratios. This is in stark contrast to the behavior of the mobility function found for $\tau_{12} = 0$ (73), which showed an increase for large values of α_3.

3.7.3 The complete solution

In practice, surface tension gradients exist simultaneously at both interfaces. Each of these gradients will contribute to the velocity field. The parameter τ_{12} determines the relative magnitude of these contributions. For small values of τ_{12}, velocity contributions from interface $\partial\Omega_d$ dominate. For large values of τ_{12}, velocity contributions from interface $\partial\Omega_p$ dominate. In this section, two important questions are addressed: what new states (topologically) does the combined velocity field exhibit for intermediate values of τ_{12}, and how additional corrections from reflections about the interfaces affect these intermediate states?

For a moment, consider neglecting all corrections from reflections about the interfaces. For very small values of τ_{12}, the interior velocity field resembles that counter-rotating dipole flow (Fig. 12); discussed in Section 3.7.1. For a very large τ_{12} the interior velocity resembles recirculation flow in Fig. 15; discussed in Section 3.7.2. As τ_{12} is increased from zero, a fixed point in the $y = 0$ plane and exterior to the droplet approaches from below. Shown in Fig. 21, this fixed point is a hyperbolic fixed point for small values of α_3, and an elliptic fixed point for large values of α_3. Simultaneously, an elliptic fixed point in the interior of the droplet approaches the bottom surface of the drop.

As τ_{12} is increased further, the fixed points on either side of the bottom surface of the drop combine. In the case of large α_3 (Fig. 21b), what remains is the flow field of Fig. 15c, an interior flow rotating counterclockwise around a single elliptic fixed point. This structure does not change for further increases in τ_{12}.

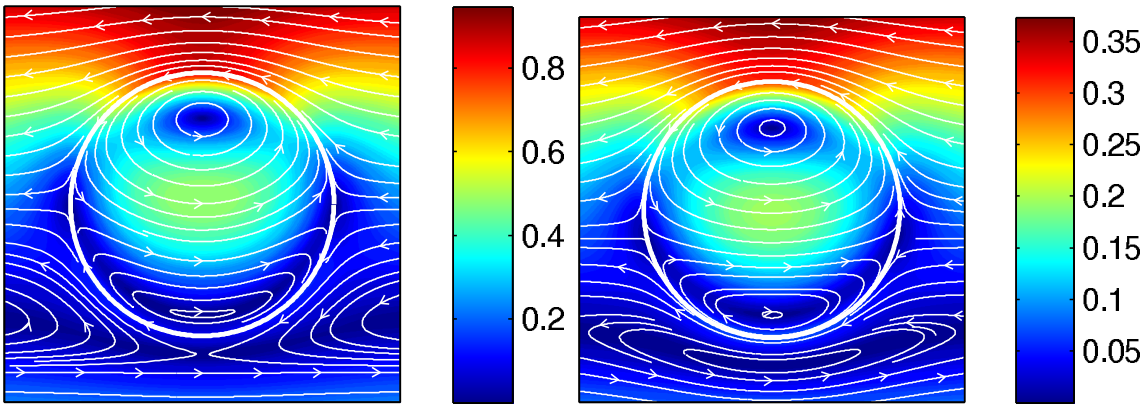

(a) (b)

Figure 21: Combined velocity field for different values of α_3. The hyperbolic and elliptic fixed points are clearly visible below the droplet. Panel (a) $\alpha_3 = 0.01$ and $\tau_{12} = 0.5$. Panel (b) $\alpha_3 = 1$ and $\tau_{12} = 0.2$.

For small values of α_3, the hyperbolic and elliptic fixed point combine to create a pair of fixed points on either side of the droplet (Fig. 21a). Each pair consist of a hyperbolic fixed point on the surface of the drop and a spiral fixed point near the inside surface of the droplet. Streamlines and level sets for this flow are shown in Fig. 22. The topological structure of Fig. 22 is distinct from those determined previously. The interior fixed point on the right, is a stable spiral while the one on the left is an unstable spiral. These spirals are connected by two heteroclinic orbits, one of which is visible in the $y = 0$ plane. The other heteroclinic connection, not shown in the figure, arcs out of the $y = 0$ plane from the stable spiral and crosses the $x = 0$ plane before terminating at the unstable spiral.

The heteroclinic orbit (not in the $y = 0$ plane) connecting the spiral fixed points of Fig. 22 organizes a bundle of similar orbits that spiral around the heteroclinic orbit before terminating in the $y = 0$ plane. This is illustrated in Fig. 23 where the heteroclinic orbits are shown in blue and the trajectories near these orbits are red. The remaining elliptic fixed point located near the top of the droplet belongs to a line of fixed points located in the $x = 0$ plane, visible as the dark blue line in Fig. 22b. This line of fixed points organizes the flow in the remainder of the droplet in the same

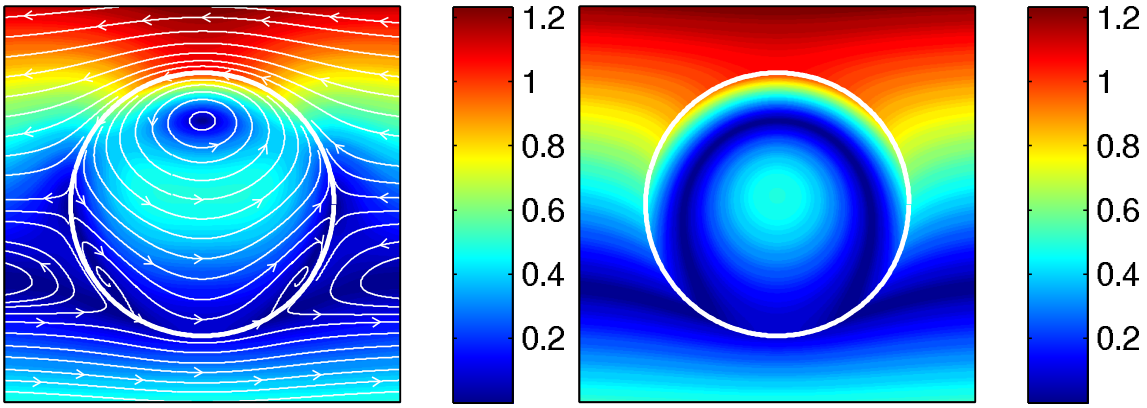

(a) (b)

Figure 22: Streamlines and level sets of the combined velocity field for $\alpha_3 = 0.01$ and $\tau_{12} = 0.75$. Panel (a) $y = 0$. Panel (b) $x = 0$.

way seen in the $y = 0$ plane, such as in Fig. 22a.

As τ_{12} is further increased, the spiral fixed points migrate up the sides of the droplet until they reach the hyperbolic fixed points located about halfway up the surface of the droplet. These fixed points combine and result in a single hyperbolic fixed point on both sides of the drop, similar to Fig. 15c. As τ_{12} is further increased, the elliptic fixed point located in the interior of the drop slowly drifts down towards the center of droplet until at last a hyperbolic and elliptic fixed point pair emerges near the center of the droplet. The structure of the flow is now identical to that of Fig. 15a.

When the corrections in the form of reflections from both interfaces are included, the structure of the velocity field remained mostly unchanged. Only small changes to the magnitude of the field is discernible. One minor exception to that is when α_3 is small. In this case, when corrections are included, the complex of hyperbolic and spiral fixed points shown in Fig. 22 does not disappear as τ_{12} is increased. Instead, this structure remains and the trio of elliptic and hyperbolic fixed points appear near the center of the drop. The final structure of the velocity field is topologically identical to that of Fig. 12a.

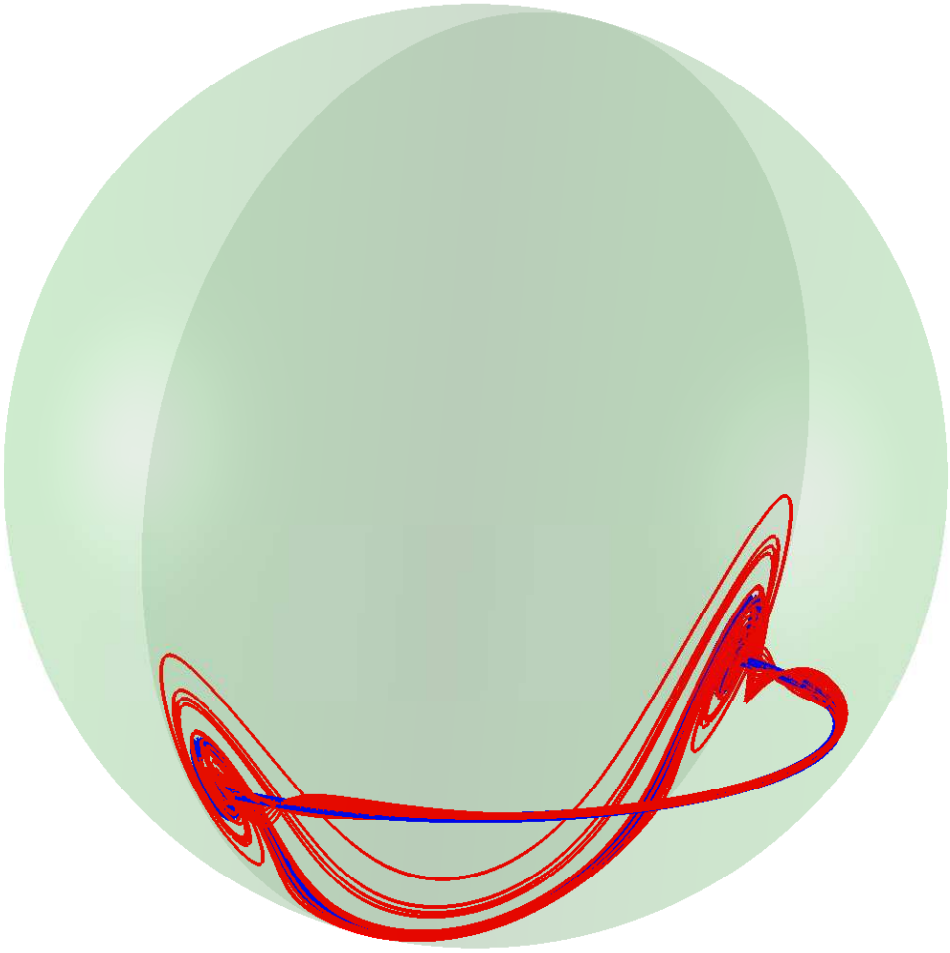

Figure 23: A three-dimensional view of the heteroclinic orbits connecting the spiral fixed points, shown here in blue. Neighboring trajectories will be organized by the heteroclinic connections and are shown in red. The surface of the droplet and the $y = 0$ plane are shown in green

3.8 Conclusion

In this chapter, the temperature and velocity field of a droplet migrating parallel to a fluid-fluid interface in a temperature gradient were found. This represents the first successful solution for this problem. It was found by using the method of reflections, independently satisfying the discontinuity in the tangential stress at each interface and superimposing the results in the limit when the thermal conductivity ratios of the substrate and droplet were equal. For a thermal conductivity ratio far from unity, a boundary integral formulation becomes necessary. An explicit analytic result for such integrals has not yet been found. When employing the method of reflections it was determined that the lower the order of the first correction, the more reflections about the air-substrate interface would be necessary.

The dependence of the resultant velocity field on parameters of the system was determined by studying the change in the migration velocity and flow structures for various values of the parameters. In general, it was found that a droplet submerged near a planar interface would migrate more slowly than one in an unbounded medium. The predicted thermocapillary migration velocity predicted by Chen [6] was found to be in error. Though the differences in Chen's results and those found here were small, it was seen that even small differences predicted the wrong qualitative behavior for a gas bubble. Chen's solution did not include the effects of thermocapillary stress at the air-substrate interface on the velocity field. For this case, the differences flow fields, between Chen and this research, are glaringly large.

While generally successful at predicting flow fields and migration velocities, the submerged droplet model was struck with one limitation. When nonuniform surface tension gradients were found at the air-substrate interface only a partial solution was possible. This is one of the situations where a numerical scheme will be needed to obtain a quantitatively accurate solution.

This study was motivated by the problem of efficient mixing in a microfluidic

device. Including the effects of thermal and hydrodynamic interactions between the droplet and planar interface did not result in flow structures significantly different from those studied in the simple model originally proposed by Grigoriev [10]. However, there still remain significant differences between a droplet floating at the surface of a liquid and one entirely submerged with in the liquid. To judge the effect of such differences on the flow structures, and how well the submerged droplet models a floating droplet, a numerical scheme will be required to solve for the velocity field. This will be the the topic of the following two chapters.

CHAPTER IV

MOTION OF AN INTERFACIAL DROPLET

4.1 Introduction

This chapter deals with the motion of a fluid droplet confined to move at the interface between two immiscible fluids. As seen in Fig. 24, the interfacial droplet floats at a free surface a distance H above a solid boundary. All three fluids are subject to an imposed temperature field far from the droplet. The temperature and velocity fields, along with the migration velocity of the droplet, are found numerically using a boundary collocation technique. For the case where the covering fluid (fluid 1) is air, results here compared with the submerged drop model of Chapter 3.

In the previous chapter the method of reflections was used to obtain an analytic model for the flow inside a droplet that migrated fully submerged below the air-substrate interface. This model was developed to analyze the flow in an optically controlled microfluidic device [11]. However, in experiments [11] the droplet straddles the air-substrate interface. This significantly complicates the problem in several ways. First, the shape of the droplet must be determined by the three interfacial surface tensions. In general, the shape of the droplet will not be spherical. Second, the presence of a contact line (i. e., the line where the three fluids contact each other) both affects the total force on the droplet and places additional constraints on the velocity field. Last, but certainly not least, the incorporation of a third liquid (fluid 1) covering the top portion of the droplet introduces a discontinuity in the interfacial properties of the droplet at the contact line and also introduces a whole slew of new dimensional parameters and scales.

While approximate analytical methods can provide valuable knowledge in certain

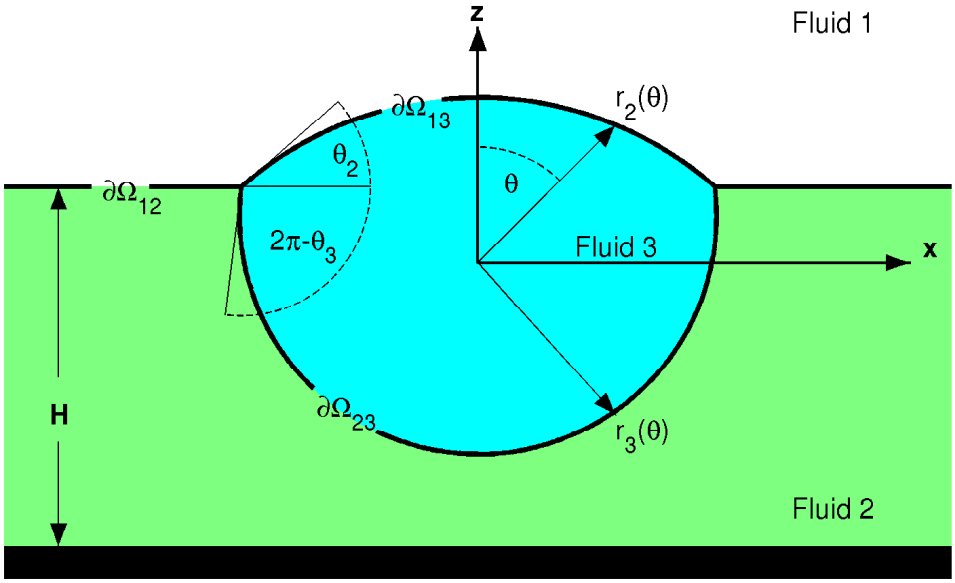

Figure 24: A view of the interfacial drop in the (x, z) plane (not to scale). We take the z axis to be vertical and the x axis to point in the direction of the temperature gradient.

limiting cases (e. g. lubrication analysis for very slender droplets or Lamb's expansion for nearly spherical drops), a solution for the general case can only be obtained numerically. Despite the departure of the drop shape from a sphere, Lamb's general solution is used to represent the interior flow. The coefficients being determined numerically by boundary collocation, where boundary conditions are enforced at specified locations on the interfaces. The advantages of this method are twofold. First, the solution is analytic everywhere in space and no interpolation or mesh refinement is necessary. Second, because both this solution and the solution by the method of reflections consist of Lamb modes, it is possible to make a direct comparison between the two solutions.

It must not be overlooked that the study of interfacial drops is interesting and worthwhile in its own right. There has been only a handful of studies examining interfacial droplet motion. One study by Pozrikidis [33], examined a solid spherical particle that equally straddled a fluid-fluid interface. Another study examined fluid

motion resulting from surface tension gradients, Ref. [35]. The more general results of this thesis will therefore fill a gap in the literature of thermocapillary phenomena. This is not to diminish the motivation that prompted this thesis, accurate modeling of the flow in a new breed of microfluidic devices. In fact, the next chapter will deal exclusively with predictions for what an experimenter should observe for migration velocities and flow fields.

4.2 Governing Equations and Boundary Conditions

The governing equations and boundary conditions for an interfacial drop are an extension of the equations of Chapter 3 from two to three fluids. Consider a droplet floating at the surface of the liquid layer analyzed in Chapter 2. As illustrated in Fig. 24 the covering fluid, labeled fluid 1, is unbounded above and bounded below by $\partial\Omega_{12}$. The substrate liquid, fluid 2, is bounded above by $\partial\Omega_{12}$ and below by a parallel solid surface a distance H from the interface. At interface $\partial\Omega_{12}$ is confined an immiscible droplet designated as fluid 3. This droplet is bounded above by interface $\partial\Omega_{13}$ and below by interface $\partial\Omega_{23}$. The origin for this coordinate system is set at the center of mass of the droplet. Aside from a simple relabeling of the interfaces, things look rather similar to the fully submerged droplet of Chapter 3.

Since this study is primarily driven by microfluidic applications, velocities and length scales are assumed small enough for convective momentum and energy transport to be negligible. In the limit of vanishing Reynolds number, $Re = 0$, the velocity fields in all three fluids are governed by the Stokes equation subject to the incompressibility condition

$$\nabla \cdot \mathbf{V_i} = 0, \tag{82a}$$

$$\mu_i \nabla^2 \mathbf{V_i} = \nabla p_i, \tag{82b}$$

where μ_i is the dynamic viscosity of the i^{th} fluid. Correspondingly, in the limit of vanishing thermal Péclet numbers, $Pe = 0$, the temperature field in each fluid must

satisfy Laplace's equation

$$\nabla^2 T_i = 0. \tag{83}$$

Unlike the analysis of the submerged droplet, the covering fluid (fluid 1) is not assumed to be air, and the temperature and velocity field in that fluid will be part of the general solution.

The boundary conditions at $\partial\Omega_{12}$ and $\partial\Omega_{23}$ are identical to those given in Chapter 3. Likewise, a similar set of boundary conditions are now required at the interface $\partial\Omega_{13}$. The boundary conditions for all interfaces are given below. For the temperature field at the interface $\partial\Omega_{ij}$ (see Fig. 24), the continuity of the temperature field and the heat flux must be enforced

$$(T_j - T_i)|_{\partial\Omega_{ij}} = 0, \tag{84a}$$

$$(k_j \nabla T_j - k_i \nabla T_i) \cdot \hat{\mathbf{n}}|_{\partial\Omega_{ij}} = 0 \tag{84b}$$

where k_i is the thermal conductivity and the normal vector $\hat{\mathbf{n}}$ points from fluid i into fluid j. Furthermore, at $\partial\Omega_{ij}$ the normal component of the velocity must vanish and the tangential component of the velocity must be continuous

$$\mathbf{V}_j \cdot \hat{\mathbf{n}}|_{\partial\Omega_{ij}} = \mathbf{V}_i \cdot \hat{\mathbf{n}}|_{\partial\Omega_{ij}} = 0, \tag{85a}$$

$$(\mathbf{V}_j - \mathbf{V}_i) \times \hat{\mathbf{n}}|_{\partial\Omega_{ij}} = 0, \tag{85b}$$

where the position of the interface is assumed stationary (the reference frame is chosen to be that of the droplet). Finally, the jump in the tangential and normal components of the stress must balance the surface tension at the interface

$$\hat{\mathbf{n}} \cdot (\mathbf{\Sigma}_j - \mathbf{\Sigma}_i) \times \hat{\mathbf{n}}|_{\partial\Omega_{ij}} = -\nabla\sigma_{ij} \times \hat{\mathbf{n}}, \tag{86a}$$

$$\hat{\mathbf{n}} \cdot (\mathbf{\Sigma}_j - \mathbf{\Sigma}_i) \cdot \hat{\mathbf{n}}|_{\partial\Omega_{ij}} = \sigma_{ij} \cdot (\nabla \cdot \hat{\mathbf{n}}). \tag{86b}$$

All physical properties of the fluids, except for surface tension, are assumed to be independent of temperature. Surface tension is assumed to vary linearly with

temperature and is given by

$$\sigma_{ij}(T) = \bar{\sigma}_{ij} + \sigma'_{ij}(T - T_0), \tag{87}$$

where $\bar{\sigma}_{ij}$ is the value of the surface tension at the interface between fluids i and j at the reference temperature T_0 (taken as the instantaneous temperature at the origin) and σ'_{ij} is the corresponding temperature coefficient.

As an additional consequence of restricting this research to the study of small droplets, it is safe to assume that the temperature variation to be small near the droplet (where the curvature $\nabla \cdot \hat{\mathbf{n}}$ is large), so that the stress boundary condition (86) can be rewritten as

$$\hat{\mathbf{n}} \cdot (\boldsymbol{\Sigma}_j - \boldsymbol{\Sigma}_i) \times \hat{\mathbf{n}}|_{\partial\Omega_{ij}} = -\sigma'_{ij} \nabla T_i \times \hat{\mathbf{n}}, \tag{88a}$$

$$\hat{\mathbf{n}} \cdot (\boldsymbol{\Sigma}_j - \boldsymbol{\Sigma}_i) \cdot \hat{\mathbf{n}}|_{\partial\Omega_{ij}} = \bar{\sigma}_{ij} \cdot (\nabla \cdot \hat{\mathbf{n}}). \tag{88b}$$

4.3 Flow Far From The Droplet

The introduction of a droplet of characteristic size r_0, small when compared with both l_0 (13) and the depth of the substrate H, will distort the temperature and velocity fields near the droplet. Far from the droplet (i. e. for $r_0 \ll |\mathbf{x}| \lesssim l_0$) the fields will remain unchanged. The velocity and temperature far from the droplet was derived in the liquid layer analysis of Chapter 2. There, however, the covering liquid (fluid 1) was taken to be air. This permitted a solution for the temperature and velocity field to be restricted to that of the substrate, simplifying the problem. In this chapter the covering fluid is not restricted to that of air. This permits analysis of the more general problem of an interfacial droplet trapped between two arbitrary fluids.

Determining the temperature and velocity fields in a two-phase liquid layer (one layer atop another) is accomplished by exactly the same procedure that was used in the single layer analysis (see Sections 2.4 and 2.5). To recover a velocity field in fluid 1 applicable to the geometry of the interfacial droplet system, the thickness of the

covering fluid is taken to approach infinity. In this limit the temperature and velocity field in the substrate remain unchanged from Eqs. (33,34). Just as in the submerged droplet model the no-slip boundary condition (7) at the solid bottom boundary will not be explicitly enforced. Instead, analysis will be restricted to the typical case $r_0 \ll H$ where (7) is satisfied automatically as a consequence of (34).

The asymptotic flow (34) in fluid 2 used for the interfacial droplet system was defined in Chapter 3. There, Eq. (34) contained the parameter δ, the submersion depth of the spherical droplet. For interfacial droplets it was replaced with the vertical distance z_1 from interface $\partial\Omega_{12}$ to the center of mass of the droplet. For an interfacial droplet $z_1 \leq \mathcal{O}(1)$. Utilizing the condition that $r_0 \ll H$, Eq. (34) is further simplified to

$$V_2^\infty = \frac{\sigma'_{12}\Theta}{\mu_2}\left((z - z_1) + \frac{H}{4}\right)\hat{\mathbf{x}}, \tag{89}$$

when evaluated near the interface $\partial\Omega_{12}$. In the covering fluid the temperature and velocity fields are simplified even further to

$$T_1^\infty = T_0 + \Theta x, \tag{90}$$

$$\mathbf{V_1^\infty} = \frac{\sigma'_{12}H\Theta}{4\mu_2}\hat{\mathbf{x}}. \tag{91}$$

It is easy to check that the equations (82) and (83), the boundary conditions (84),(85), and (88) at the free interface $\partial\Omega_{12}$ are all satisfied by the above temperature and velocity fields.

For convenience, the reference frame is chosen to move at the steady-state migration velocity of the droplet. The symmetry of the system with respect to the y axis and the symmetry of the asymptotic fields implies that the droplet moves along the x axis. Switching to a reference frame moving with velocity $\mathbf{U_0} = U_0\hat{\mathbf{x}}$, the following boundary conditions are obtained

$$T_i \to T_i^\infty, \qquad |\mathbf{x}| \to \infty, \tag{92a}$$

$$\mathbf{V}_i \to \mathbf{V}_i^{\infty} - \mathbf{U_0}, \qquad |\mathbf{x}| \to \infty, \tag{92b}$$

for $i = 1, 2$. In this reference frame all interfaces are stationary and the boundary condition (85a) is applicable.

4.4 The Droplet Shape

The temperature and velocity field for an interfacial droplet are characterized by several important scales and dimensionless numbers inherent to this system. These are the same scales defined during the derivation of the fully submerged droplet model, now generalized to three fluids. For the flow far from the droplet the characteristic length and velocity scales remain H and v_0^{∞} (91), the substrate thickness and the asymptotic velocity field evaluated at the planar interface. Near the droplet the scales are r_0 and v_0. The velocity scale v_0 is given by Eq. (37) and is characteristic of the thermocapillary stress at the bottom surface of the droplet. Using these scales the Reynolds and Péclet numbers for each fluid are defined as

$$Re_i = \frac{l_i v_i \rho_i}{\mu_i}, \tag{93}$$

$$Pe_i = \frac{l_i v_i \rho_i C_{p,i}}{k_i}. \tag{94}$$

In both definitions the respective values of the densities ρ_i, viscosities μ_i, thermal conductivities k_i, and heat capacities $C_{p,i}$ are used for each fluid. The corresponding length scales are $l_1 = l_2 = H$, $l_3 = r_0$ and the velocity scales are $v_1 = v_2 = v_0^{\infty}$, $v_3 = v_0$.

The same caveat of Chapter 3 regarding the potential differences in magnitude of the Reynolds and Péclet numbers for different fluids will apply to an interfacial droplet system. Just as with the submerged drop model, the magnitude of Re_i and Pe_i will become arbitrarily small as the imposed temperature gradient Θ is reduced. Any requirement on the smallness of the dimensionless parameters can thus be completely justified by requiring an appropriate decrease in the imposed temperature gradient.

Characterization of the droplet shape requires the introduction of the capillary and Bond numbers. The capillary numbers are defined for each fluid as:

$$Ca_i = \frac{\mu_i v_0}{\bar{\sigma}_i}, \qquad \bar{\sigma}_i = \begin{cases} \bar{\sigma}_{i3}, & i = 1, 2, \\ \bar{\sigma}_{23}, & i = 3. \end{cases} \tag{95}$$

and are all of the same order of magnitude in the typical case when the surface tensions and viscosities of all three fluids are comparable. The Bond numbers are similarly defined as

$$Bo_i = \frac{\rho_i g r_0^2}{\bar{\sigma}_i}, \tag{96}$$

where g is the gravitational acceleration and $\bar{\sigma}_i$ is defined as in (95). Here, again, the Bond numbers are all of the same order of magnitude for fluids with comparable densities and surface tensions. For typical fluids they quickly become very small as the droplet size decreases.

The position of the interfaces, determining both the droplet shape and the shape of the surface of the substrate fluid, is found by solving the normal stress balance equation (88b). In the limit $Bo = Ca = 0$, the normal component of the stress reduces to a constant pressure. Consequently, all three interfaces are surfaces of constant curvature. Since $\partial\Omega_{12}$ is flat far from the droplet, it has to be a horizontal flat plane $z = \text{const}$. Similarly, the top and bottom surfaces of the droplet, $\partial\Omega_{13}$ and $\partial\Omega_{23}$, will be spherical caps of constant curvature.

The contact angles that the interfaces $\partial\Omega_{13}$ and $\partial\Omega_{23}$ make with $\partial\Omega_{12}$ (see Fig. 24) are defined as θ_2 and θ_3 respectively. These angles can be determined from a simple force balance analysis at the contact line

$$\bar{\sigma}_{12} = \bar{\sigma}_{13}\cos\theta_2 + \bar{\sigma}_{23}\cos\theta_3, \tag{97a}$$

$$0 = \bar{\sigma}_{13}\sin\theta_2 + \bar{\sigma}_{23}\sin\theta_3. \tag{97b}$$

The radii of curvature, R_2 and R_3, of the top and bottom caps of the interfacial

drop, are determined by solving the Young-Laplace equation obtained from (88b)

$$\frac{\bar{\sigma}_{13}}{\bar{\sigma}_{23}} = \frac{R_2}{R_3}, \tag{98}$$

subject to the condition that the droplet volume is equal to that of a sphere of characteristic radius r_0

$$\begin{aligned} 4r_0^3 = R_2^3(2 - \cos\theta_2 + \cos^3\theta_2) + \\ + R_3^3(2 - \cos\theta_3 + \cos^3\theta_3). \end{aligned} \tag{99}$$

With the origin of the coordinate system placed at the droplet's center of mass the height of the interface $\partial\Omega_{12}$ is found to be

$$\begin{aligned} z_1 = \frac{1}{16r_0^3}(R_2^4(\cos\theta_2 + 3)(\cos\theta_2 - 1)^3 - \\ - R_3^4(\cos\theta_3 + 3)(\cos\theta_3 - 1)^3). \end{aligned} \tag{100}$$

Furthermore, interface $\partial\Omega_{13}$ is parametrized as

$$r_2(\theta) = -h_2\cos\theta + \sqrt{R_2^2 - h_2^2\sin^2\theta}, \tag{101a}$$

$$h_2 \equiv R_2\cos\theta_2 - z_1, \tag{101b}$$

and $\partial\Omega_{23}$ as

$$r_3(\theta) = -h_3\cos\theta + \sqrt{R_3^2 - h_3^2\sin^2\theta}, \tag{102a}$$

$$h_3 \equiv -R_3\cos\theta_3 - z_1, \tag{102b}$$

so that all interfaces axisymmetric with respect to the z axis. For certain values of parameters, it is more convenient to place the origin at the intersection of the z axis with the plane of the interface $\partial\Omega_{12}$, such that $z_1 = 0$. This will become apparent when deriving the total force on the droplet.

By specifying the location of all three interfaces, the location of the contact line is also uniquely determined. The contact line Γ_c is the intersection of the hemispheres $\partial\Omega_{13}$ and $\partial\Omega_{23}$. This intersection defines a circle with polar coordinates $r = r_c$ and $\theta = \theta_c$ obtained by solving $r_c = r_1(\theta_c) = r_2(\theta_c)$. Alternatively, Γ_c can be described as a circle of radius $r_c\sin\theta_c$ that lies in the plane $z = z_1 = r_c\cos\theta_c$.

4.5 Forces on the Droplet

Now that the positions of the boundaries of all three fluids have been specified, the temperature and velocity fields in each can be found by solving (82) and (83) subject to the boundary conditions stated previously. Furthermore, as the position and shape of all free interfaces have already been determined, it is no longer necessary to satisfy the normal stress balance boundary condition (88b) everywhere on each interface.

For computational purposes it will also be convenient to satisfy the following boundary conditions for the velocity fields at the contact line, which immediately follow from (85),

$$\mathbf{V}_{i,r} = \mathbf{V}_{i,\theta} = 0, \qquad i = 1, 2, 3, \tag{103a}$$

$$\mathbf{V}_{1,\phi} = \mathbf{V}_{2,\phi} = \mathbf{V}_{3\phi}, \tag{103b}$$

where the second subscript denotes the components in the polar coordinates.

As a consequence of the assumption that the droplet is stationary in the chosen reference frame, the total force on the droplet vanishes

$$\mathbf{f} = \mathbf{f}_{\text{body}} + \mathbf{f}_{\text{surface}} + \mathbf{f}_{\text{line}} = 0 \tag{104}$$

In the $Bo = 0$ limit, the body force $\mathbf{f}_{\text{body}}$ is absent and the surface force is given by

$$\mathbf{f}_{\text{surface}} = \int_{\partial\Omega_{13}} \boldsymbol{\Sigma}_1 \cdot \mathbf{n} dS + \int_{\partial\Omega_{23}} \boldsymbol{\Sigma}_2 \cdot \mathbf{n} dS. \tag{105}$$

The line force is exerted on the droplet by the surface tension at the interface $\partial\Omega_{12}$ and is found by integrating this force around the contact line

$$\mathbf{f}_{\text{line}} = \int_{\Gamma_c} \sigma_{12} d\mathbf{s} \times \hat{\mathbf{z}}, \tag{106}$$

where $d\mathbf{s} = r_c \sin\theta_c d\phi\, \hat{\phi}$. This force is nonzero due to the variation in the surface tension along the contact line. Because the surface tension is larger where the fluid is at a lower temperature, the contact line force will pull the drop in the direction opposite to that of the imposed temperature gradient. Using (106) and (87) it is found

Table 4: Dimensionless parameters describing thermocapillary migration of an interfacial droplet subject to a horizontal temperature gradient.

	Fluid 1	Fluid 2	Fluid 3
Viscosity	$\alpha_1 = \mu_1/\mu_2$	$\alpha_2 = 1$	$\alpha_3 = \mu_3/\mu_2$
Thermal conductivity	$\beta_1 = k_1/k_2$	$\beta_2 = 1$	$\beta_3 = k_3/k_2$
Surface tension	$\gamma_{12} = \bar{\sigma}_{12}/\bar{\sigma}_{23}$	$\gamma_{13} = \bar{\sigma}_{13}/\bar{\sigma}_{23}$	$\gamma_{23} = 1$
Temperature coefficient	$\tau_{12} = \sigma'_{12}/\sigma'_{23}$	$\tau_{13} = \sigma'_{13}/\sigma'_{23}$	$\tau_{23} = 1$

that this force can be alternatively expressed as an integration of the temperature field around the contact line

$$\mathbf{f}_{\text{line}} = \sigma'_{12} r_c \sin\theta_c \hat{\mathbf{x}} \int_0^{2\pi} T \cos\phi \, d\phi. \tag{107}$$

The force constraint (104) closes the system of equations for the velocity fields, allowing the computation of the speed $\mathbf{U_0}$ of the droplet relative to the solid bottom boundary.

To minimize the number of parameters describing the problem to a minimum, the governing equations and boundary conditions are nondimensionalized. All lengths are scaled by r_0. Temperature is scaled by first subtracting the reference temperature at the center of the drop and then dividing by the characteristic temperature scale Θr_0. All velocities are scaled by the characteristic velocity v_0. All stresses, including pressure, are scaled by the typical viscous stress $\Sigma_0 = -\sigma'_{23}\Theta$. The viscosities, thermal conductivities, reference surface tensions, and temperature coefficients of surface tension are scaled by μ_2, k_2, $\bar{\sigma}_{23}$, and σ'_{23}, respectively. The corresponding nondimensional quantities are summarized in Table 4. In addition to these eight $\mathcal{O}(1)$ parameters we find two large parameters, the nondimensional temperature length scale $\lambda = l_0/r_0$ and substrate depth $\chi = H/r_0$.

4.6 Numerical Method and Procedures

4.6.1 A General Solution

The interfacial droplet system possess the same set of symmetries as the submerged drop model of Chapter 3. The general solution for the temperature field will therefore be given by

$$T_i = T_i^{\infty} + T_{out}, \quad i = 1, 2, \tag{108a}$$

$$T_3 = T_{in}, \tag{108b}$$

where T_{out} and T_{in} are the outer and inner spherical harmonic expansion given in Eqs. (33). The asymptotic form of the temperature field as been explicitly added to the general solution, automatically satisfying boundary conditions far from the droplet. Lamb's general solution for the Stokes equation is again used for determining the velocity field. By virtue of the similarities in the symmetries (say that fast three times!) between the submerged and interfacial drop, the general solution for the velocity field is given by

$$\mathbf{V}_i = \frac{\mathbf{V}_i^{\infty} - \mathbf{U}_0}{v_0} + \mathbf{V}_{out}, \tag{109a}$$

$$p_i = p_{out}, \tag{109b}$$

for the nondimensional velocity and pressure fields in the outer fluids, $i = 1, 2$, and

$$\mathbf{V}_3 = -\frac{\mathbf{U}_0}{v_0} + \mathbf{V}_{in}, \tag{110a}$$

$$p_3 = p_{in}, \tag{110b}$$

for the nondimensional velocity and pressure fields in the inner fluid. In Eq. (110b) the constant hydrostatic pressure p_0 inside the drop is determined by the Young-Laplace equation at the surface of the droplet to be

$$p_0 = \frac{2}{R_3 Ca_2}. \tag{111}$$

In defining the general solution for both the temperature and velocity fields, different sets of coefficients are used for fluids 1 and 2.

4.6.2 Computation of the Forces on the Droplet

The contact line force (107) can be computed analytically by substituting the expansion for the temperature field inside the droplet and evaluating the integral:

$$\mathbf{f}_{\text{line}} = -\pi\tau_{12} r_c \sin\theta_c \sum_{n=1}^{N} A_3^n r_c^n P_n^1(\cos\theta_c)\hat{\mathbf{x}}. \tag{112}$$

The surface force (105) can be broken up into two contributions: the force due to the asymptotic velocity field $\mathbf{V}^\infty$ and the force due to the correction $\mathbf{V}^* = \mathbf{V} - \mathbf{V}^\infty$ arising due to the presence of the droplet. The first contribution is independent of the unknowns and is calculated analytically:

$$\mathbf{f}^\infty_{\text{surface}} = \pi\tau_{12}(r_c \sin\theta_c)^2\hat{\mathbf{x}}. \tag{113}$$

In calculating the force on the droplet from $\mathbf{V}^*$ one of two approaches is taken. If the interface $\partial\Omega_{12}$ is chosen to coincide with the plane $z = 0$ (i. e. , if $z_1 = 0$), this force is also computed analytically exploiting the fact that in Stokes flows the stress tensor has zero divergence. Applying Stoke's theorem to transform the integral over the drop surface (105) to an integral over two hemispheres at infinity and the $z = 0$ plane, the force contribution from $\mathbf{V}^*$ is found to be

$$\begin{aligned}\mathbf{f}^*_{\text{surface}} = \Bigg[& \pi\sqrt{3}(B_1^1 + B_2^1) + \sum_{n=1}^{N} \pi \frac{n^2+1-n}{(n-1)(2n-1)n}(B_1^n - B_2^n) r_c^{-n+1} \frac{dP_n^1}{d\theta}\Big|_{\theta=\theta_c} - \\ & - \sum_{n=1}^{N} 2\pi(\alpha_1 C_1^n - C_2^n) r_c^{-n-1} \frac{dP_n^1}{d\theta}\Big|_{\theta=\theta_c} - \\ & - \sum_{n=1}^{N} \frac{\pi}{n}(\alpha_1 D_1^n - D_2^n) r_c^{-n} \left((n+1)P_n^1 - \frac{d^2 P_n^1}{d\theta^2} \right) \Big|_{\theta=\theta_c} \Bigg] \hat{\mathbf{x}}.\end{aligned} \tag{114}$$

This force calculation technique was originally introduced by Brenner [5] for calculating the force on a deformed droplet in Stokes flow. This is, however, the first time it has been applied to an interfacial droplet.

If the interface $\partial\Omega_{12}$ does not lie in the $z = 0$ plane, $\partial\Omega_{12}$ will no longer coincide with a constant value of θ. This prevents an analytic calculation of the force along

that interface. Instead, $\mathbf{f}^*_{\text{surface}}$ must be calculated numerically. Integration over ϕ can be carried out analytically, leaving only quadrature over the θ domain performed using an adaptive recursive Simpson's rule scheme. Carrying out the quadrature for each of the unknown coefficients in Lamb's solution, above and below the drop, requires the evaluation of $6N$ integrals. Where N is the truncation order in Lamb's solution. This is the costliest (in terms of computational time) component of the numerical procedure.

4.6.3 The Boundary Collocation Method

The unknown coefficients that determine the temperature and velocity fields are found by substituting the expansions (108), (109), and (110) into the boundary conditions (84), (85), (88a), (92), and (103) and imposing the zero force constraint (104). The method employed for solving the resulting system of equations is based on the boundary collocation procedure of Hassonjee, Ganatos and Pfeffer [14], which is itself a development of the approach proposed by Ganatos, Pfeffer and Weinbaum [8].

The method begins by first truncating the expansions for the temperature and velocity to N terms. For the interfacial droplet system the resulting equations are linear in either $\sin\phi$ or $\cos\phi$, so that the ϕ dependence can be immediately factored out. This results in a system of equations that depend only on θ. This system of equations is then evaluated on a grid of θ values, referred to as collocation rings and illustrated for an interfacial droplet in Fig. 25. The total number of collocation rings covering all three interfaces is defined as M. Since $\partial\Omega_1$ is unbounded, the largest ring is placed at a finite distance s_{max} from the z-axis.

The zero force constraint, together with the boundary conditions evaluated on the collocation rings, defines a system of linear equations with constant coefficients. Given N, M is chosen to be large enough to make the system overdetermined, so that the number of equations $(6M + 1)$ exceeds the number of unknowns $(12N + 1)$.

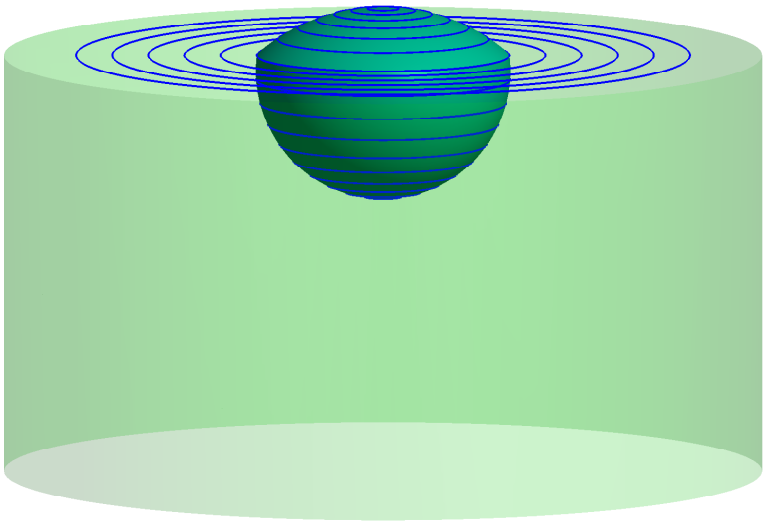

Figure 25: The boundary conditions are strictly enforced at the collocation rings (blue) on each interface (green).

The resulting system is solved in a least squares sense using Matlab's implementation of LAPACK [15], which uses Householder reflections for computing an orthogonal-triangular factorization.

To gauge the accuracy of this boundary collocation scheme, the residual R_T (defined in Eq. (63)) is calculated using the truncated solutions for the temperature and velocity fields. The normalization constant E_0 used in Eq. (63) is found by calculating the error with a solution truncated at $N = 1$. This value of the normalization constant was chosen to show the relative improvement made in keeping higher order terms in the general solution.

For a given set of dimensionless parameters, the numerical solution can depend on the choice of N, M, and s_{max}. The optimum values for N, M, and s_{max} are chosen so that R_T is minimized (holding all other parameters fixed). It was found for a generic choice of dimensionless parameters that the values $N = 50$, $M = 675$ and $s_{max} = 9$ reduced the residual by approximately 98%. Unless otherwise specified, these values

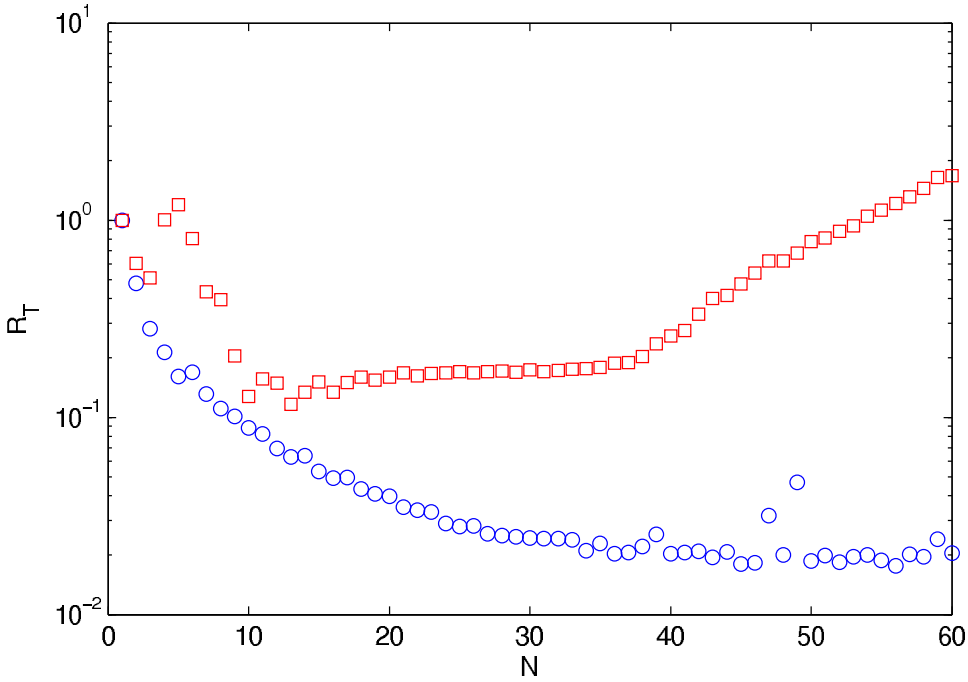

Figure 26: Residual, using a generic choice of dimensionless parameters, versus the truncation order without preconditioning (blue circles) and with preconditioning (red squares).

have been used in calculating all temperature and velocity fields.

Several different distributions for the collocation rings were tested. Ultimately a distribution with equal spacing in θ for $\partial\Omega_{13}$ and $\partial\Omega_{23}$ was chosen. For the rings on interface $\partial\Omega_{12}$ equal spacing in distance from the z-axis was used. It was found that this distribution has a slight advantage in terms of residuals and conditioning over other distributions (such as the abscissa for a Gauss-Legendre quadrature rule or equal area spacing).

The limit to the accuracy of the boundary collocation scheme was found to be set by the poor conditioning of the system at very large truncation orders. The condition number (the ratio of the largest singular value to the smallest) determines the stability of the system with respect to inversion (i. e., computing the inverse of the linear system). A typical plot of the condition number for increasing N is shown in Fig. 27 for $M = 675$. One finds a nearly exponential scaling of the condition number

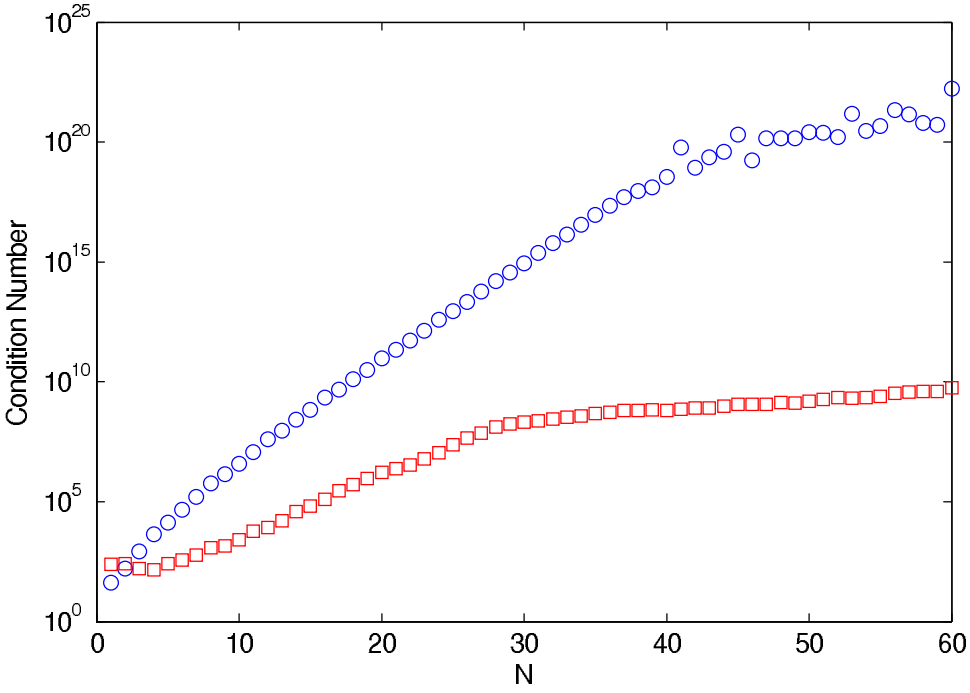

Figure 27: The condition number is found to depend strongly on the truncation order of the solution. The condition number is given without preconditioning (blue circles) and with preconditioning (red squares).

of the coefficient matrix with N. This scaling is essentially independent of the choice of dimensionless parameters not affecting the drop geometry.

One possible reason for this increasingly poor conditioning is that the orthogonality of the discretized associated Legendre functions is lost when used as basis functions for fitting. Sneeuw [39] demonstrated that orthogonality can be restored by multiplying each $P_n^m(x_i)$ by a unique weight associated with each x_i. Sneuew found that this significantly improved the condition number of the system and allowed for a much larger truncation order than was previously possible.

In addition to the loss of orthogonality between the Legendre functions, it was found that conditioning can be substantially affected by the shape of the droplet. This is a result of the evaluation of interior and exterior fields at the interfaces $\partial\Omega_{13}$ and $\partial\Omega_{23}$, characterized by a varying distance from the origin. Since the highest order terms in the expansions for the inner fields scale with r^N and those for the exterior

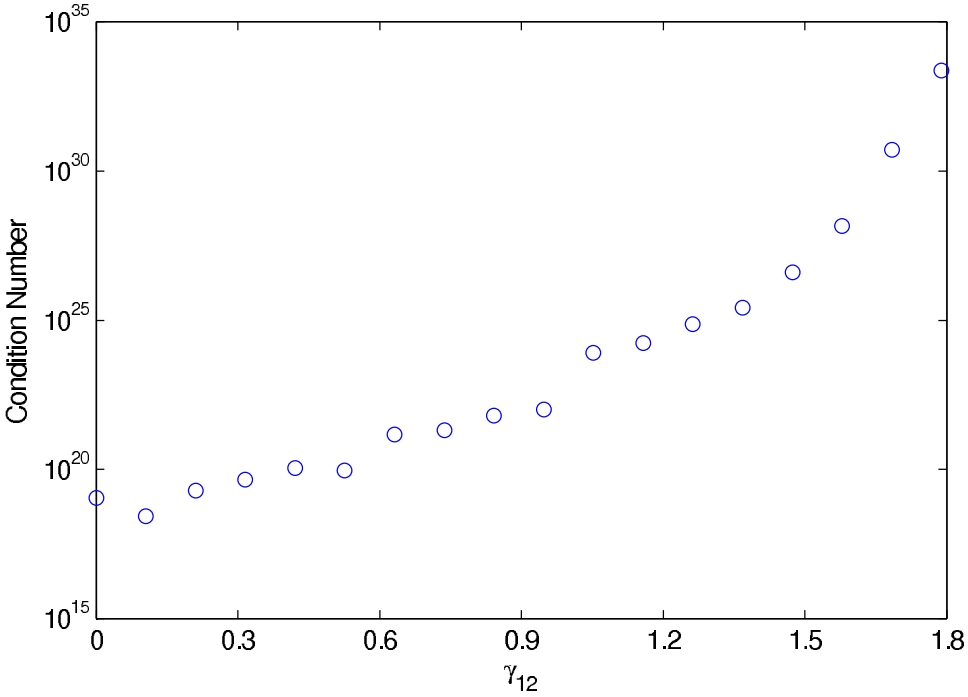

Figure 28: The condition number for increasingly slender droplet shapes (a sphere corresponds to $\gamma_{12} = 0$ and a slender film for $\gamma_{12} \to 2$). The truncation order is $N = 50$ and $M = 675$.

fields scale with r^{-N}, the entries of the coefficient matrix vary by $\mathcal{O}\left((r_{\max}/r_{\min})^N\right)$. As Fig. 28 illustrates, the condition number quickly increases for large aspect ratio droplets (i. e. long and slender droplets).

In an attempt to correct for the lost orthogonality of the Legendre functions and poor scaling in r, preconditioning of the coefficient matrix and a rescaling of the unknowns was tested. As Fig. 27 illustrates, preconditioning reduces the condition number by many orders of magnitude. However, it was also found that a side effect of preconditioning was a dramatic increase in the residual. This increase was enough that convergence in N is lost as shown in Fig. 26. Preconditioning of the linear system was therefore never implemented. On the other hand, it was found that placing the origin at the center of mass of the droplet always resulted in the lowest possible condition number. Hence, this choice was used in all the calculations reported in this chapter.

The major difference between the implementation of the boundary collocation method presented here and the one developed by Ganatos *et al.* [8] is the total number of collocation rings M used when finding a solution. In Ref. [8], M was chosen so that the resultant system of equations would be square. Recall that the collocation rings correspond to discrete values of θ. Any function comprised of powers of $\cos\theta$, such as a spherical harmonic expansion, will possess multiple values of θ that result in identical function values. To ensure a square system, Ganatos *et al.* invested considerable effort in determining which values of θ would result in a degenerate system and consequently should be avoided. For large values of N this task becomes very impractical.

In this research, the difficulties in constructing a square system are sidestepped by generously overdetermining the system of equations. For example, with the values of N and M listed above, there are nearly seven equations for every unknown in the resultant linear system. The tradeoff is that solving such a large system is computationally expensive but still well within the capabilities of a modern desktop computer.

4.6.4 Several Examples

To test the boundary collocation method outlined in this chapter, physical parameters were chosen to duplicate a spherical drop immersed in an infinite layer of fluid under the influence of a linear temperature gradient by setting $\gamma_{12} = \tau_{12} = 0$ and $\alpha_1 = \beta_1 = \gamma_{13} = \tau_{13} = 1$. This problem has a well known analytical solution for the interior flow field known as Hill's spherical vortex [42]. The computed numerical solutions for the temperature and velocity fields for different values of the two remaining dimensionless parameters α_3 and β_3 were found to agree with the analytical solution [2] to within numerical precision. The condition number was found to scale similarly to Fig. 27, however, this did not affect the accuracy or convergence of the numerical solution.

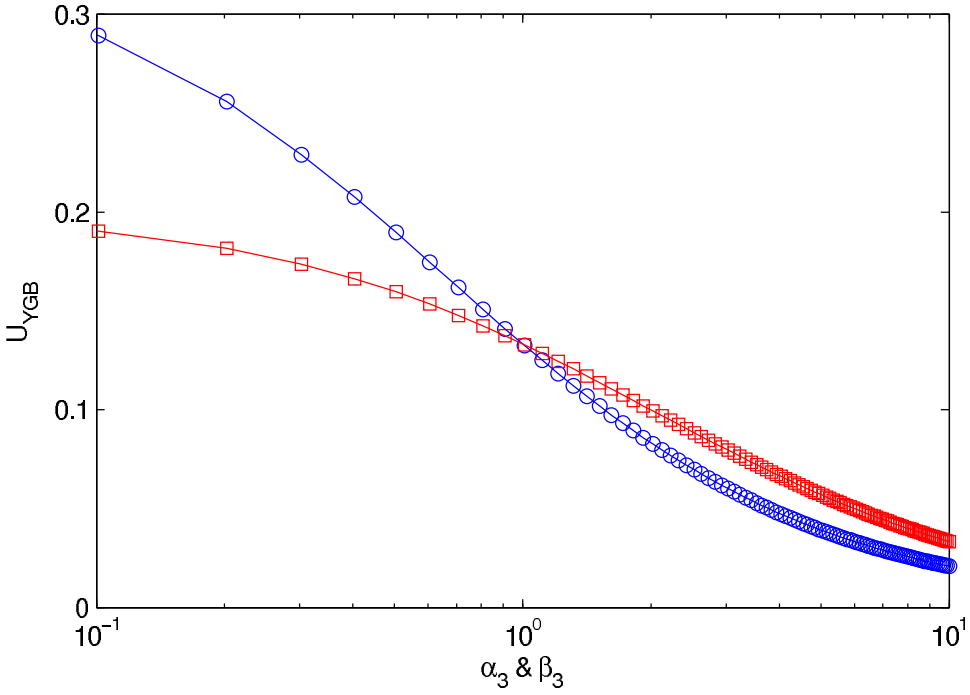

Figure 29: Migration velocity vs. α_3 for $\beta_3 = 1$ (blue circles) and vs. β_3 with $\alpha_3 = 1$ (red squares). The solid curves correspond to the analytical solution (116).

To illustrate the agreement between the numeric and analytical solutions the thermocapillary migration velocity dependence on α_3 and β_3 is compared. The analytical result for the migration velocity was obtained by Young *et al.* [50] which, in the dimensional units of this chapter, is

$$U_{\mathrm{YGB}} = -\frac{2r_0 k_2 \sigma'_{23} \Theta}{(2\mu_2 + 3\mu_3)(2k_2 + k_3)}. \tag{115}$$

Nondimensionalization, simplifies the result to

$$u_s = \frac{U_{\mathrm{YGB}}}{v_0} = \frac{2}{(2 + 3\alpha_3)(2 + \beta_3)}. \tag{116}$$

The comparison between the numerical and analytical migration velocities are shown in Fig. 29. As with the solutions for the fields, exact (within numerical precision) agreement between the numerical solution and the analytical solution is found for varied values of α_3 and β_3.

4.7 A Solution for the Droplet Shape

One of the important new features of an interfacial drop compared with droplets submerged in an infinite layer of fluid is that the shape of the former is not, in general, spherical. Some representative examples are shown in Fig. 30. As the force balance conditions (101) and (102) show, the interfacial droplet can be spherical only in the limit of vanishing non-dimensional surface tension γ_{12} at the substrate surface. As γ_{12} increases from zero, the width-to-height aspect ratio of the droplet becomes progressively larger as it is pulled apart by the surface tension at $\partial\Omega_{12}$ (e. g. Fig. 30b). There is no steady-state solution for the droplet shape for $\gamma_{12} > 1 + \gamma_{13}$; the droplet becomes thinner and thinner as the time progresses. In this limit, ignoring surface tension gradients, the solution is well described by the lubrication approximation [7].

The non-dimensional surface tension γ_{13} at the upper surface of the droplet controls the degree of submersion of the droplet. Interfacial droplets in steady-state will exist for $1 - \gamma_{12} < \gamma_{13} < 1 + \gamma_{12}$, with $\gamma_{13} = 1$ corresponding to the droplet being symmetric with respect to the substrate surface (see Fig. 30b). Decreasing γ_{13} below unity forces the droplet to be expelled from the substrate fluid (see Fig. 30c), while increasing γ_{13} above unity increases the submersion of the droplet into the substrate fluid with $\gamma_{13} \approx 1 + \gamma_{12}$ corresponding to essentially complete encapsulation (see Fig. 30d). The effect of droplet geometry on migration velocities and flow profiles will be discussed in the following sections.

4.8 A Solutions for the Temperature Field

Although the temperature field is not of direct interest, it is important for describing the relative magnitudes of thermocapillary stresses at the surfaces of the droplet and the substrate. Qualitatively, the structure of the temperature field is controlled by the dimensionless thermal conductivities β_1 and β_3.

In particular, the thermal conductivity ratio $\beta_1 = k_1/k_2$ controls the relative

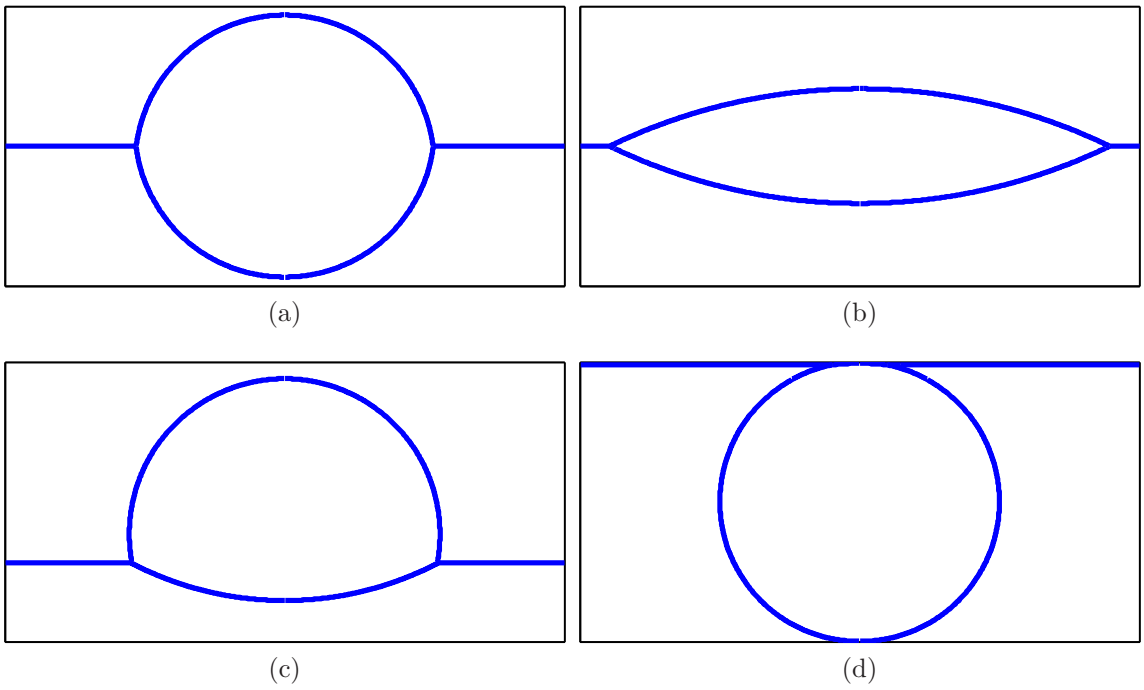

Figure 30: A $y = 0$ cross section of interfacial droplet shapes. (a) $\gamma_{12} = 0.25$ and $\gamma_{13} = 1$, (b) $\gamma_{12} = 1.8$ and $\gamma_{13} = 1$, (c) $\gamma_{12} = 0.80$ and $\gamma_{13} = 0.47$ and (d) $\gamma_{12} = 1$ and $\gamma_{13} = 2$.

magnitude of the thermocapillary stresses at the droplet's top and bottom surface. As Figs. 31a and 31b illustrate, for $\beta_1 < 1$ the temperature gradient at the top surface of the droplet is smaller, while for $\beta_1 > 1$ it is larger, than at the bottom surface. Correspondingly, the thermocapillary stresses at the top dominate for $\beta_1 > 1$ and those at the bottom dominate for $\beta_1 < 1$. It is worth mentioning that the thermocapillary stresses at both the top and bottom surface increase with increasing β_1.

The second ratio $\beta_3 = k_3/k_2$ controls the importance of the thermocapillary stresses at the droplet surface relative to those at the substrate surface. Figs. 31c and 31d show that for $\beta_3 < 1$ the thermal gradient on the droplet surface increases above its value far from the droplet, while for $\beta_3 > 1$ the thermal gradient on the droplet surface decreases below that value. In particular, for $\beta_3 \to \infty$ the temperature becomes constant throughout the droplet and thermocapillary stresses on the

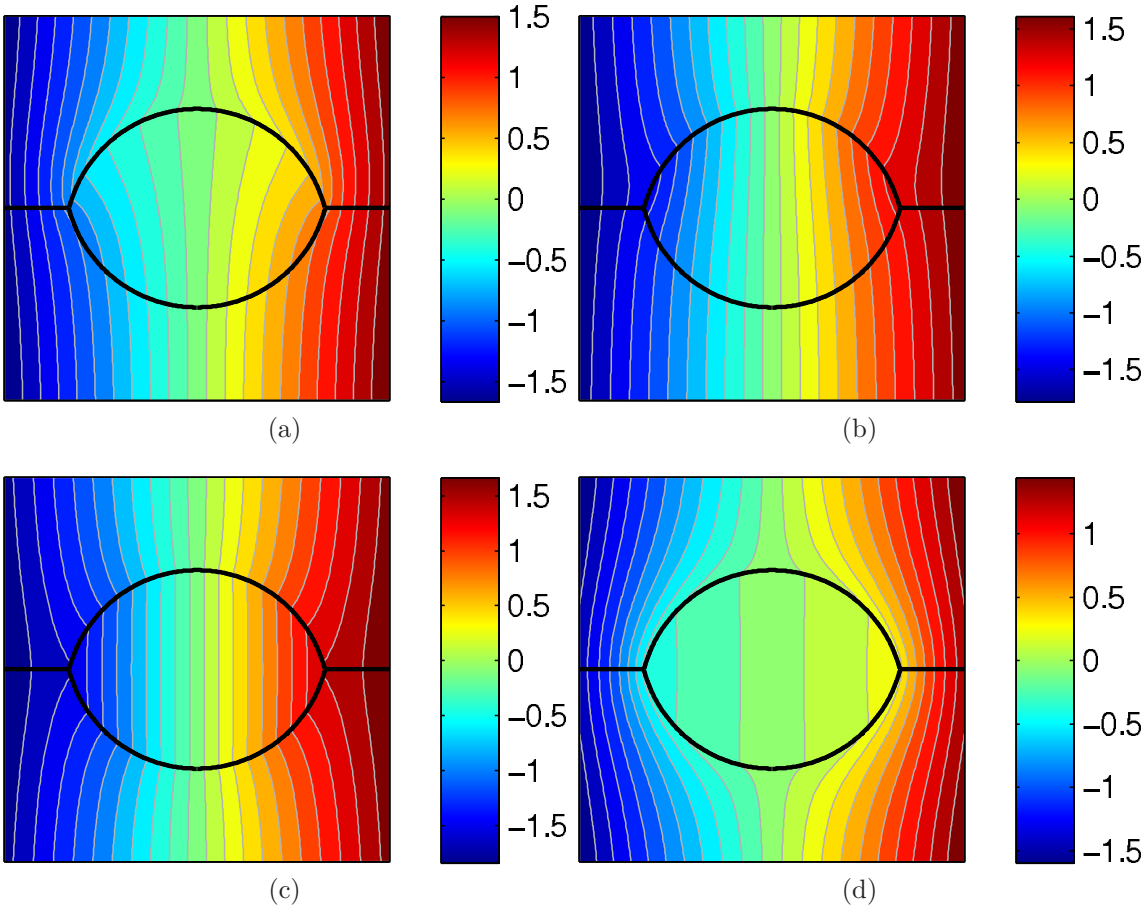

Figure 31: Temperature field in the $y = 0$ plane. (a) $\beta_1 = 0.09$, (b) $\beta_1 = 10$, (c) $\beta_3 = 0.09$ and (d) $\beta_3 = 10$. The contour levels are scaled with the maximum value corresponding to red (hot) and the minimum value corresponding to blue (cold).

droplet surface vanishes. In the case of the submerged droplet model this resulted in a vanishing thermocapillary migration velocity (116).

As illustrated in Fig. 31, the temperature field for an interfacial droplet looks very similar to the submerged droplet model of Chapter 3. For the submerged droplet the scaled submersion depth δ controlled the asymmetry (top to bottom) in the interior temperature field. In the case of an interfacial droplet, β_1 does much the same only with a slightly stronger effect. The remaining parameters that determine the temperature field are those which define the droplet shape and position. These have no analog in the submerged droplet model. However, it was found that varying these parameters always resulted in a temperature field that resembled one of the four types shown in Fig. 31.

4.9 Solutions for the Velocity Field

4.9.1 The Thermocapillary Migration Velocity

Having described the shape of the droplet and the temperature field that drives the flow, attention is now focused on the computation of the thermocapillary migration velocity for interfacial droplets. In the classical problem of thermocapillary migration of a droplet far from any interfaces (solid or fluid) the order of magnitude of the migration velocity (115) is essentially determined by: the droplet size r_0, the dropl [50]. For interfacial droplets the dominant contribution to the thermocapillary migration speed U_0 is given by the velocity (91) of the substrate's free surface relative to a solid boundary (e. g. the bottom of the container).

This phenomenon is very similar to the advection of a submerged droplet described in Chapter 3. In both cases, the speed of advection is essentially determined by the substrate thickness $H \gg r_0$. The physical properties of a droplet will have a rather small impact on its absolute speed and are mostly important in describing the relative motion of multiple droplets. In the analysis of the submerged droplet model the

mobility function (71) was used to judge the effect of the air-substrate interface on the migration velocity. A similarly defined mobility function is therefore well suited to characterize the small impact of the physical properties of an interfacial droplet on the migration velocity. This mobility function is defined as

$$M_i = \frac{U_0/v_0}{u_0}, \tag{117}$$

where u_0 is given by

$$u_0 = \frac{2}{(2+3\alpha_3)(2+\beta_3)} - \tau_{12}\frac{\chi}{4}. \tag{118}$$

The quantity u_0 is simply the superposition of two migration velocities. The first is the speed of a spherical droplet in an unbounded substrate undergoing thermocapillary migration (i. e., U_{YGB}). This speed is small and towards area of warmer fluid (in the $\hat{\mathbf{x}}$ direction). The second is the speed of a droplet that is being advected with the substrate (i. e., V_1^{∞}). This speed is large and towards regions of cooler fluid (in the $-\hat{\mathbf{x}}$ direction). Due to the requirement that $\chi \gg 1$, u_0 will almost always be negative.

Deviations of M_i from unity will directly correlate to the effect of migrating confined at the interface between the covering fluid and the substrate (i. e. $\partial\Omega_{12}$) as compared to migrating in an unbounded substrate. That is for values of $M_i < 1$ the effect of the $\partial\Omega_{12}$ is to retard the migration velocity and for values of $M_i > 1$ the effect is to enhance the velocity. As a reference, the mobility function of the submerged drop model has also been computed and given throughout this discussion.

The parameter space describing the migration velocity of an interfacial droplet has too many nondimensional parameters to explore comprehensively. Instead the focus here has been restricted to the dependence of the mobility function M_i on each of the eight parameters, with the other seven held fixed. All fixed parameters were set to unity except γ_{12}, the nondimensional surface tension at the interface $\partial\Omega_{12}$. A value of $\gamma_{12} = 0.5$ was chosen to yield an interfacial droplet with moderate (compared to a perfect sphere) deformation. Choosing a value of $\gamma_{12} = 0$ would violate the

assumption of small capillary number, since the latter scales inversely with surface tension.

Analysis begins by first examining how M_i varies with the bulk properties of the fluids, the viscosity and thermal conductivity ratios. As Fig. 32a illustrates, an increase in the viscosity ratio $\alpha_1 = \mu_1/\mu_2$ results in an increase in M_i. The speed of a droplet undergoing thermocapillary migration in an unbounded substrate is determined by Eq. (115). An interfacial droplet however is bounded by a substrate and a covering fluid, ans so its thermocapillary migration velocity should have two similar contributions from each of these substrates

$$\frac{U_0 - V_1^\infty}{v_0} \sim \frac{2}{(2+3\alpha_3)(2+\beta_3)} + \frac{\tau_{13}}{(2\alpha_1+3\alpha_3)(2+\beta_3/\beta_1)} \times C_1, \qquad (119)$$

where C_1 is an unknown and all other corrections to the migration velocity have been omitted for clarity. Since the mobility function was only scaled with the first half of these terms, it too will contain a term proportional to C_1

$$M_i \sim 1 + \frac{\tau_{13}}{(2\alpha_1+3\alpha_3)(2+\beta_3/\beta_1)} \left(\frac{4(2+3\alpha_3)(2+\beta_3)}{8 - \tau_{12}\chi(2+3\alpha_3)(2+\beta_3)} \right) \times C_1, \qquad (120)$$

where again all corrections to the mobility function from other contributions have been omitted for clarity.

Holding all parameters fixed except α_1, the trend observed in Fig. 32a is now quite easily understood as the scaled thermocapillary contribution from the top of the droplet. When $\alpha_1 \ll 1$ the thermocapillary migration velocity increases and the interfacial droplet moves more rapidly towards regions of warmer fluid (M_i is reduced). For large values of α_1, the thermocapillary migration velocity is reduced and the interfacial droplet moves more rapidly towards regions of cooler fluid (M_i is increased). A slight decrease in M_i around $\alpha_1 = 0.2$ is likely due to a rearrangement of the flow in the covering fluid.

Using the same arguments concerning the scaling of the thermocapillary migration velocity with respect to the covering fluid, one would expect the dependence of M_i

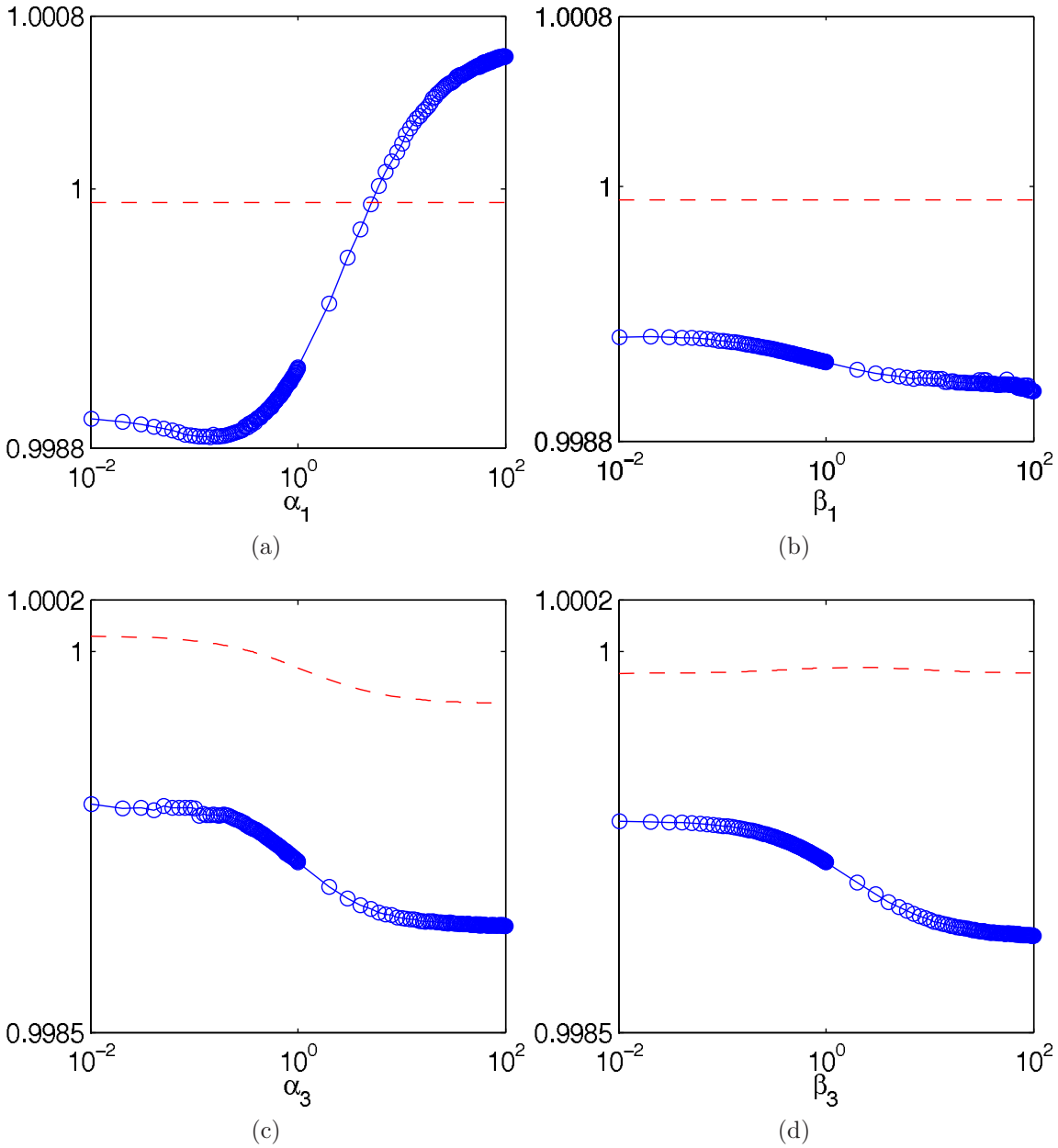

Figure 32: The mobility function dependence on the bulk material parameters. The symbols show the numerical results for the partially submerged droplet (blue), while the dashed curve represents the fully submerged droplet (red).

on the thermal conductivity ratio $\beta_1 = k_1/k_2$ to have the opposite effect as α_1. While this trend is observed, the decrease in the mobility function, as shown in Fig. 32b, is much less pronounced than expected. This counterintuitive behavior is correctly explained by examining the other forces acting on the drop.

The sum of the line force from the contact line (112) and the shear force from the asymptotic substrate flow (113) play a game of tug-of-war on the droplet. When all of the thermal conductivities are equal these forces exactly balance as seen in Fig. 33. When the thermal conductivities are not equal one of these forces will dominate. As illustrated in Fig. 33a for small values of β_1 the net force points in the $\hat{\mathbf{x}}$ direction and for large values in the $-\hat{\mathbf{x}}$ direction. While this imbalance of force is ultimately compensated for by the hydrodynamic drag on the droplet, its end effect is a change in the migration velocity. For small value of β_1 this results in an increase in the migration velocity towards warmer fluid. For large values of β_1 this results in an increase towards regions of cooler fluid. Consequently these changes tend to cancel the expected trend found from the analysis of the thermocapillary contributions.

The dependence of M_i on $\beta_3 = k_3/k_2$ (see Fig. 32d) can also be understood by reexamining the balance of line and shear forces on the droplet. As seen in Fig. 33b, for small values of β_3 the droplet is pulled towards cooler fluid while for large values the droplet is pulled toward regions of warmer fluid. The mobility function mirrors this dependence nicely, monotonically decreasing for larger values of the β_3.

From Fig. 32c it is observed that the mobility function also decreases monotonically for increasing values of α_3. This trend is more difficult to explain as both the line and shear forces are in balance and both substrates contribute equally to the thermocapillary migration of the droplet. This effect then must be attributed to the interface $\partial\Omega_{12}$ (the interface between the covering fluid and the substrate). The presence of $\partial\Omega_{12}$ requires the normal component of the velocity in fluids 1 and 2 to vanish at $\partial\Omega_{12}$. Such a reduction in the velocity field near $\partial\Omega_{12}$ results in an effective

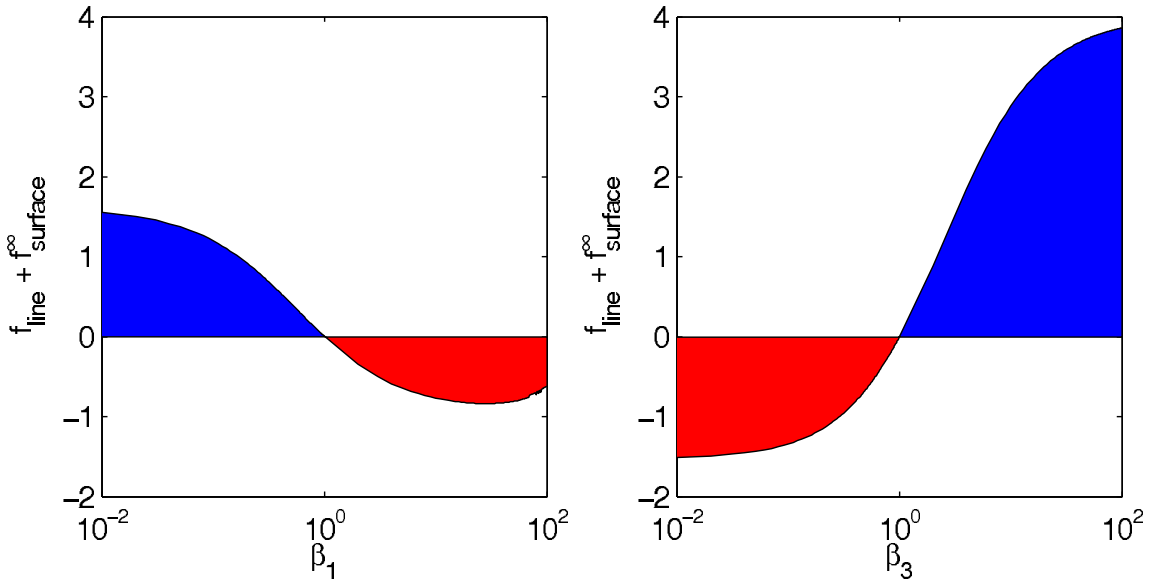

(a) (b)

Figure 33: The combined contact line and shear flow force. When β_i is not equal to one these two forces do not cancel. The resultant force will either point in the positive (blue) or negative (red) $\hat{\mathbf{x}}$ direction.

hydrodynamic drag on the droplet.

To understand the role of the droplet viscosity in determining the trend in the drag force, consider an idealized spherical droplet whose center of mass is located at the interface $\partial\Omega_{12}$. With the exception of the droplet viscosity, all physical properties of the fluids and interfaces are assumed equal. In a constant temperature gradient and imposed shear flow the leading order velocity field outside of the droplet will be the superposition of the fields given in Eqs. (70 and 79); the fields for a droplet in an unbounded substrate. At the planar interface $\partial\Omega_{12}$ the normal component of Eq. (70) vanishes. The normal component of Eq. (79) however, does not vanish but instead is found to be

$$\mathbf{V}_{\text{out}}^{\text{shear}} \cdot \hat{\mathbf{z}} = \frac{\tau_{12}}{2r^4}\left(\frac{\alpha_3}{\alpha_3+1}\right). \tag{121}$$

It is impossible to determine the analytical form of the corrections to the flow field required to correctly satisfy the boundary conditions at $\partial\Omega_{12}$. To properly cancel the non-zero part of the flow at the planar interface it must be proportional to the right

ahnd side of Eq. (121). The drag force associated with this correction will also be proportional to Eq. (121) and, since the droplet is migrating towards cooler fluid, it must point towards regions of warmer fluid. From this argument it is possible to determine the effect on the mobility function

$$M_i \sim 1 + \tau_{12}\frac{\alpha_3}{(1+\alpha_3)}\left(\frac{4(2+3\alpha_3)(2+\beta_3)}{8-\tau_{12}\chi(2+3\alpha_3)(2+\beta_3)}\right) \times C_2, \tag{122}$$

where the large term on the right is the scaling u_0 (118) and C_2 is a proportionality constant. The other corrections to the M_i have been omitted for clarity of discussion.

The reduction in the mobility function for increasing droplet viscosity can now be understood as corresponding to an increase in the hydrodynamic drag on the droplet. This drag results from the effects of the planar interface $\partial\Omega_{12}$ on the exterior flow and its proportionality was determined by Eq. (121). As Fig. 32c clearly illustrates, this is exactly the trend predicted by Eq. (122) and observed numerically.

Having discussed the effect of the bulk material parameters on the mobility function only the effect of the interfacial material parameters remain. Fig. 34a shows that an increase in the surface tension ratio $\gamma_{12} = \bar{\sigma}_{12}/\bar{\sigma}_{23}$ leads to a nearly linear increase in M_i. This is due to an decrease in the viscous drag and is nicely illustrated by comparing the velocity field near an interfacial droplet that is nearly spherical Fig. 35a with an interfacial droplet that is very slender Fig. 35b. As the droplet becomes more slender (increasing γ_{12}) it will displace less of its neighboring fluid and hence experience less drag.

For small values of $\gamma_{13} = \bar{\sigma}_{13}/\bar{\sigma}_{23}$ an interfacial droplet will sit mostly above the planar interface (exposed) while for large values it is nearly submerged within the substrate. The exposed droplet migrates almost entirely in a constant streaming flow experiencing little drag. Corrections to this flow from the interfaces require very little rearrangement of the asymptotic flow as observed in Fig. 36a. In contrast, the submerged interfacial droplet is migrating almost entirely within a shear flow. Fig. 36b demonstrates that a considerable reorganization of the flow was required

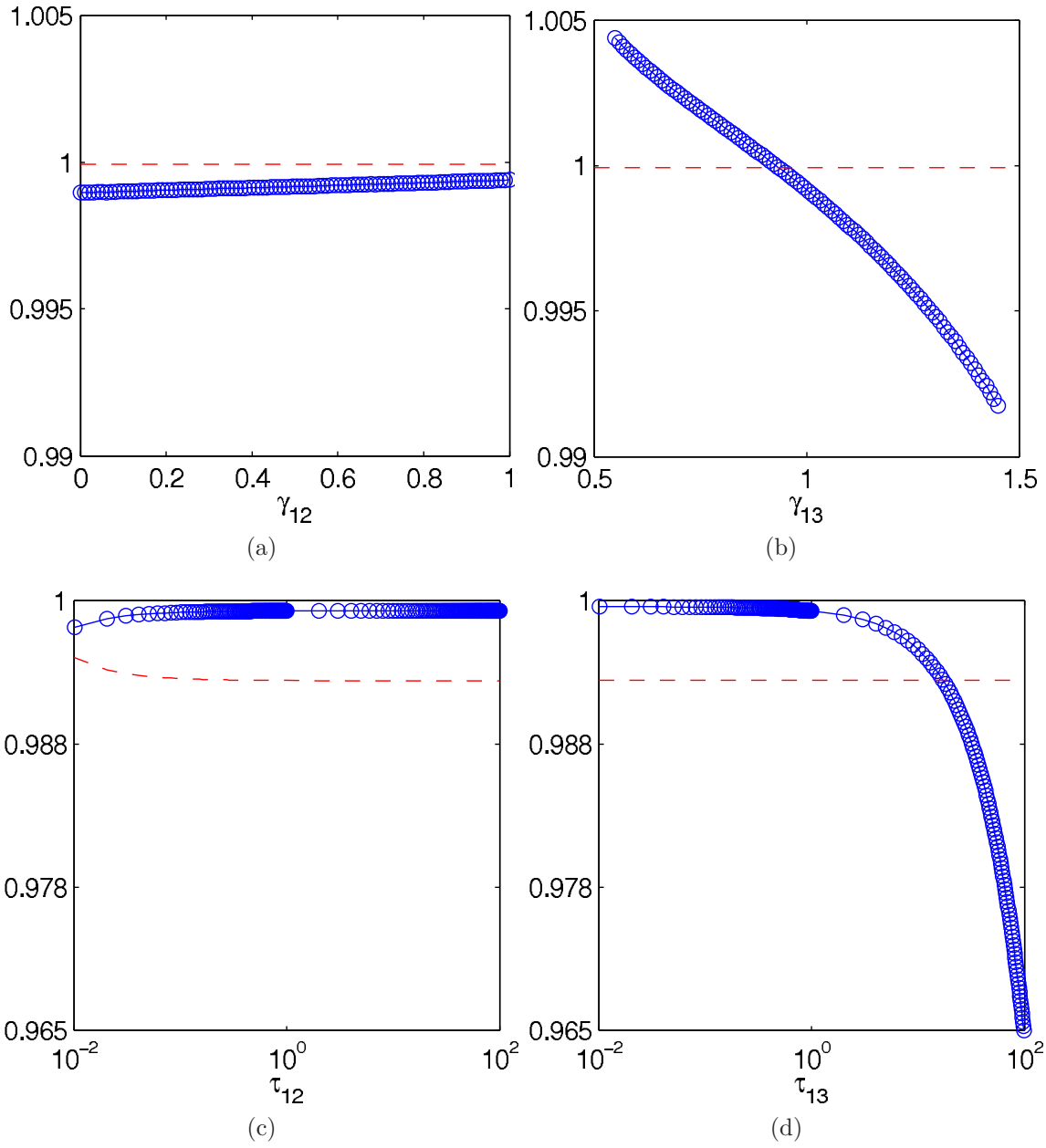

Figure 34: The mobility function dependence on the bulk material parameters. The symbols show the numerical results for the interfacial droplet (blue), while the dashed curve represents the submerged droplet (red).

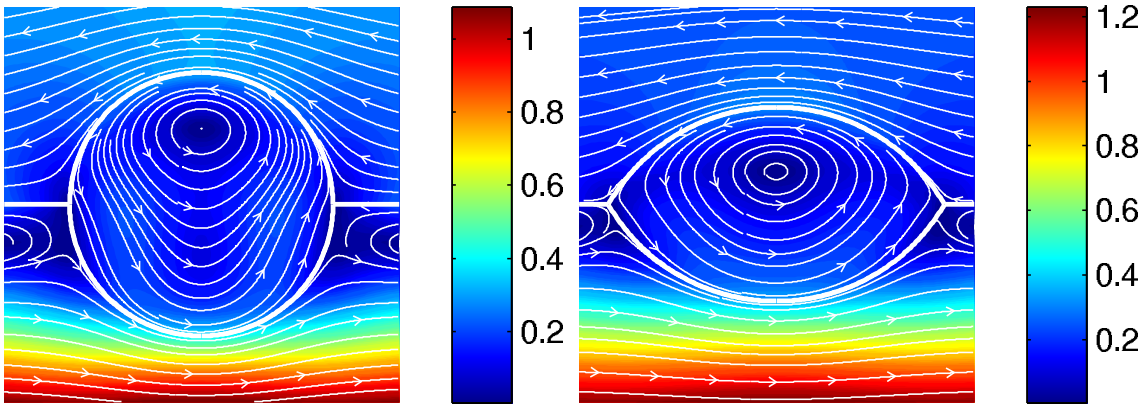

(a) (b)

Figure 35: Streamlines in the $y = 0$ symmetry plane of a spherical and slender interfacial droplet. The slender droplet displaces less neighboring fluid and thus experiences less drag. Panel (a) is for value of $\gamma_{12} = 0$ and panel (b) is for a value of $\gamma_{12} = 1$. All remaining parameters are fixed at unity.

to satisfy boundary conditions for the submerged interfacial droplet. This had the effect of reducing the mobility function M_i, whose dependence on γ_{13} was observed in Fig. 34a.

The remaining two interfacial parameters, τ_{12} and τ_{13}, are the ratios of the temperature coefficients of surface tension between the interfaces. They determine the relative strengths of the thermocapillary flows originating from each interface. The dependence of the mobility function M_i on these two parameters has already been determined in Eqs. (120) and (122) while discussing the effects of β_1 and α_3. As illustrated in Figs. 34c and 34d the numerical results are in agreement with these predictions.

Before concluding this section on droplet migration velocities there remains one interesting behavior that has yet to be discussed. One of the novel properties of droplets undergoing thermocapillary migration is their ability to arrest buoyancy induced migration. Young *et al.* [50] observed that by aligning the imposed temperature gradient in the opposite direction of gravity air bubbles could be suspended in silicon oil indefinitely. The bubbles did not migrate up or down, while the fluid surrounding

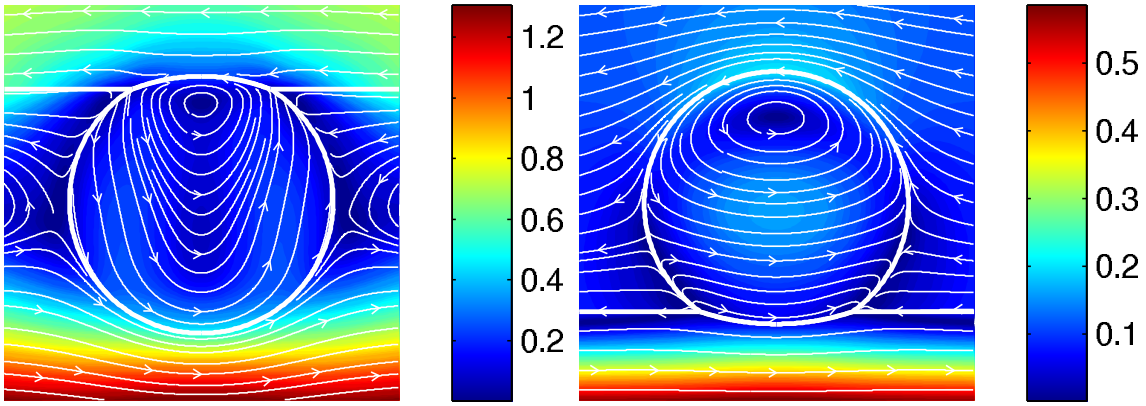

(a) (b)

Figure 36: Streamlines in the $y = 0$ symmetry plane of a exposed and submerged interfacial droplet. The exposed droplet disrupts less neighboring fluid and thus experiences less drag than the submerged interfacial droplet. Panel (a) is for a value of $\gamma_{13} = 0.5$ and panel (b) is for a value of $\gamma_{13} = 1.5$. All remaining parameters are fixed at unity.

them stayed in constant motion. While this research is only concerned with temperature gradients aligned perpendicular to gravity it is still possible to arrest the migration of a droplet.

For very small values of τ_{12} the asymptotic flow in the substrate will be weak (see for example Eq. (91)) and the speed of advection towards cooler fluid is reduced. The thermocapillary effect at the surface of the droplet remains unchanged and continues to nudge the droplet towards warmer fluid. Keeping all other parameters fixed, there will be a specific value of τ_{12} which exactly balances these competing effects. This results in an interfacial droplet with zero migration velocity. The dependence of the mobility function for small values of τ_{12} is shown in Fig. 37 for both an interfacial droplet and the submerged drop model.

The submerged droplet model of Chapter 3 predicts that the planar interface $\partial\Omega_{12}$ will cause the droplet to approach standstill more slowly than a drop in an unbounded substrate. Interestingly, the numerical results for an interfacial droplet predict that the droplet will approach standstill more quickly than the unbounded drop. This is precisely what was predicted from the mobility function analysis (e. g. Eq. (122)).

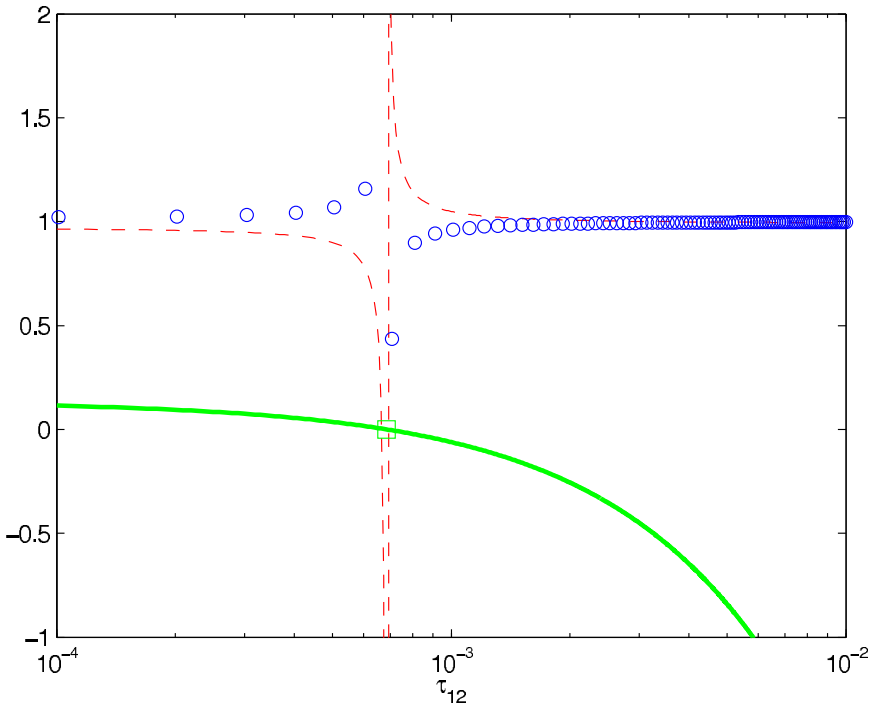

Figure 37: The mobility function of an interfacial droplet (blue circles) for very small values of τ_{12}. For comparison the mobility function of the submerged droplet model (red dashes) and the migration velocity of an unbounded droplet (green line) are given. The green square is the exact value of τ_{12} resulting in $U_0 = 0$ for an unbounded droplet in a similar asymptotic flow.

An explanation of the behavior predicted by the submerged droplet model remains elusive.

4.9.2 The Interior Flow Field

Having thoroughly examined the dependence of the migration velocity on the physical parameters of the system, an analysis of the flow field inside the interfacial droplet is all that remains to complete this chapter. The mixing properties of this flow field are largely determined by its topological structure. This topological structure is characterize by identifying the invariant sets of the flow: separatrix surfaces, homo/heteroclinic orbits and fixed points (stagnation points). One question of particular interest is the effect the droplet shape and contact line will have on the topological structure of the flow.

An interfacial droplet system possesses several symmetries resulting from the shape of the droplet and the asymptotic fields. These symmetries determine the location of the invariants of the flow. For example, the flow is mirror symmetric with respect to the $y = 0$ plane, which is thus both an invariant plane and a separatrix of the flow, with $V_y = 0$ at $y = 0$. The flow is also invariant with respect to reflection about the $x = 0$ plane. Combined with the time reversal ($\mathbf{v} \rightarrow -\mathbf{v}$) this requires $v_y = v_z = 0$ at $x = 0$. These symmetries, together with the incompressibility condition (82), guarantee the existence of a curve of fixed points lying in the plane $x = 0$. Therefore, examination of the velocity field in the planes $x = 0$ and $y = 0$ will uncover most, if not all, invariant structures.

The first parameter that is considered is τ_{12}, the scaled temperature coefficient of surface tension at the planar interface $\partial\Omega_{12}$. This parameter controls the strength of the shear flow induced from the planar interface relative to the thermocapillary flow generated by the droplet surface. For values of $\tau_{12} \sim 1$, the shear flow will dominate. The streamlines for this flow (in the $y = 0$ plane) were already computed in Fig. 35a for $\alpha_3 = 1$. It was observed that the fluid within the droplet rotates counterclockwise in that plane around elliptic fixed points located above the center of the drop. For small values of τ_{12} the asymptotic shear flow is negligible and the flow field inside the droplet is the same counter-rotating thermocapillary flow examined in Section 4.6.4. The streamlines and level sets of this flow were given in Fig. 12. For that flow, it was found that a line of elliptic fixed points centered on the droplet extended $x = 0$ plane. This line of fixed points organized the flow in the interior of the droplet.

As τ_{12} is increased from very small values, the changes in the flow field can be characterized by calculating the position of the fixed points on the surface of the interfacial droplet. The velocity field of a spherical droplet in an unbounded substrate with the same asymptotic fields as the interfacial droplet is the superposition of the flows given by Eqs. (70 and 79). This flow possesses a set of (saddle) fixed points

lying at the intersection of the $y = 0$ plane with the droplet surface given by

$$\frac{\tau_{13}(2\cos^2\theta + \alpha_3)}{2(\alpha_3 + 1)} + \frac{3\cos\theta}{(3\alpha_3 + 2)(2 + \beta_3)} = 0. \tag{123}$$

Likewise another set of (elliptic) fixed points lies at the intersection of the droplet surface with the $x = 0$ plane given by

$$\frac{\tau_{13}(\alpha_3 + 2)\cos\theta}{2(\alpha_3 + 1)} + \frac{3}{(3\alpha_3 + 2)(2 + \beta_3)} = 0. \tag{124}$$

The locations of these fixed points is compared to the calculated fixed points on the surface of an interfacial droplet for different values of τ_{12}, holding the other parameters fixed. The location of the fixed points on the surface of the submerged droplet model of Chapter 3 have also been computed for comparison.

To calculate the locations of the fixed points for the interfacial drop, the values of relative surface tensions $\gamma_{12} = 1$, $\gamma_{13} = 1.888$ and temperature coefficient $\tau_{13} = 1$ where chosen. These values correspond to a droplet that is almost completely submerged. The viscosity and thermal conductivity ratios were also set to $\alpha_3 = \beta_3 = 1$ and $\alpha_1 = \beta_3 = 10^{-6}$. This choice of parameters reflect the fact that in practice an interfacial droplet is mostly submerged and the covering fluid (e. g. air or even vacuum) would likely have viscosity and thermal conductivity negligible compared to those of the droplet and substrate. Furthermore, this choice of parameters facilitates the comparison between the analytical submerged droplet model and interfacial droplet solution.

The locations of the fixed points on the surface of the drop are given in Fig. 38 for various values τ_{12}. For the interfacial drop and submerged droplet model, the fixed points are found numerically using a bounded Newton's method. The fixed points for the droplet in an unbounded substrate were obtained by solving Eqs. (123) and (124). Good qualitative agreement between all three flows is observed.

For a value of $y = 0$, the droplet in an unbounded substrate experiences a bifurcation in the number of fixed points at the value $\tau_{12} = 4/15$ as seen in Fig. 38a. This is

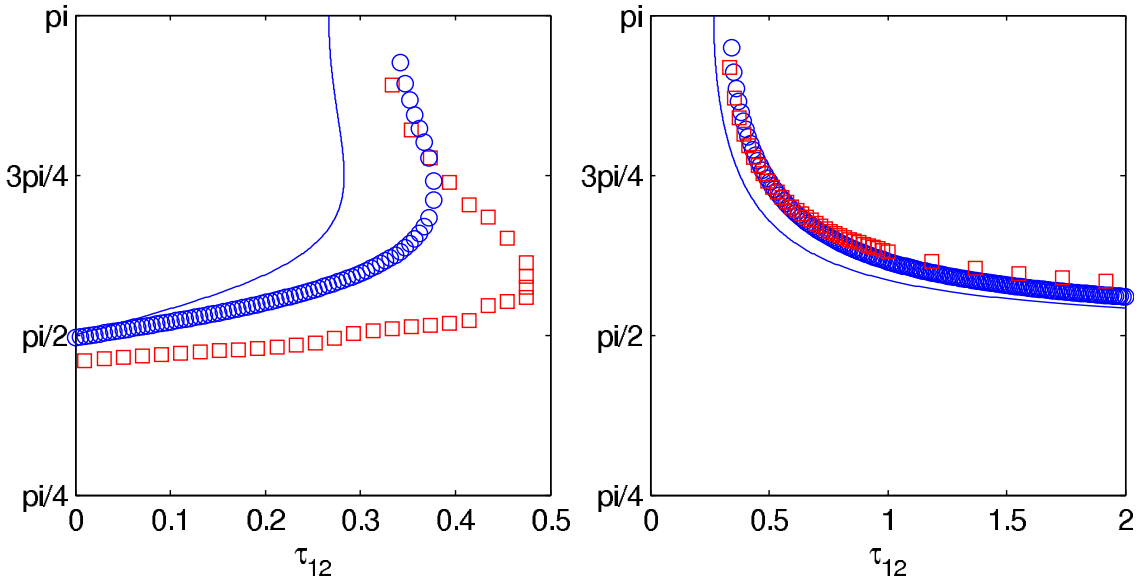

(a) (b)

Figure 38: The zenith angle of fixed points on the surface of a droplet in an unbounded fluid (blue line), a droplet submerged $\delta = 1.25$ from the air-substrate interface (blue circles) and an interfacial droplet (red squares) Panel (a) corresponds to fixed points with $y = 0$ and panel (b) to fixed points with $x = 0$.

due to one of the elliptic fixed points in the interior of the drop crossing the bottom surface of the droplet (at $\theta = \pi$). Thereafter, no fixed points are found to exist on the surface of the drop for $y = 0$. For $x = 0$ however, the intersection of the elliptic fixed point with the bottom surface of the drop creates two fixed points (one on each side of the drop surface). These fixed points approach the zenith angle ($\theta = \pi/2$) as $\tau_{12} \to \infty$, as illustrated in Fig. 38b.

The submerged drop model and the interfacial droplet solution are in good qualitative agreement. One subtle difference is that the interfacial droplet has a range of τ_{12} twice as large for which two fixed points exist simultaneously on either side of the drop. The streamlines and level sets of the velocity field are given in Fig. 39 for the value of $\tau_{12} = 0.35$. This flow field is very similar to the one observed in Chapter 3 for the submerged flow model. The streamlines exterior to the interfacial droplet indicate the presence of a strong turning flow that was not present in the submerged flow model. This likely accounts for the exaggerated size in the range of τ_{12}. The

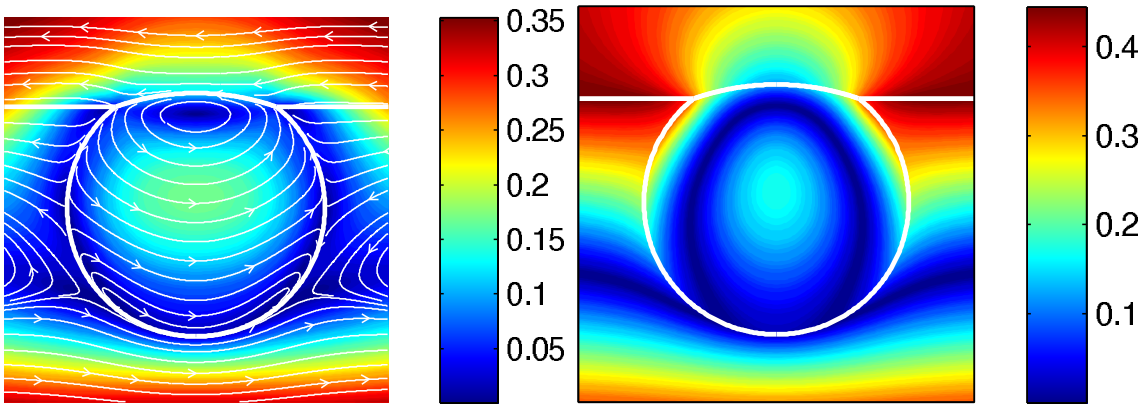

(a) (b)

Figure 39: The streamlines for $y = 0$ (a) and level sets for $x = 0$ (b) for the velocity field of an interfacial droplet. The value of τ_{12} was chosen to illustrate the two hyperbolic fixed points on the surface of the drop.

persistence of the turning flow delays the inevitable collision of the fixed points.

During the analysis of the submerged droplet model, it was found that for values of $\alpha_3 \ll 1$, the flow inside the droplet would contain a pair of spiral fixed points. These fixed points were connected by a rather curious heteroclinic obit not contained to the $y = 0$ plane. In light of the general similarity thus far observed between the submerged droplet model and the interfacial droplet solution, a comparison of the flows for small α_3 are expected to produce similar results. To test this hypothesis the number and location of fixed points on the surface of the droplet for both systems has been determined for comparison.

For $\alpha_3 = 0.01$, the locations of the fixed points on the surface of the drop are given in Fig. 40 for various values of τ_{12}. The Eqs. (123 and 124) for the droplet in an unbounded substrate are very similar to the $\alpha_3 = 1$ case considered previously. The range of τ_{12} values that allowed a pair of fixed points was much larger. This is mostly likely to accommodate the spiral fixed fixed points. The submerged droplet model also exhibits a bifurcation in the number of fixed points at a similar value of τ_{12}. These hyperbolic fixed points persist at all values of τ_{12}, settling on either side of the droplet equator ($\theta = \pi/2$) as $\tau_{12} \to \infty$.

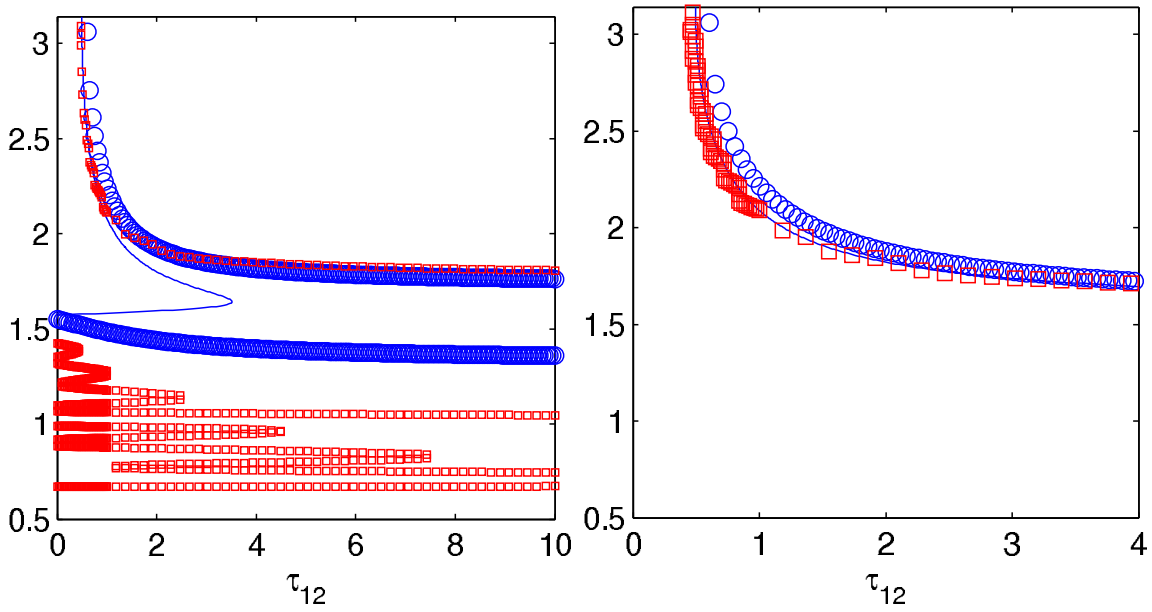

(a) (b)

Figure 40: The zenith angle of fixed points on the surface of a droplet in an unbounded fluid (blue line), a droplet submerged $\delta = 1.25$ from the air-substrate interface (blue circles) and an interfacial droplet (red squares). Panel (a) corresponds to fixed points with $y = 0$, and panel (b) to fixed points with $x = 0$.

The interfacial droplet possess qualitatively different behavior. While the number and location of fixed points for all three flows match up nicely in the $x = 0$ plane, the locations of the fixed points for $y = 0$ do not. As shown in Fig. 40a, the interfacial droplet will contain three complexes of fixed points in the $y = 0$ plane. The first complex is in the southern hemisphere of the droplet. The position of these fixed points on the droplet nicely mirrors the locations found from the submerged droplet model. The remaining two complexes are located on either side of the zenith angle $\theta \approx 1$. As τ_{12} is increased, the number of fixed points in each of these complexes first increases and then steadily decreases. For large τ_{12} two fixed points remain from one cluster and one from the other.

For values of $\tau_{12} \approx 10$ the cluster of two fixed points is found to straddle the zenith angle $\theta = 0.66$. This value corresponds to the exact location of the contact line. When $y = 0$ the condition of steady-state requires the contact line (here just

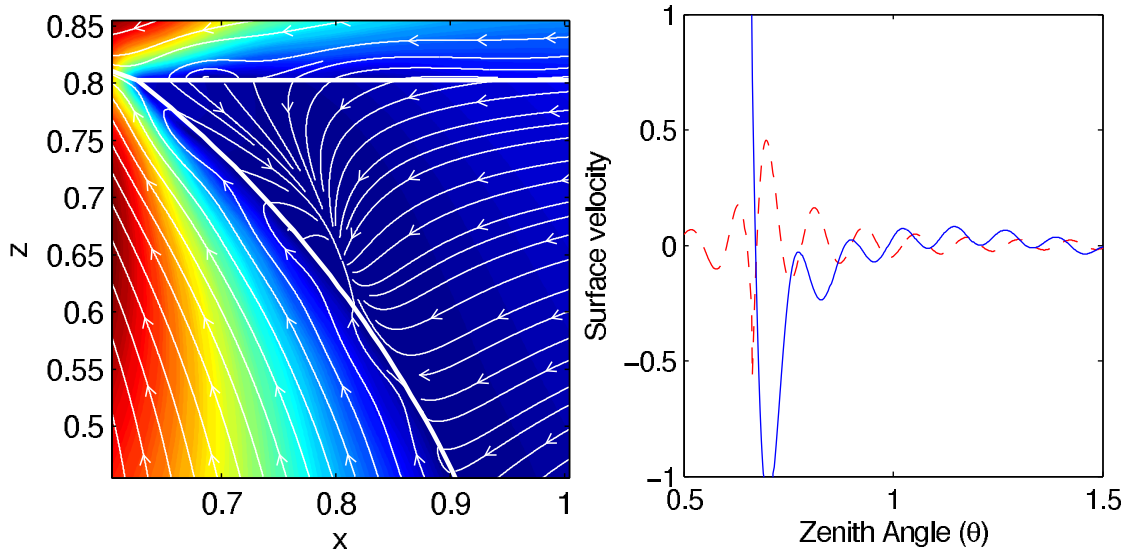

(a) (b)

Figure 41: (a) Streamlines near the contact line of an interfacial droplet. (a) The velocity field at the surface of the drop as a function of the zenith angle (θ) is also provided to demonstrate oscillations in the solution near the contact line. The velocity field is decomposed into components normal to the drop surface (dashed red) and tangential (solid blue).

a point) to be a fixed point of the flow. The numerical solution only approximately satisfies this boundary condition. Usually, the velocity field at the contact point is not found to be identically zero but some small number. This effect is exacerbated for droplet geometries resulting in an acute wedge domain near the contact line.

By using a larger truncation order in the boundary collocation procedure the residual of the solution generally decreased. However, even for high truncation orders the error in the boundary conditions associated with the contact line does not decrease. Instead, an oscillation in the velocity field develops in the neighborhood of the contact line. This oscillation in the flow corresponds to an oscillation in the error near the contact line. This phenomenon is observed in Fig. 41b for the normal component of the velocity vector (shown in red). It is this oscillation in the velocity field which creates the complex of fixed points near the contact. The streamlines of the flow near the contact point are given in Fig. 41a. From this figure it is quite clear that the boundary collocation procedure is not correctly determining the flow in the

neighborhood of the contact point. Because the flow is essentially stagnant here, this does not lead to a significant increase in the residual of the system.

The other cluster of fixed points was located below the equator of the droplet. This far from the contact line, the oscillations in the velocity field have already damped out. These fixed points are the result of a new flow structure not seen in the submerged droplet model. Fig. 42 provides the streamlines near the interior surface of this drop for consecutively larger values of τ_{12}. As Fig. 42a illustrates, an alternating series of saddles and spirals lie near the bottom surface of the droplet. As τ_{12} is increased, the total number of these fixed points decreases until only one spiral fixed point is located near the equator. This single spiral is the same spiral that was found for the submerged droplet model in Chapter 3.

Having thoroughly investigated the effect of τ_{12} and α_3 on the topology of the flow, six parameters remain unexamined. Varying one of the remaining parameters, while keeping the others fixed at unity, did not reveal any new types of flow within the interfacial droplet. The reason for this is that at $\tau_{12} \approx 1$ the thermocapillary flow generated at the planar interface dominates. One possibility for uncovering unique flow structures would be to consider only cases for which τ_{12} is small and varying the remaining parameters. Even restricting the possible choices for the remaining parameters to just a few values would result in a plethora of flow fields to examine. Such an exhaustive examination has not been carried out at this time.

4.10 Conclusions

In this chapter a boundary collocation scheme was developed and utilized to find the temperature and velocity fields for an interfacial droplet. This was necessary to test the validity of the submerged droplet model of Chapter 3. The submerged droplet model was not able to provide a qualitatively accurate solution for a droplet that was very near the air-substrate interface or for a droplet whose thermal conductivity

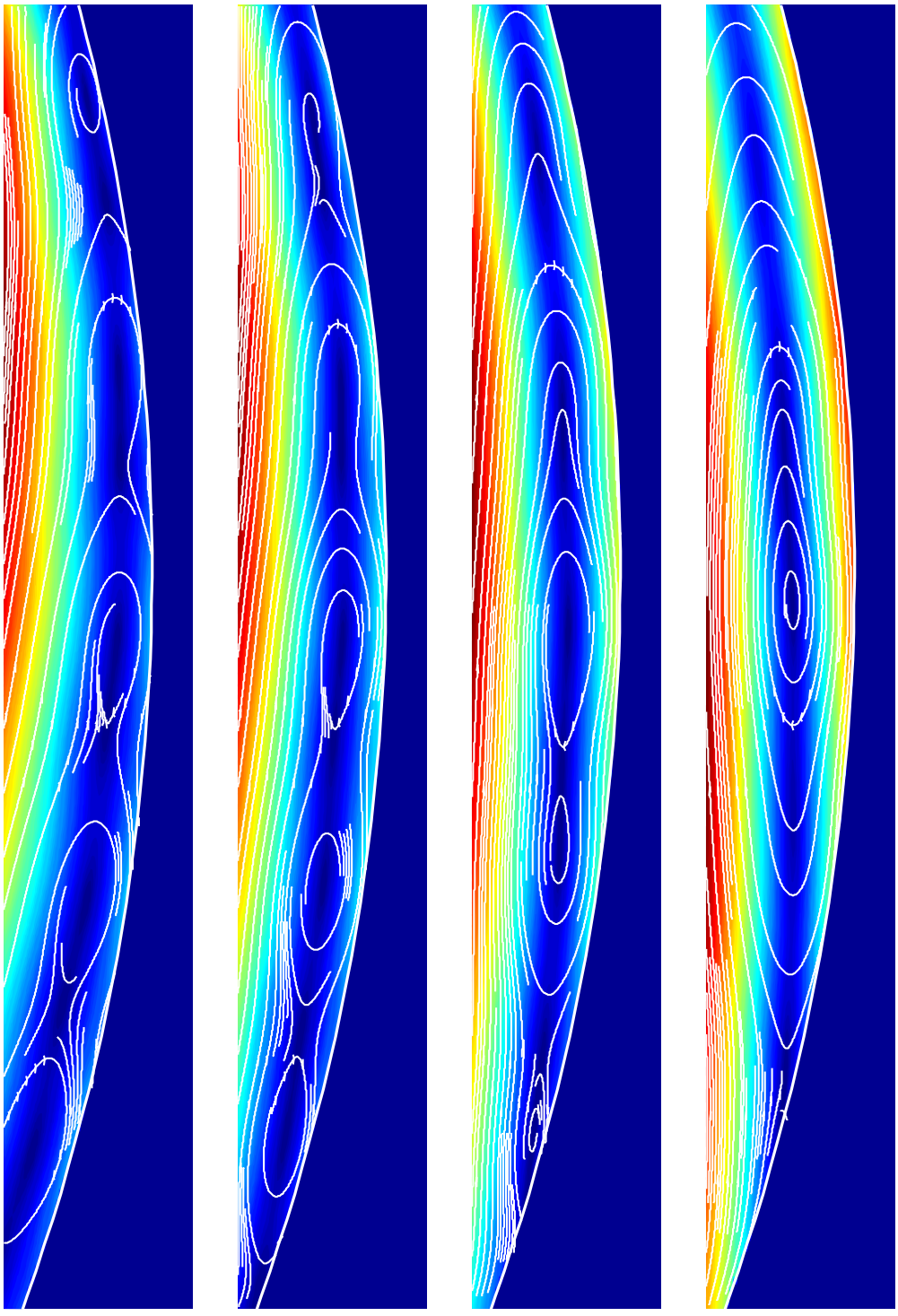

(a) (b) (c) (d)

Figure 42: A collection of flow patterns predicted for small droplet viscosity by the interfacial droplet solution. These flow structures were not found for the submerged droplet model. (a) $\tau_{12} = 1$,(a) $\tau_{12} = 2$,(c) $\tau_{12} = 4$ and (d) $\tau_{12} = 8$.

differed from the substrate. For most values of the material and interfacial parameters the results for the interfacial droplet were in good agreement with the submerged droplet model.

As part of the solution for the velocity field the migration velocity of the droplet was also determined. For most cases it was found that an interfacial droplet would migrate more slowly and in the opposite direction than a droplet in an unbounded substrate. It was determined that this was due to the increased drag the planar interface placed on the droplet. There were two exceptions to this rule of thumb. The first was when the viscosity of the covering fluid was greater than the viscosity of the substrate. The other case was when the temperature coefficient of surface tension at the top of the droplet was less than at the bottom. In both of these limits, the thermocapillary forcing from the surface of the droplet was reduced and the droplet was able to advect more rapidly towards cooler regions of fluid.

Another question, concerning interfacial droplets, was what effect the shape of the droplet and its contact line would have on the flow structure. It was determined that the shape of the droplet had very little to do with types of flows observed inside the droplet as long as it was near spherical. What was more important was the level of submersion within the substrate. For a drop mostly exposed to the covering fluid or nearly submerged in the substrate, the contact line would form the vertex of an acute wedge domain that oncoming fluid would flow into and stagnate. The flow in this region was difficult to determine and often led to spurious results near the contact line. Fortuitously, this problem did not adversely effect the flow in other parts of the droplet.

The interfacial droplet was in good agreement with the submerged droplet model for flow in the center of the droplet. Near the surface of the droplet, generally, there was less agreement and new flow structures unique to interfacial droplets were found. While the entire parameter space was too large for a punctilious search, most

parameter cases of interest were investigated. In the limit of small droplet viscosity a new complex flow structure was found near the bottom surface of the droplet. It was determined that this structure was confined within a very thin shell and would not significantly affect the mixing properties throughout the interior of the droplet.

CHAPTER V

PREDICTIONS FOR THE MICROFLUIDIC EXPERIMENTER

5.1 Introduction

In this chapter the submerged droplet model and the numerical solution for an interfacial droplet are used to determine the flow structures arising in the digital microfluidic device of Grigoriev, Sharma and Schatz [11]. Computation of these flows is necessary to verify the validity of the simple mixing model proposed by Grigoriev [10] for this system. The microfluidic device used air as the covering fluid (fluid 1). Fluorinert FC-70 was used as the substrate (fluid 2) and the droplet (fluid 3) was a water/glycerin mixture. The values of most material parameters were taken from the CRC Handbook [23]. Some parameters, such as the temperature coefficients of surface tension and the temperature gradient were estimated. Other parameters (substrate thickness, droplet radius) were measured directly. In particular, the characteristic length, temperature, and velocity scales were taken to be $r_0 = 6.2 \times 10^{-5}$ m, $\Theta = 100$ K/m, and $v_0 = 3.0 \times 10^{-5}$m/s respectively.

The values of the corresponding nondimensional parameters are summarized in Table 5. The values for Re_1, Pe_1, Bo_1 and Ca_1 are not tabulated for the air layer due to its small values of density, viscosity and thermal conductivity. The flux of heat and momentum from air are too small to influence the temperature and velocity fields inside the droplet and the substrate fluid.

Most of the nondimensional parameters have the order of magnitude assumed throughout the analysis of Chapters 2, 3 and 4. A notable exception is the large value of the Péclet number Pe_2 in the substrate fluid. This means that at large distances

Table 5: Dimensionless parameters computed from Grigoriev *et al.* [11].

Viscosity	$\alpha_1 = 0.0008$	$\alpha_3 = 0.59$
Thermal conductivity	$\beta_1 = 0.036$	$\beta_3 = 5.9$
Surface tension	$\gamma_{12} = 0.33$	$\gamma_{13} = 1.2$
Temperature coefficient	$\tau_{12} = 0.59$	$\tau_{13} = 1.2$
Bond number	$Bo_2 = 0.004$	$Bo_3 = 0.0008$
capillary number	$Ca_2 = 1\times10^{-5}$	$Ca_3 = 7\times10^{-6}$
Thermal Péclet number	$Pe_2 = 140$	$Pe_3 = 0.02$
Reynolds number	$Re_2 = 0.38$	$Re_3 = 2\times10^{-4}$
Length	$\lambda = 4 \times 10^4$	$\chi = 64$

from the droplet, heat transport is advection,rather than diffusion, dominated and hence the asymptotic solution in the substrate is inaccurate. As was discussed in each of those chapters, the validity of the models can be restored by reducing the imposed temperature gradient.

5.2 Predicted Migration Velocities

Using the parameter values gleaned from Table 5, the dimensional migration velocity U_0 for an interfacial droplet was determined to be roughly one millimeter per second in the $-\hat{\mathbf{x}}$ direction. The submerged droplet model predicts a speed in the same direction and differs from the interfacial droplet results by less than 1%. In calculating U_0 from the submerged droplet model a value of $\delta = 1.25$ was chosen. By holding the parameters of Table 5 fixed, except one which is varied, the dependence on the migration velocity for the varied parameter can be determined. Experimentally the easiest parameters to vary are the droplet viscosity (e. g., by using salts or different water/glycerin ratios) and the temperature coefficients for surface tension (using surfactants).

The change in the migration velocity for the parameters α_3, τ_{12} and τ_{13} is given in Fig. 43. These results were calculated using the interfacial droplet solution procedure. The trend observed in the migration velocity for α_3 and β_3 agrees nicely with the

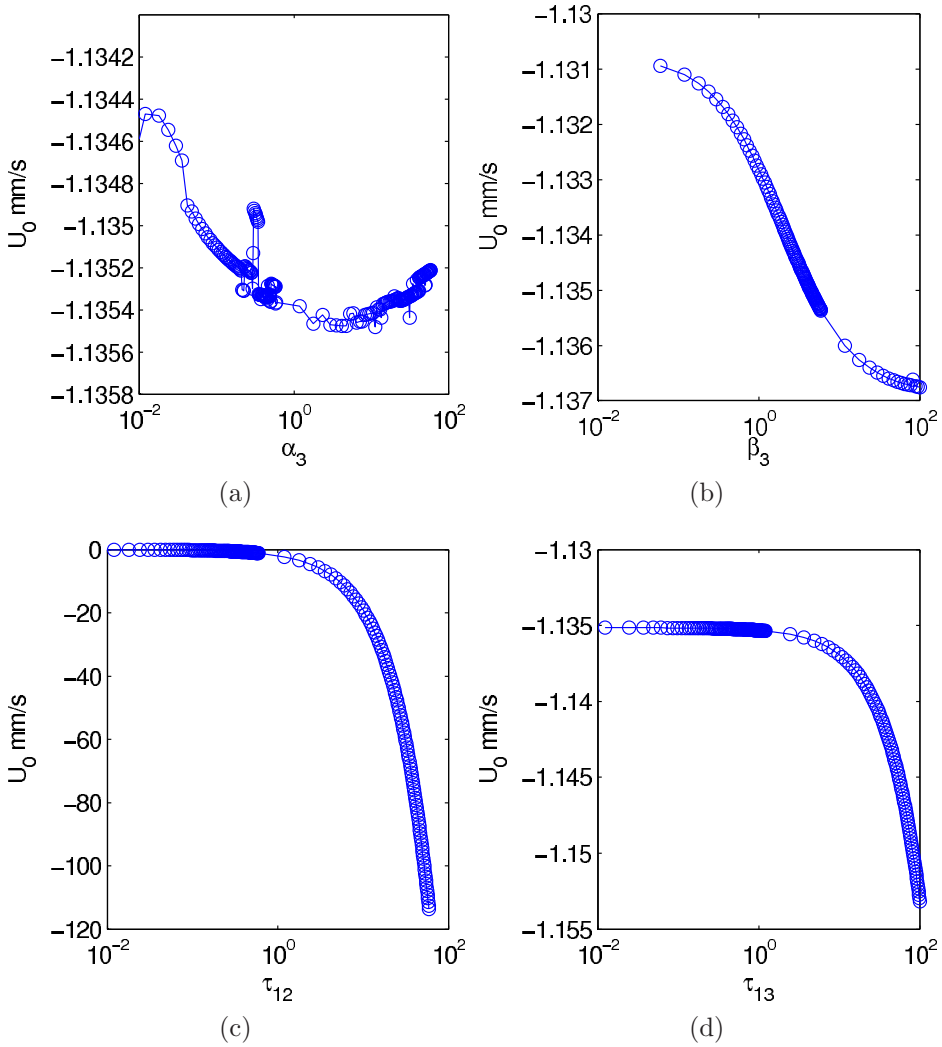

Figure 43: The migration velocity (in mm/s) of an interfacial drop with lab values.

analysis of Chapter 4. In the case of τ_{12} and τ_{13} the opposite of what was expected is observed. The interfacial droplet migrates faster than expected for larger values of those parameters. This is most likely due to the remaining parameters of Table 5 not being nearly unity (as during the analysis). This allows multiple effects, such as line force, thermocapillary forcing and planar interface drag, to compete for control of the droplet.

5.3 Predicted Flow Profiles

Stream plots of the flow in the $y = 0$ plane and the level sets of v_x at $x = 0$ are shown in Fig. 44 for both the numerical solution and the submerged droplet model. The topological structure of the flow is organized by a continuous set of elliptic fixed points in the $x = 0$ plane (see Fig. 45), anchored at the z axis near the top of the droplet and extending all the way to the droplet surface. The bulk of the fluid inside the droplet circulates around the curved line representing this set of fixed points. A quick comparison shows that the flow is quite similar to the submerged droplet for the same values of parameters. One should therefore expect the model to provide a qualitatively accurate description of the flow (and hence its mixing properties) almost everywhere inside an interfacial droplet.

On the other hand, one finds that the simplified model – for the same values of parameters – does not capture some finer details of the flow near the droplet's surface, such as the pairs of spiral and saddle fixed points (see Fig. 44b) and the heteroclinic orbits connecting those spirals (see Fig. 45). The emergence of such invariant structures can, in principle, radically alter the mixing properties of the flow near the surface (and possibly near the $y = 0$ plane). In practice, however, the regions where the predictions of the submerged droplet model disagree with the interfacial droplet solution are characterized by small values of the velocity, so in either case the flow will have poor mixing properties in such regions. To be fair, for slightly different values of parameters (i. e. for smaller values of α_3) similar spiral flow structures arise near the droplet surface in the submerged droplet model. These were the topic of discussion in Chapter 3. There, the spiral flow structure was nicely illustrated in Fig. 23.

The interfacial droplet solution for the flow outside the droplet is shown in Fig. 46. Two features of this flow are worth pointing out. First, for the values of parameters in Table 5 there are two stagnation points of the flow (or saddles) at the front of the

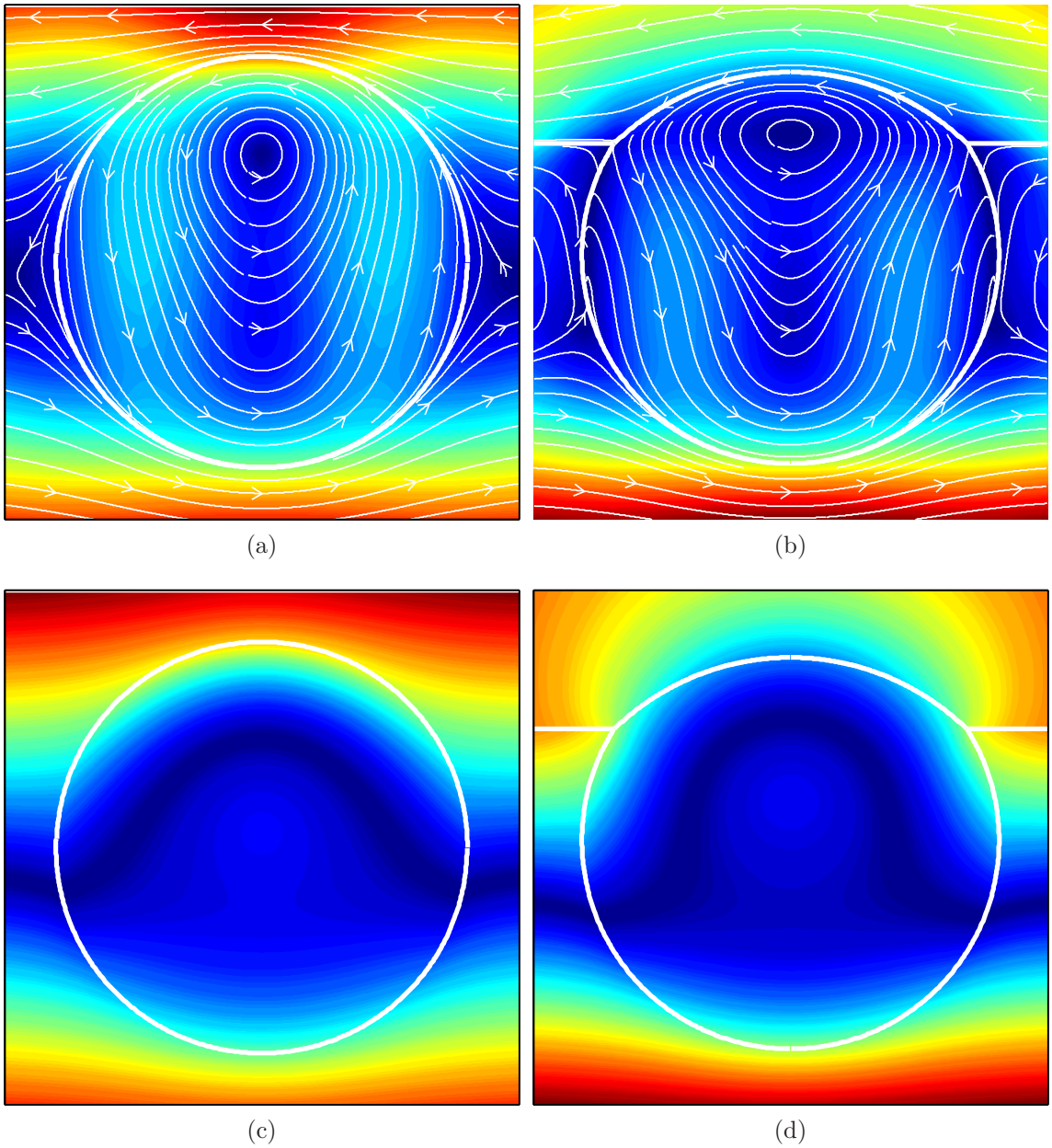

Figure 44: The flow field for the glycerin/water mixture. Shown are the streamlines for the submerged (a) and interfacial (b) droplet in the $y = 0$ plane and the level sets of v_x for the submerged (c) and interfacial (d) droplet in the $x = 0$ plane. The parameters are summarized in Table 5.

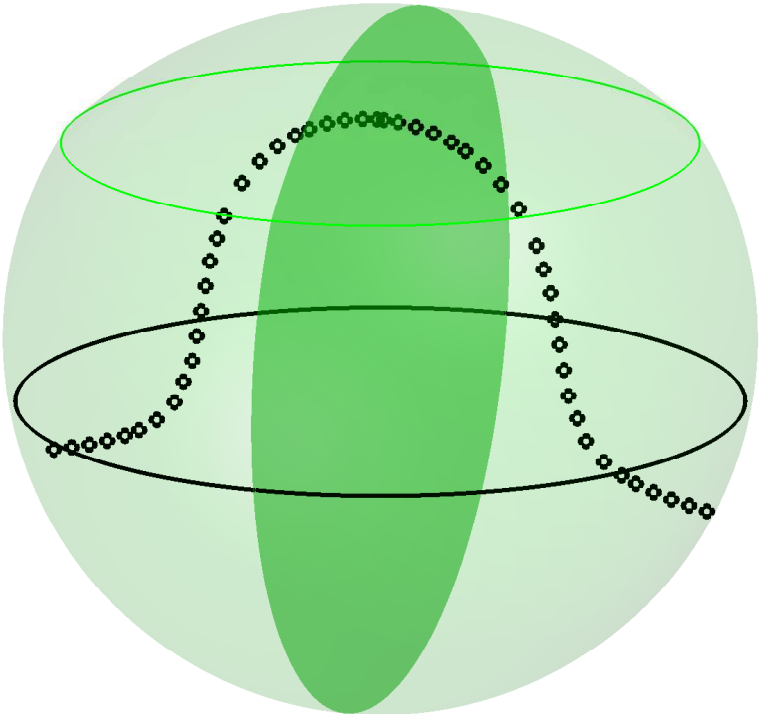

Figure 45: Invariant sets of the flow shown in Fig. 44. The open circles represent the set of elliptic fixed points in the $x = 0$ plane. The solid lines show pairs of heteroclinic orbits connecting spiral fixed points in the $y = 0$ plane. Both the surface of the droplet (light green) and the $y = 0$ plane (dark green) are also invariant sets.

droplet and two at the back (more typically one finds one stagnation point at the front and one at the back). The top pair corresponds to the triple contact line, while the bottom pair corresponds to the saddle-spiral complex (discussed above) and its mirror image on the other side of the droplet. Second, the disturbance in the exterior field due to the presence of the droplet is seen to decay very quickly with the distance to the droplet. Relatively close to the droplet, the outside flow is very similar to the asymptotic shear flow $\mathbf{V}^{\infty}$. It, therefore, should not be very surprising to find that the thermocapillary driven flow shown in Fig. 46 is qualitatively similar to the flow inside and around an interfacial droplet driven by external shear. The interested

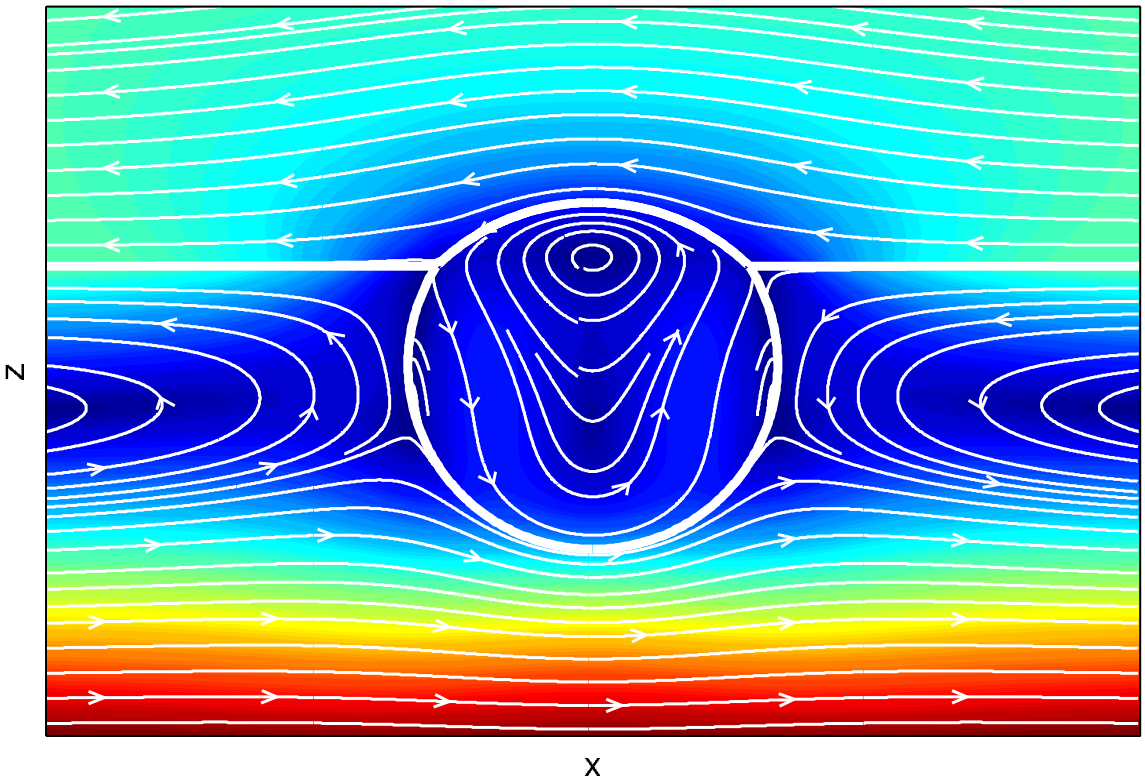

Figure 46: The exterior flow field for the interfacial droplet with the parameters taken from Table 5. Shown are the streamlines in the $y = 0$ plane.

reader may consult Fig. 6 of Ref. [38] for a comparision of the flow presented here and the flow structure of an interfacial droplet in an imposed shear.

For the microfluidic experimentalist the easiest parameter to modify is α_3, the ratio of the droplet viscosity to that of the substrate. With this in mind, the velocity field has been computed in the limits of small and large droplet viscosity. In particular, for pure water the relative viscosity is low, with $\alpha_3 = 0.043$. The corresponding numerical solution and the flow predicted by the submerged droplet model are shown in Fig. 47. Qualitative agreement over most of the droplet interior is also found in this case.

For a heavy glycerin/water mixture, also used in Ref. [11], the droplet is substantially more viscous than the substrate fluid, with $\alpha_3 = 4.9$. The corresponding solutions for this flow are shown in Fig. 48. In this limit, reasonable qualitative

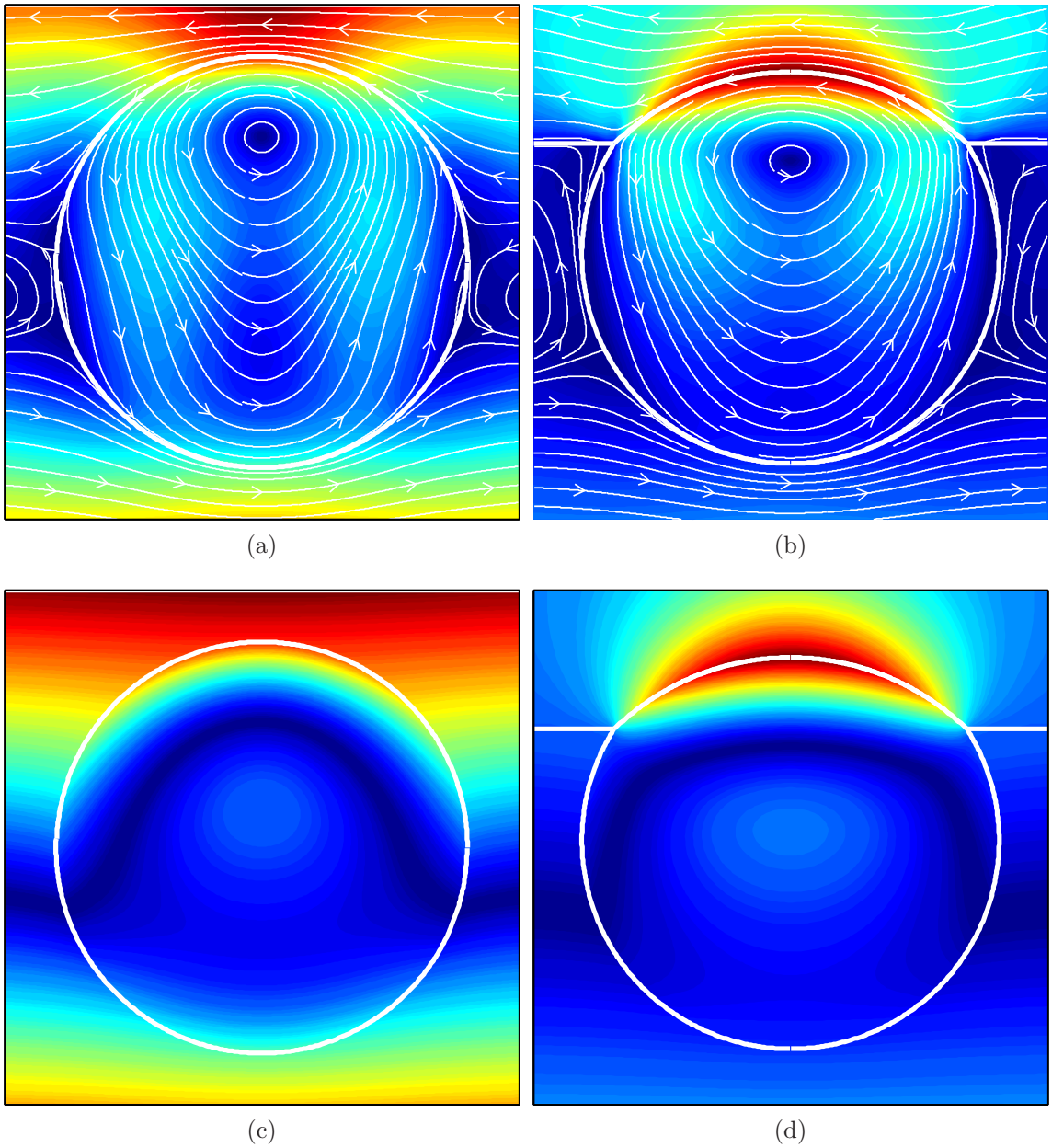

Figure 47: The flow field for an interfacial water droplet. Shown are the streamlines for the submerged (a) and interfacial (b) droplet in the $y = 0$ plane and the level sets of v_x for the submerged (c) and interfacial (d) droplet in the $x = 0$ plane. The parameters are summarized in Table 5 except for $\alpha_3 = 0.043$.

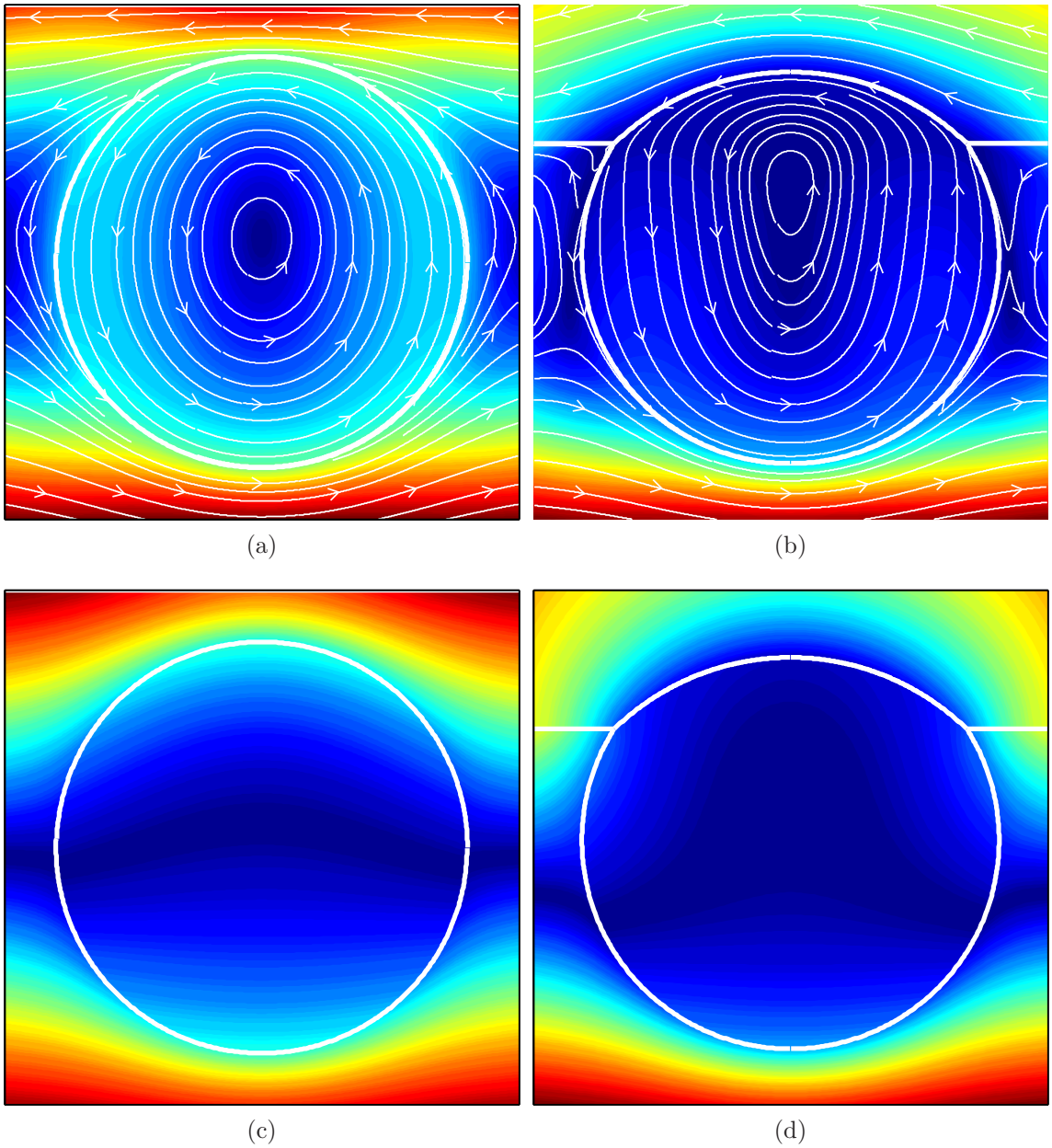

Figure 48: The flow field for the heavy glycerin/water interfacial droplet. Shown are the streamlines for the submerged (a) and interfacial (b) droplet in the $y = 0$ plane and the level sets of v_x for the submerged (c) and interfacial (d) droplet in the $x = 0$ plane. The parameters are summarized in Table 5 except for $\alpha_3 = 4.9$.

agreement was also determined between the interfacial and submerged droplet over most of the droplet interior. The submerged droplet model predicts the flow to be almost identical to solid rotation around the y axis (i. e. quasi-two-dimensional). The boundary conditions at the contact line, however, force the flow inside the interfacial droplet to retain a distinctly three-dimensional structure, as the level sets of v_x shown in Fig. 48d illustrate.

5.4 Conclusions

The parameter space of the interfacial droplet problem is too large to be fully explored. However, changing even just a few of the parameters relative to the experimental values can produce interior flows with substantially more complex structures. One such flow is presented in Fig. 49, where two parameters have been changed: $\gamma_{12} = 0.62$ and $\tau_{13} = 6 \times 10^{-3}$. In contrast to the other cases considered in this chapter, the flow is organized around *two* sets of fixed points in the $x = 0$ plane extending from the z axis to the surface of the droplet (see Fig. 49b). While the bottom set is again composed of elliptic fixed points, the top set is made up of saddles near the axis and elliptic fixed points near the droplet surface.

This flow also contains a heteroclinic orbit connecting two spirals in the $y = 0$ plane near the droplet surface. The novel feature of the flow is that the spirals now affect the flow near the surface of the droplet and everywhere in the $y = 0$ plane. This effect is clearly visible in Fig. 49a and 49d. The submerged droplet model provides an adequate description of the flow *nowhere* inside the interfacial droplet. This is not entirely unexpected: the model flow does not permit such a drastic imbalances between the top and bottom surface tension gradients. The possibility of observing this type of flow structure was posited in the analysis of Chapter 4.

Summarizing, the migration velocities and flow patterns for an interfacial droplet were computed using parameter values matching the digital microfluidic device of

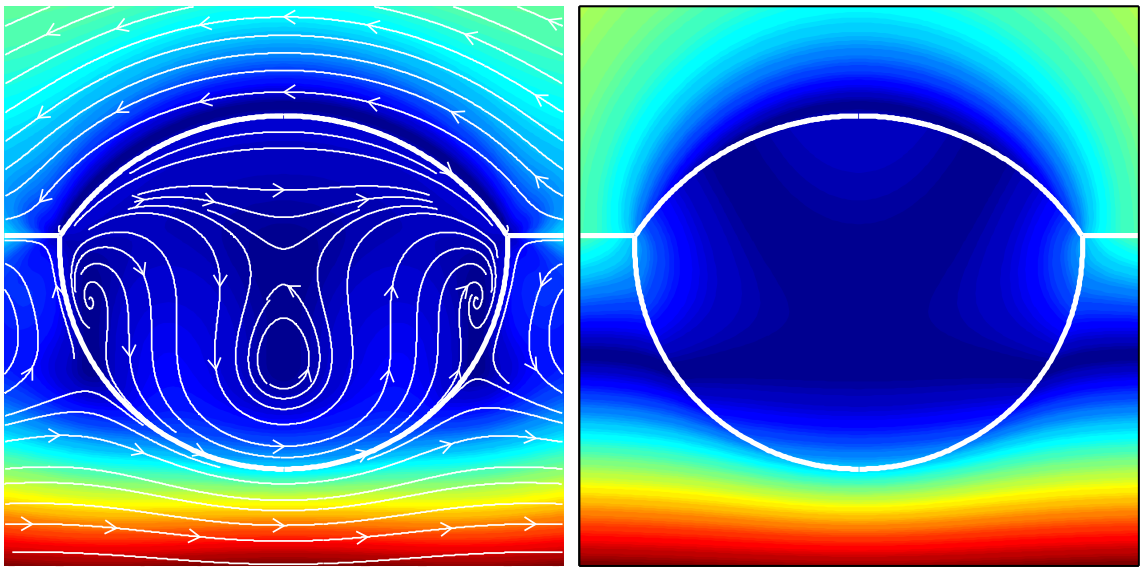

(a) (b)

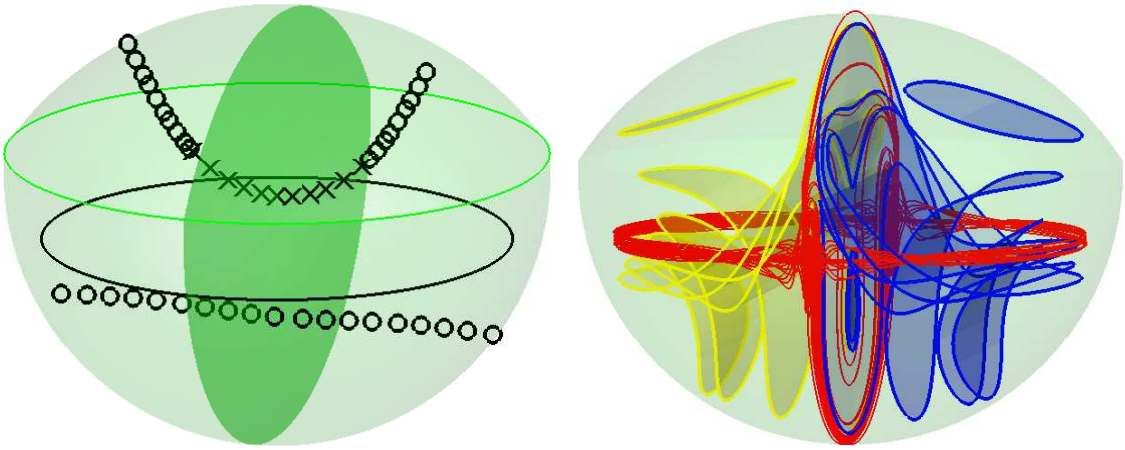

(c) (d)

Figure 49: The streamlines and level sets of an interfacial flow with complex topology. For convenience the flow invariants and several interior trajectories have been illustrated. (a) The streamlines in the $y = 0$ plane and (b) level sets in the $x = 0$ plane. (c) Invariant structures of the flow. The open circles and crosses represent the sets of elliptic and saddle fixed points, respectively, in the $x = 0$ plane. The solid line is a heteroclinic orbit connecting the stable and unstable spiral points. (d) representative trajectories of the flow inside the droplet. Some of the trajectories have been shaded to aid in their distinction. The parameters are as in Table. 5, except for $\gamma_{12} = 0.62$ and $\tau_{13} = 6 \times 10^{-3}$.

Ref. [11]. In addition, several parameter sets in the neighborhood of those taken from [11] were analyzed. This was done with the express hope of facilitating future comparisons with experimental data sets. During one such excursion into parameter space, a new and novel flow structure was found that could not be predicted by the submerged droplet model of Chapter 3. The difficulty of observing this flow experimentally remains to be seen. For most parameter sets considered, however, the simple model of a full submerged droplet doe a very good job of describing the experimental observations of [11].

CHAPTER VI

CONCLUSION

The research presented in this thesis was motivated by the desire to understand the flow field within a new digital microfluidic device currently under development. This required an investigation of the dynamics of a droplet migrating along the surface of another fluid. The quantitative analysis of the flow field presented in this thesis provides the first known solution for the velocity field in a droplet migrating at an interface due to a temperature gradient. While this thesis was primarily motivated by mixing in microfluidic devices, the results of this research may prove to be beneficial in many applications where the behavior of small bubbles and drops is important.

The first step towards gaining insight into the flow field was made with an improvement on the simple model developed by Grigoriev [10]. This simple model was limited to the idealized case of a droplet in an unbounded substrate to facilitate a study of the thermocapillary mixing within a droplet. The improvement to this model was achieved by using the method of reflections to obtain an analytical solution for the temperature and velocity fields inside and outside a submerged droplet migrating near a free surface. This model is the first successful attempt at applying the method of reflections to thermocapillary-driven flows for droplets migrating near a free surface.

The fully submerged droplet model enabled further analysis of the effects of the fluid properties on the velocity field and droplet migration speed. To simultaneously account for the surface tension gradients at both fluid interfaces, part of this analysis was limited to the special case of equal thermal conductivity coefficients. This was due to the lack of an analytical solution for the velocity field generated by non uniform

temperature gradients at the air-substrate interface.

In general, the migration velocity of the submerged drop model was found to differ dramatically from the classic problem of thermocapillary migration in an unbounded substrate. Most importantly, in most cases the submerged droplets were found to migrate in a direction opposite to the temperature gradient. In the classic problem of an isolated droplet, the migration is always in the direction of the gradient. It is, in principle, possible to find the parameters for which the direction of the migration for a submerged droplet is reversed. This requires the temperature coefficient of surface tension at the substrate's free surface to be small compared to that at the droplet surface. While such a situation is highly unlikely to occur in an experiment, it does provide a nice parallel to the arrest of buoyant gas bubbles observed by Young *et al.* [50].

To determine the flow field and migration velocity of a droplet floating trapped at the air-substrate interface, a boundary-collocation scheme was developed. The numerical solution produced by this scheme was compared to the velocity field of submerged droplet model using parameter values taken from the digital microfluidic device of [11]. It was determined that the submerged droplet model captured most of the flow structure within the microfluidic droplet. In particular, the droplet shape deformation caused by the contact line was found to be negligible for the specific parameter values of the device. One assumption that was found to be in disagreement with the experiment is that of negligible advective heat transport (small thermal Péclet number) in the substrate fluid. The disagreement could, however, be resolved by employing weaker temperature gradients.

The numerical method was found to produce accurate solutions for the velocity and temperature fields inside and outside of the droplet for nearly all choices of parameters. However, the numerical solutions were found to be unreliable when either (i) the droplet was strongly stretched due to a large surface tension at the

substrate's free surface, or (ii) the droplet was almost completely expelled by, or immersed in, the substrate. In both cases the condition number of the system of equations, which represents the boundary conditions evaluated at the collocation rings, becomes extremely large. This illustrates the limitations of the Lamb's spherical harmonic expansions in strongly non-spherical geometries.

6.1 What about mixing?

This study was largely motivated by the problem of mixing inside thermocapillary driven droplets. A detailed analysis of the flow field, using the boundary collocation scheme, did not uncover flow structures within the drop that would significantly affect mixing. Due to symmetry of the flow, essentially all trajectories of the flow remain closed. This prevents mixing via chaotic advection. Efficient mixing requires the destruction of the flow invariants. All of the complex flow structures discovered in this research were found to be contained within very small regions near the droplet surface. Furthermore, the flow in these regions was always nearly stagnant. Together, these two features dealt a death blow to any chance of complete mixing within the droplet.

The apparent lack of efficient mixing is, in all likelihood, a consequence of the very nature of the imposed temperature gradient. Throughout this research, any nonuniformity of the imposed temperature gradient was neglected. This was due to the belief that in the experimental system of [11], the temperature field near the drop was linear. Grigoriev [10], and more recently Vainchtein *et al.* [45], showed that it is essential to incorporate a symmetry breaking, nonuniform, asymptotic temperature gradient for effective mixing inside the droplet. Inclusion of this effect in the present model is challenging, since no analytical solution for the corresponding asymptotic velocity field $\mathbf{V}^{\infty}$ is available.

One possibility is to reexamine the orientation of the imposed temperature field to

the air-substrate interface. In modeling the microfluidic system of [11] it was assumed that the action of a laser sheet heating the fluid substrate could be approximated by a solid end wall maintained at a constant temperature. This resulted in variations in the asymptotic temperature field parallel to the planar interface. In reality the laser sheet does not maintain the entire depth of the substrate at a constant temperature. Instead, the amount of heat absorbed by the substrate will decay with increasing distance from the interface. This will give rise to an asymptotic temperature field with variations normal to the air-substrate interface. It is likely these additional variations will provide the required symmetry breaking to achieve mixing in the models developed in this thesis. Incorporation of these effects into the present models is currently underway.

APPENDIX A

COEFFICIENTS OF THE SUBMERGED DROP MODEL

Listed below are the values of the coefficients in Lamb's solution for a submerged droplet. These values were found using the method of reflections. They are arranged by powers of ϵ in Tables (6,7,8) for the interior field and Tables (10,11,12) for the exterior field in the limit $\tau_{12} = 0$. Tables (14, 16, 17) for the interior field and Tables (21,22,24) for the exterior field in the limit $\beta_3 = 1$.

To find the value of the coefficient to a given order, each element in the table is first multiplied by the power of ϵ corresponding to that element's column. The resulting products are then added up across that coefficients row to the desired order. The complete interior field is found by direct substitution into the general solution. The complete exterior velocity field is given by substituting the resultant coefficients into the general solution and adding its reflection.

Table 6: The coefficients for the interior velocity field (65) for $\epsilon^i, \quad i = 0..4$.

	$\epsilon^{\mathbf{0}}$	$\epsilon^{\mathbf{3}}$	$\epsilon^{\mathbf{4}}$
$\mathbf{B_3^1}$	$-30\,\frac{\alpha_3}{(\beta_3+2)(2+3\,\alpha_3)}$	$30\,\frac{\alpha_3\,(-1+\beta_3)}{(\beta_3+2)^2(2+3\,\alpha_3)}$	0
$\mathbf{B_3^2}$	0	0	$21\,\frac{\alpha_3\,(-5-3\,\alpha_3+3\,\beta_3\,\alpha_3)}{(2\,\beta_3+3)(\beta_3+2)(\alpha_3+1)(2+3\,\alpha_3)}$
$\mathbf{B_3^3}$	0	0	0
$\mathbf{B_3^4}$	0	0	0
$\mathbf{B_3^5}$	0	0	0
$\mathbf{B_3^6}$	0	0	0
$\mathbf{C_3^1}$	$5\,\frac{1}{(\beta_3+2)(2+3\,\alpha_3)}$	$-3\,\frac{-1+2\,\beta_3}{(\beta_3+2)^2(2+3\,\alpha_3)}$	0
$\mathbf{C_3^2}$	0	0	$-3/2\,\frac{-5-3\,\alpha_3+3\,\beta_3\,\alpha_3}{(2\,\beta_3+3)(\beta_3+2)(\alpha_3+1)(2+3\,\alpha_3)}$
$\mathbf{C_3^3}$	0	0	0
$\mathbf{C_3^4}$	0	0	0
$\mathbf{C_3^5}$	0	0	0
$\mathbf{C_3^6}$	0	0	0
$\mathbf{D_3^1}$	0	0	0
$\mathbf{D_3^2}$	0	0	0
$\mathbf{D_3^3}$	0	0	0
$\mathbf{D_3^4}$	0	0	0
$\mathbf{D_3^5}$	0	0	0
$\mathbf{D_3^6}$	0	0	0

Table 7: The coefficients for the interior velocity field (65) for ϵ^5 and ϵ^6.

	$\epsilon^{\mathbf{5}}$	$\epsilon^{\mathbf{6}}$
$\mathbf{B_3^1}$	0	$-30\,\frac{(-1+\beta_3)^2\alpha_3}{(\beta_3+2)^3(2+3\,\alpha_3)}$
$\mathbf{B_3^2}$	0	0
$\mathbf{B_3^3}$	$9\,\frac{\alpha_3\,(-28-12\,\alpha_3-7\,\beta_3+12\,\beta_3\,\alpha_3)}{(\beta_3+2)(3\,\beta_3+4)(\alpha_3+1)(2+3\,\alpha_3)}$	0
$\mathbf{B_3^4}$	0	$33\,\frac{\alpha_3\,(-15-5\,\alpha_3-6\,\beta_3+5\,\beta_3\,\alpha_3)}{(\beta_3+2)(4\,\beta_3+5)(\alpha_3+1)(2+3\,\alpha_3)}$
$\mathbf{B_3^5}$	0	0
$\mathbf{B_3^6}$	0	0
$\mathbf{C_3^1}$	0	$3\,\frac{(-1+\beta_3)(-1+2\,\beta_3)}{(\beta_3+2)^3(2+3\,\alpha_3)}$
$\mathbf{C_3^2}$	0	0
$\mathbf{C_3^3}$	$-1/2\,\frac{-28-12\,\alpha_3-7\,\beta_3+12\,\beta_3\,\alpha_3}{(\beta_3+2)(3\,\beta_3+4)(\alpha_3+1)(2+3\,\alpha_3)}$	0
$\mathbf{C_3^4}$	0	$-3/2\,\frac{-15-5\,\alpha_3-6\,\beta_3+5\,\beta_3\,\alpha_3}{(\beta_3+2)(4\,\beta_3+5)(\alpha_3+1)(2+3\,\alpha_3)}$
$\mathbf{C_3^5}$	0	0
$\mathbf{C_3^6}$	0	0
$\mathbf{D_3^1}$	0	0
$\mathbf{D_3^2}$	0	0
$\mathbf{D_3^3}$	0	0
$\mathbf{D_3^4}$	0	0
$\mathbf{D_3^5}$	0	0
$\mathbf{D_3^6}$	0	0

Table 8: The coefficients for the interior velocity field (65) for ϵ^7.

	$\epsilon^{\mathbf{7}}$
$\mathbf{B_3^1}$	0
$\mathbf{B_3^2}$	$-21/2\,\frac{\alpha_3\left(28\,\alpha_3+10+6\,{\alpha_3}^2+22\,\beta_3\,\alpha_3+10\,\beta_3-12\,{\alpha_3}^2\beta_3+25\,{\beta_3}^2\alpha_3+10\,{\beta_3}^2+6\,{\alpha_3}^2{\beta_3}^2\right)}{(2\,\beta_3+3)(\beta_3+2)^2(2+3\,\alpha_3)(\alpha_3+1)^2}$
$\mathbf{B_3^3}$	0
$\mathbf{B_3^4}$	0
$\mathbf{B_3^5}$	$39\,\frac{\alpha_3\,(-22-6\,\alpha_3-11\,\beta_3+6\,\beta_3\,\alpha_3)}{(\beta_3+2)(5\,\beta_3+6)(\alpha_3+1)(2+3\,\alpha_3)}$
$\mathbf{B_3^6}$	0
$\mathbf{C_3^1}$	0
$\mathbf{C_3^2}$	$3/4\,\frac{28\,\alpha_3+10+6\,{\alpha_3}^2+22\,\beta_3\,\alpha_3+10\,\beta_3-12\,{\alpha_3}^2\beta_3+25\,{\beta_3}^2\alpha_3+10\,{\beta_3}^2+6\,{\alpha_3}^2{\beta_3}^2}{(2\,\beta_3+3)(\beta_3+2)^2(2+3\,\alpha_3)(\alpha_3+1)^2}$
$\mathbf{C_3^3}$	0
$\mathbf{C_3^4}$	0
$\mathbf{C_3^5}$	$-3/2\,\frac{-22-6\,\alpha_3-11\,\beta_3+6\,\beta_3\,\alpha_3}{(\beta_3+2)(5\,\beta_3+6)(\alpha_3+1)(2+3\,\alpha_3)}$
$\mathbf{C_3^6}$	0
$\mathbf{D_3^1}$	$3/2\,\frac{6\,\alpha_3+10\,\beta_3+19\,\beta_3\,\alpha_3}{(\beta_3+2)(2\,\beta_3+3)(\alpha_3+1)(2+3\,\alpha_3)}$
$\mathbf{D_3^2}$	0
$\mathbf{D_3^3}$	0
$\mathbf{D_3^4}$	0
$\mathbf{D_3^5}$	0
$\mathbf{D_3^6}$	0

Table 9: The coefficients for the interior velocity field (65) for ϵ^8. $D_3^i = 0$ for $i = 3, 4, 5, 6$

	$\epsilon^{\mathbf{8}}$
$\mathbf{B_3^1}$	$-30\,\frac{\alpha_3\left(18\,\alpha_3+12+18\,{\alpha_3}^2-104\,\beta_3\,\alpha_3-44\,\beta_3-36\,{\alpha_3}^2\beta_3+11\,{\beta_3}^2\alpha_3+2\,{\beta_3}^2+18\,{\alpha_3}^2{\beta_3}^2\right)}{(2+3\,\alpha_3)^2(\beta_3+2)^2(2\,\beta_3+3)(\alpha_3+1)}$
$\mathbf{B_3^2}$	0
$\mathbf{B_3^3}$	$-3\,\frac{\alpha_3\left(252+744\,\alpha_3+198\,{\beta_3}^3+619\,\beta_3+1531\,\beta_3\,\alpha_3+1439\,{\beta_3}^2\alpha_3+108\,{\alpha_3}^2+611\,{\beta_3}^2-36\,{\alpha_3}^2{\beta_3}^2-144\,{\alpha_3}^2\beta_3+486\,{\beta_3}^3\alpha_3+72\,{\alpha_3}^2{\beta_3}^3\right)}{(\beta_3+2)^2(3\,\beta_3+4)(\alpha_3+1)^2(2\,\beta_3+3)(2+3\,\alpha_3)}$
$\mathbf{B_3^4}$	0
$\mathbf{B_3^5}$	0
$\mathbf{B_3^6}$	$15\,\frac{\alpha_3\,(-91-21\,\alpha_3-52\,\beta_3+21\,\beta_3\,\alpha_3)}{(\beta_3+2)(6\,\beta_3+7)(\alpha_3+1)(2+3\,\alpha_3)}$
$\mathbf{C_3^1}$	$3/4\,\frac{192+224\,\alpha_3+112\,{\beta_3}^3-920\,\beta_3-2128\,\beta_3\,\alpha_3-1084\,{\beta_3}^2\alpha_3+384\,{\alpha_3}^2-644\,{\beta_3}^2+403\,{\alpha_3}^2{\beta_3}^2-202\,{\alpha_3}^2\beta_3+468\,{\beta_3}^3\alpha_3+570\,{\alpha_3}^2{\beta_3}^3}{(2+3\,\alpha_3)^2(\beta_3+2)^2(2\,\beta_3+3)(\alpha_3+1)(3\,\beta_3+4)}$
$\mathbf{C_3^2}$	0
$\mathbf{C_3^3}$	$1/6\,\frac{252+744\,\alpha_3+198\,{\beta_3}^3+619\,\beta_3+1531\,\beta_3\,\alpha_3+1439\,{\beta_3}^2\alpha_3+108\,{\alpha_3}^2+611\,{\beta_3}^2-36\,{\alpha_3}^2{\beta_3}^2-144\,{\alpha_3}^2\beta_3+486\,{\beta_3}^3\alpha_3+72\,{\alpha_3}^2{\beta_3}^3}{(\beta_3+2)^2(3\,\beta_3+4)(\alpha_3+1)^2(2\,\beta_3+3)(2+3\,\alpha_3)}$
$\mathbf{C_3^4}$	0
$\mathbf{C_3^5}$	0
$\mathbf{C_3^6}$	$-1/2\,\frac{-91-21\,\alpha_3-52\,\beta_3+21\,\beta_3\,\alpha_3}{(\beta_3+2)(6\,\beta_3+7)(\alpha_3+1)(2+3\,\alpha_3)}$
$\mathbf{D_3^1}$	0
$\mathbf{D_3^2}$	$10/3\,\frac{6\,\alpha_3+10\,\beta_3+19\,\beta_3\,\alpha_3}{(\beta_3+2)(2\,\beta_3+3)(\alpha_3+4)(\alpha_3+1)(2+3\,\alpha_3)}$

Table 10: The coefficients for the exterior velocity field (65) for $\epsilon^i, \quad i = 0..4$.

	$\epsilon^{\mathbf{0}}$	$\epsilon^{\mathbf{3}}$	$\epsilon^{\mathbf{4}}$
$\mathbf{B_2^1}$	0	0	0
$\mathbf{B_2^2}$	0	0	$2\,\frac{6\,\alpha_3+10\,\beta_3+19\,\beta_3\,\alpha_3}{(2\,\beta_3+3)(\beta_3+2)(\alpha_3+1)(2+3\,\alpha_3)}$
$\mathbf{B_2^3}$	0	0	0
$\mathbf{B_2^4}$	0	0	0
$\mathbf{B_2^5}$	0	0	0
$\mathbf{B_2^6}$	0	0	0
$\mathbf{C_2^1}$	$-\frac{1}{(\beta_3+2)(2+3\,\alpha_3)}$	$\frac{-1+\beta_3}{(\beta_3+2)^2(2+3\,\alpha_3)}$	0
$\mathbf{C_2^2}$	0	0	$\frac{-2+2\,\beta_3+5\,\beta_3\,\alpha_3}{(2\,\beta_3+3)(\beta_3+2)(\alpha_3+1)(2+3\,\alpha_3)}$
$\mathbf{C_2^3}$	0	0	0
$\mathbf{C_2^4}$	0	0	0
$\mathbf{C_2^5}$	0	0	0
$\mathbf{C_2^6}$	0	0	0
$\mathbf{D_2^1}$	0	0	0
$\mathbf{D_2^2}$	0	0	0
$\mathbf{D_2^3}$	0	0	0
$\mathbf{D_2^4}$	0	0	0
$\mathbf{D_2^5}$	0	0	0
$\mathbf{D_2^6}$	0	0	0

Table 11: The coefficients for the exterior velocity field (65) for ϵ^5 and ϵ^6.

	$\epsilon^{\mathbf{5}}$	$\epsilon^{\mathbf{6}}$
$\mathbf{B_2^1}$	0	0
$\mathbf{B_2^2}$	0	0
$\mathbf{B_2^3}$	$\frac{15}{4}\,\frac{16\,\alpha_3+14\,\beta_3+33\,\beta_3\,\alpha_3}{(\beta_3+2)(3\,\beta_3+4)(\alpha_3+1)(2+3\,\alpha_3)}$	0
$\mathbf{B_2^4}$	0	$\frac{84}{5}\,\frac{10\,\alpha_3+6\,\beta_3+17\,\beta_3\,\alpha_3}{(\beta_3+2)(4\,\beta_3+5)(\alpha_3+1)(2+3\,\alpha_3)}$
$\mathbf{B_2^5}$	0	0
$\mathbf{B_2^6}$	0	0
$\mathbf{C_2^1}$	0	$-\frac{(-1+\beta_3)^2}{(\beta_3+2)^3(2+3\,\alpha_3)}$
$\mathbf{C_2^2}$	0	0
$\mathbf{C_2^3}$	$3/8\,\frac{-8+8\,\alpha_3+8\,\beta_3+27\,\beta_3\,\alpha_3}{(\beta_3+2)(3\,\beta_3+4)(\alpha_3+1)(2+3\,\alpha_3)}$	0
$\mathbf{C_2^4}$	0	$2/5\,\frac{-10+20\,\alpha_3+10\,\beta_3+43\,\beta_3\,\alpha_3}{(\beta_3+2)(4\,\beta_3+5)(\alpha_3+1)(2+3\,\alpha_3)}$
$\mathbf{C_2^5}$	0	0
$\mathbf{C_2^6}$	0	0
$\mathbf{D_2^1}$	0	0
$\mathbf{D_2^2}$	0	0
$\mathbf{D_2^3}$	0	0
$\mathbf{D_2^4}$	0	0
$\mathbf{D_2^5}$	0	0
$\mathbf{D_2^6}$	0	0

Table 12: The coefficients for the exterior velocity field (65) for ϵ^7.

	$\epsilon^{\mathbf{7}}$
$\mathbf{B_2^1}$	0
$\mathbf{B_2^2}$	$3\,\frac{(6\,\alpha_3+10\,\beta_3+19\,\beta_3\,\alpha_3)(\beta_3\,\alpha_3+4\,\alpha_3+2)}{(2\,\beta_3+3)(\beta_3+2)^2(2+3\,\alpha_3)(\alpha_3+1)^2}$
$\mathbf{B_2^3}$	0
$\mathbf{B_2^4}$	0
$\mathbf{B_2^5}$	$15/2\,\frac{48\,\alpha_3+22\,\beta_3+73\,\beta_3\,\alpha_3}{(\beta_3+2)(5\,\beta_3+6)(\alpha_3+1)(2+3\,\alpha_3)}$
$\mathbf{B_2^6}$	0
$\mathbf{C_2^1}$	0
$\mathbf{C_2^2}$	$1/2\,\frac{-4\,\alpha_3-4+12\,{\alpha_3}^2+38\,\beta_3\,\alpha_3+8\,\beta_3+54\,{\alpha_3}^2\beta_3-4\,\beta_3{}^2\alpha_3-4\,\beta_3{}^2+9\,{\alpha_3}^2\beta_3{}^2}{(2\,\beta_3+3)(\beta_3+2)^2(2+3\,\alpha_3)(\alpha_3+1)^2}$
$\mathbf{C_2^3}$	0
$\mathbf{C_2^4}$	0
$\mathbf{C_2^5}$	$5/4\,\frac{-4+12\,\alpha_3+4\,\beta_3+21\,\beta_3\,\alpha_3}{(\beta_3+2)(5\,\beta_3+6)(\alpha_3+1)(2+3\,\alpha_3)}$
$\mathbf{C_2^6}$	0
$\mathbf{D_2^1}$	0
$\mathbf{D_2^2}$	0
$\mathbf{D_2^3}$	0
$\mathbf{D_2^4}$	0
$\mathbf{D_2^5}$	0
$\mathbf{D_2^6}$	0

Table 13: The coefficients for the exterior velocity field (65) for ϵ^8. $D_3^i = 0$ for $i = 3, 4, 5, 6$

	$\epsilon^{\mathbf{8}}$
$\mathbf{B_2^1}$	0
$\mathbf{B_2^2}$	0
$\mathbf{B_2^3}$	$1/4\ \frac{1488\,\alpha_3+60\,{\beta_3}^3+1910\,\beta_3+9747\,\beta_3\,\alpha_3+7743\,{\beta_3}^2\alpha_3+3408\,{\alpha_3}^2+1390\,{\beta_3}^2+10673\,{\alpha_3}^2{\beta_3}^2+13117\,{\alpha_3}^2\beta_3+1182\,{\beta_3}^3\alpha_3+2202\,{\alpha_3}^2{\beta_3}^3}{{(\beta_3+2)}^2(3\,\beta_3+4){(\alpha_3+1)}^2(2\,\beta_3+3)(2+3\,\alpha_3)}$
$\mathbf{B_2^4}$	0
$\mathbf{B_2^5}$	0
$\mathbf{B_2^6}$	$\frac{66}{7}\ \frac{70\,\alpha_3+26\,\beta_3+99\,\beta_3\,\alpha_3}{(\beta_3+2)(6\,\beta_3+7)(\alpha_3+1)(2+3\,\alpha_3)}$
$\mathbf{C_2^1}$	$-3/5\ \frac{20+38\,\alpha_3-60\,\beta_3-124\,\beta_3\,\alpha_3+41\,{\beta_3}^2\alpha_3+42\,{\alpha_3}^2+10\,{\beta_3}^2+49\,{\alpha_3}^2{\beta_3}^2-16\,{\alpha_3}^2\beta_3}{(2\,\beta_3+3){(\beta_3+2)}^2{(2+3\,\alpha_3)}^2(\alpha_3+1)}$
$\mathbf{C_2^2}$	0
$\mathbf{C_2^3}$	$1/8\ \frac{-72-48\,{\beta_3}^3+96\,\beta_3+955\,\beta_3\,\alpha_3+695\,{\beta_3}^2\alpha_3+456\,{\alpha_3}^2+24\,{\beta_3}^2+1535\,{\alpha_3}^2{\beta_3}^2+1915\,{\alpha_3}^2\beta_3+30\,{\beta_3}^3\alpha_3+294\,{\alpha_3}^2{\beta_3}^3}{{(\beta_3+2)}^2(3\,\beta_3+4){(\alpha_3+1)}^2(2\,\beta_3+3)(2+3\,\alpha_3)}$
$\mathbf{C_2^4}$	0
$\mathbf{C_2^5}$	0
$\mathbf{C_2^6}$	$3/7\ \frac{-14+56\,\alpha_3+14\,\beta_3+87\,\beta_3\,\alpha_3}{(\beta_3+2)(6\,\beta_3+7)(\alpha_3+1)(2+3\,\alpha_3)}$
$\mathbf{D_2^1}$	0
$\mathbf{D_2^2}$	$-2/3\ \frac{(\alpha_3-1)(6\,\alpha_3+10\,\beta_3+19\,\beta_3\,\alpha_3)}{(\beta_3+2)(2\,\beta_3+3)(\alpha_3+4)(\alpha_3+1)(2+3\,\alpha_3)}$

Table 14: The coefficients for the interior velocity field (65) for ϵ^{i-3}, $\quad i = 1..6$.

	ϵ^{-2}	ϵ^{-1}	ϵ^{0}	ϵ^{2}	ϵ^{3}
$\mathbf{B_3^1}$	0	0	0	0	$-\frac{15}{4}\,\frac{\tau_{12}\,\alpha_3\,(5\,\alpha_3+2)}{\chi\,(\alpha_3+1)(3\,\alpha_3+2)}$
$\mathbf{B_3^2}$	0	$\frac{21}{8}\,\frac{\tau_{12}\,\alpha_3}{(\alpha_3+1)\chi}$	$-7/2\,\frac{\tau_{12}\,\alpha_3}{\alpha_3+1}$	$\frac{21}{16}\,\frac{\tau_{12}\,\alpha_3\,(5\,\alpha_3+2)}{\chi\,(\alpha_3+1)^2}$	$-7/4\,\frac{\tau_{12}\,\alpha_3\,(5\,\alpha_3+2)}{(\alpha_3+1)^2}$
$\mathbf{B_3^3}$	0	0	0	0	$3\,\frac{\tau_{12}\,\alpha_3\,(5\,\alpha_3+2)}{\chi\,(\alpha_3+1)^2}$
$\mathbf{B_3^4}$	0	0	0	0	0
$\mathbf{B_3^5}$	0	0	0	0	0
$\mathbf{B_3^6}$	0	0	0	0	0
$\mathbf{B_3^7}$	0	0	0	0	0
$\mathbf{B_3^8}$	0	0	0	0	0
$\mathbf{C_3^1}$	$-3/16\,\frac{\tau_{12}}{\chi}$	$1/2\,\tau_{12}$	$-1/4\,\chi\,\tau_{12}$	0	$-3/8\,\frac{\tau_{12}\left(8\,{\alpha_3}^2-\alpha_3-2\right)}{\chi\,(\alpha_3+1)(3\,\alpha_3+2)}$
$\mathbf{C_3^2}$	0	$-3/16\,\frac{\tau_{12}}{(\alpha_3+1)\chi}$	$1/4\,\frac{\tau_{12}}{\alpha_3+1}$	$-\frac{3}{32}\,\frac{\tau_{12}\,(5\,\alpha_3+2)}{\chi\,(\alpha_3+1)^2}$	$1/8\,\frac{\tau_{12}\,(5\,\alpha_3+2)}{(\alpha_3+1)^2}$
$\mathbf{C_3^3}$	0	0	0	0	$-1/6\,\frac{\tau_{12}\,(5\,\alpha_3+2)}{\chi\,(\alpha_3+1)^2}$
$\mathbf{C_3^4}$	0	0	0	0	0
$\mathbf{C_3^5}$	0	0	0	0	0
$\mathbf{C_3^6}$	0	0	0	0	0
$\mathbf{C_3^7}$	0	0	0	0	0
$\mathbf{C_3^8}$	0	0	0	0	0

Table 15: The coefficients for the interior velocity field (65) for ϵ^{i-3}, $\quad i = 1..6$.

	ϵ^{-2}	ϵ^{-1}	ϵ^{0}	ϵ^{2}	ϵ^{3}
$\mathbf{D_3^1}$	0	$3/8\,\frac{\tau_{12}}{\chi}$	$-1/2\,\tau_{12}$	$-3/16\,\frac{\tau_{12}\,(5\,\alpha_3+2)}{(\alpha_3+1)\chi}$	$1/4\,\frac{\tau_{12}\,(5\,\alpha_3+2)}{\alpha_3+1}$
$\mathbf{D_3^2}$	0	0	0	0	$-\frac{5}{12}\,\frac{\tau_{12}\,(5\,\alpha_3+2)}{\chi\,(\alpha_3+1)(\alpha_3+4)}$
$\mathbf{D_3^3}$	0	0	0	0	0
$\mathbf{D_3^4}$	0	0	0	0	0
$\mathbf{D_3^5}$	0	0	0	0	0
$\mathbf{D_3^6}$	0	0	0	0	0
$\mathbf{D_3^7}$	0	0	0	0	0
$\mathbf{D_3^8}$	0	0	0	0	0

Table 16: The coefficients for the interior velocity field (65) for ϵ^4 and ϵ^5.

	$\epsilon^{\mathbf{4}}$	$\epsilon^{\mathbf{5}}$
$\mathbf{B_3^1}$	$5\,\frac{\tau_{12}\,\alpha_3\,(5\,\alpha_3+2)}{(\alpha_3+1)(3\,\alpha_3+2)}$	0
$\mathbf{B_3^2}$	$-7\,\frac{\tau_{12}\,(1+4\,\alpha_3)\alpha_3}{\chi\,(\alpha_3+1)^2}$	$\frac{7}{96}\,\frac{\tau_{12}\,\alpha_3\left(640\,\chi\,\alpha_3+128\,\chi+512\,\chi\,{\alpha_3}^2+225\,{\alpha_3}^2+180\,\alpha_3+36\right)}{(\alpha_3+1)^3\chi}$
$\mathbf{B_3^3}$	$-4\,\frac{\tau_{12}\,\alpha_3\,(5\,\alpha_3+2)}{(\alpha_3+1)^2}$	$-\frac{45}{4}\,\frac{\tau_{12}\,\alpha_3\,(1+5\,\alpha_3)}{\chi\,(\alpha_3+1)^2}$
$\mathbf{B_3^4}$	$\frac{165}{32}\,\frac{\tau_{12}\,\alpha_3\,(5\,\alpha_3+2)}{\chi\,(\alpha_3+1)^2}$	$-\frac{55}{8}\,\frac{\tau_{12}\,\alpha_3\,(5\,\alpha_3+2)}{(\alpha_3+1)^2}$
$\mathbf{B_3^5}$	0	$\frac{39}{5}\,\frac{\tau_{12}\,\alpha_3\,(5\,\alpha_3+2)}{\chi\,(\alpha_3+1)^2}$
$\mathbf{B_3^6}$	0	0
$\mathbf{B_3^7}$	0	0
$\mathbf{B_3^8}$	0	0
$\mathbf{C_3^1}$	$1/2\,\frac{\tau_{12}\left(8\,{\alpha_3}^2-\alpha_3-2\right)}{(\alpha_3+1)(3\,\alpha_3+2)}$	0
$\mathbf{C_3^2}$	$1/2\,\frac{(1+4\,\alpha_3)\tau_{12}}{\chi\,(\alpha_3+1)^2}$	$-\frac{1}{192}\,\frac{\tau_{12}\left(640\,\chi\,\alpha_3+128\,\chi+512\,\chi\,{\alpha_3}^2+225\,{\alpha_3}^2+180\,\alpha_3+36\right)}{(\alpha_3+1)^3\chi}$
$\mathbf{C_3^3}$	$2/9\,\frac{\tau_{12}\,(5\,\alpha_3+2)}{(\alpha_3+1)^2}$	$5/8\,\frac{(1+5\,\alpha_3)\tau_{12}}{\chi\,(\alpha_3+1)^2}$
$\mathbf{C_3^4}$	$-\frac{15}{64}\,\frac{\tau_{12}\,(5\,\alpha_3+2)}{\chi\,(\alpha_3+1)^2}$	$\frac{5}{16}\,\frac{\tau_{12}\,(5\,\alpha_3+2)}{(\alpha_3+1)^2}$
$\mathbf{C_3^5}$	0	$-3/10\,\frac{\tau_{12}\,(5\,\alpha_3+2)}{\chi\,(\alpha_3+1)^2}$
$\mathbf{C_3^6}$	0	0
$\mathbf{C_3^7}$	0	0
$\mathbf{C_3^8}$	0	0
$\mathbf{D_3^1}$	0	$-\frac{3}{32}\,\frac{(5\,\alpha_3+2)^2\tau_{12}}{\chi\,(\alpha_3+1)^2}$
$\mathbf{D_3^2}$	$5/9\,\frac{\tau_{12}\,(5\,\alpha_3+2)}{(\alpha_3+1)(\alpha_3+4)}$	0
$\mathbf{D_3^3}$	$-\frac{35}{96}\,\frac{\tau_{12}\,(5\,\alpha_3+2)}{\chi\,(2\,\alpha_3+5)(\alpha_3+1)}$	$\frac{35}{72}\,\frac{\tau_{12}\,(5\,\alpha_3+2)}{(2\,\alpha_3+5)(\alpha_3+1)}$
$\mathbf{D_3^4}$	0	$-\frac{9}{80}\,\frac{\tau_{12}\,(5\,\alpha_3+2)}{(\alpha_3+2)(\alpha_3+1)\chi}$
$\mathbf{D_3^5}$	0	0
$\mathbf{D_3^6}$	0	0
$\mathbf{D_3^7}$	0	0
$\mathbf{D_3^8}$	0	0

Table 17: The coefficients for the interior velocity field (65) for ϵ^6.

	$\epsilon^{\mathbf{6}}$
$\mathbf{B_3^1}$	$-\frac{15}{8}\,\frac{\tau_{12}\,(5\,\alpha_3+2)^2\alpha_3}{\chi\,(3\,\alpha_3+2)(\alpha_3+1)^2}$
$\mathbf{B_3^2}$	$-\frac{7}{8}\,\frac{\tau_{12}\,(5\,\alpha_3+2)^2\alpha_3}{(\alpha_3+1)^3}$
$\mathbf{B_3^3}$	$3/2\,\frac{\tau_{12}\,\alpha_3\left(60\,\chi\,\alpha_3+10\,\chi+50\,\chi\,{\alpha_3}^2+25\,{\alpha_3}^2+20\,\alpha_3+4\right)}{(\alpha_3+1)^3\chi}$
$\mathbf{B_3^4}$	$-\frac{33}{2}\,\frac{(6\,\alpha_3+1)\tau_{12}\,\alpha_3}{\chi\,(\alpha_3+1)^2}$
$\mathbf{B_3^5}$	$-\frac{52}{5}\,\frac{\tau_{12}\,(5\,\alpha_3+2)\alpha_3}{(\alpha_3+1)^2}$
$\mathbf{B_3^6}$	$\frac{175}{16}\,\frac{\tau_{12}\,(5\,\alpha_3+2)\alpha_3}{\chi\,(\alpha_3+1)^2}$
$\mathbf{B_3^7}$	0
$\mathbf{B_3^8}$	0
$\mathbf{C_3^1}$	$3/16\,\frac{(5\,\alpha_3+2)\left(2\,{\alpha_3}^3+{\alpha_3}^2+24\,\alpha_3+8\right)\tau_{12}}{(\alpha_3+1)^2\chi\,(3\,\alpha_3+2)(\alpha_3+4)}$
$\mathbf{C_3^2}$	$1/16\,\frac{\tau_{12}\,(5\,\alpha_3+2)^2}{(\alpha_3+1)^3}$
$\mathbf{C_3^3}$	$-1/12\,\frac{\tau_{12}\left(60\,\chi\,\alpha_3+10\,\chi+50\,\chi\,{\alpha_3}^2+25\,{\alpha_3}^2+20\,\alpha_3+4\right)}{(\alpha_3+1)^3\chi}$
$\mathbf{C_3^4}$	$3/4\,\frac{(6\,\alpha_3+1)\tau_{12}}{\chi\,(\alpha_3+1)^2}$
$\mathbf{C_3^5}$	$2/5\,\frac{(5\,\alpha_3+2)\tau_{12}}{(\alpha_3+1)^2}$
$\mathbf{C_3^6}$	$-\frac{35}{96}\,\frac{(5\,\alpha_3+2)\tau_{12}}{\chi\,(\alpha_3+1)^2}$
$\mathbf{C_3^7}$	0
$\mathbf{C_3^8}$	0
$\mathbf{D_3^1}$	$1/8\,\frac{\tau_{12}\,(5\,\alpha_3+2)^2}{(\alpha_3+1)^2}$
$\mathbf{D_3^2}$	$-\frac{5}{24}\,\frac{\tau_{12}\,(5\,\alpha_3+2)^2}{\chi\,(\alpha_3+4)(\alpha_3+1)^2}$
$\mathbf{D_3^3}$	0
$\mathbf{D_3^4}$	$\frac{3}{20}\,\frac{(5\,\alpha_3+2)\tau_{12}}{(\alpha_3+2)(\alpha_3+1)}$
$\mathbf{D_3^5}$	$-\frac{77}{240}\,\frac{(5\,\alpha_3+2)\tau_{12}}{(4\,\alpha_3+7)(\alpha_3+1)\chi}$
$\mathbf{D_3^6}$	0
$\mathbf{D_3^7}$	0
$\mathbf{D_3^8}$	0

Table 18: The coefficients for the interior velocity field (65) for ϵ^7.

	$\epsilon^{\mathbf{7}}$
$\mathbf{B_3^1}$	$5/2\,\frac{(5\,\alpha_3+2)^2\tau_{12}\,\alpha_3}{(3\,\alpha_3+2)(\alpha_3+1)^2}$
$\mathbf{B_3^2}$	$-\frac{7}{8}\,\frac{\left(25\,\alpha_3+3\,{\alpha_3}^3-4+56\,{\alpha_3}^2\right)(5\,\alpha_3+2)\tau_{12}\,\alpha_3}{\chi\,(\alpha_3+4)(3\,\alpha_3+2)(\alpha_3+1)^3}$
$\mathbf{B_3^3}$	$-2\,\frac{(5\,\alpha_3+2)^2\tau_{12}\,\alpha_3}{(\alpha_3+1)^3}$
$\mathbf{B_3^4}$	$\frac{11}{64}\,\frac{\tau_{12}\,\alpha_3\left(768\,\chi\,{\alpha_3}^2+896\,\chi\,\alpha_3+128\,\chi+375\,{\alpha_3}^2+300\,\alpha_3+60\right)}{(\alpha_3+1)^3\chi}$
$\mathbf{B_3^5}$	$-\frac{91}{4}\,\frac{\tau_{12}\,(1+7\,\alpha_3)\alpha_3}{\chi\,(\alpha_3+1)^2}$
$\mathbf{B_3^6}$	$-\frac{175}{12}\,\frac{\tau_{12}\,(5\,\alpha_3+2)\alpha_3}{(\alpha_3+1)^2}$
$\mathbf{B_3^7}$	$\frac{102}{7}\,\frac{\tau_{12}\,(5\,\alpha_3+2)\alpha_3}{\chi\,(\alpha_3+1)^2}$
$\mathbf{B_3^8}$	0
$\mathbf{C_3^1}$	$-1/32\,\frac{\tau_{12}\,(5\,\alpha_3+2)\left(16\,{\alpha_3}^3\chi+8\,\chi\,{\alpha_3}^2+192\,\chi\,\alpha_3+64\,\chi+195\,{\alpha_3}^3+888\,{\alpha_3}^2+444\,\alpha_3+48\right)}{(\alpha_3+1)^2(3\,\alpha_3+2)(\alpha_3+4)\chi}$
$\mathbf{C_3^2}$	$1/16\,\frac{\left(25\,\alpha_3+3\,{\alpha_3}^3-4+56\,{\alpha_3}^2\right)(5\,\alpha_3+2)\tau_{12}}{\chi\,(\alpha_3+4)(3\,\alpha_3+2)(\alpha_3+1)^3}$
$\mathbf{C_3^3}$	$1/9\,\frac{(5\,\alpha_3+2)^2\tau_{12}}{(\alpha_3+1)^3}$
$\mathbf{C_3^4}$	$-\frac{1}{128}\,\frac{\tau_{12}\left(768\,\chi\,{\alpha_3}^2+896\,\chi\,\alpha_3+128\,\chi+375\,{\alpha_3}^2+300\,\alpha_3+60\right)}{(\alpha_3+1)^3\chi}$
$\mathbf{C_3^5}$	$\frac{7}{8}\,\frac{\tau_{12}\,(1+7\,\alpha_3)}{\chi\,(\alpha_3+1)^2}$
$\mathbf{C_3^6}$	$\frac{35}{72}\,\frac{\tau_{12}\,(5\,\alpha_3+2)}{(\alpha_3+1)^2}$
$\mathbf{C_3^7}$	$-3/7\,\frac{\tau_{12}\,(5\,\alpha_3+2)}{\chi\,(\alpha_3+1)^2}$
$\mathbf{C_3^8}$	0
$\mathbf{D_3^1}$	$-3/4\,\frac{(5\,\alpha_3+2)(2\,\alpha_3+3)\tau_{12}}{\chi\,(\alpha_3+4)(\alpha_3+1)^2}$
$\mathbf{D_3^2}$	$\frac{5}{18}\,\frac{(5\,\alpha_3+2)^2\tau_{12}}{(\alpha_3+4)(\alpha_3+1)^2}$
$\mathbf{D_3^3}$	$-\frac{35}{192}\,\frac{(5\,\alpha_3+2)^2\tau_{12}}{\chi\,(2\,\alpha_3+5)(\alpha_3+1)^2}$
$\mathbf{D_3^4}$	0
$\mathbf{D_3^5}$	$\frac{77}{180}\,\frac{\tau_{12}\,(5\,\alpha_3+2)}{(4\,\alpha_3+7)(\alpha_3+1)}$
$\mathbf{D_3^6}$	$-\frac{13}{42}\,\frac{\tau_{12}\,(5\,\alpha_3+2)}{\chi\,(5\,\alpha_3+8)(\alpha_3+1)}$
$\mathbf{D_3^7}$	0
$\mathbf{D_3^8}$	0

Table 19: The coefficients for the interior velocity field (65) for ϵ^8.

	$\epsilon^{\mathbf{8}}$
$\mathbf{B_3^1}$	$-15/2\,\frac{\tau_{12}\,(5\,\alpha_3+2)\alpha_3}{\chi\,(\alpha_3+1)^2}$
$\mathbf{B_3^2}$	$\frac{7}{384}\,\frac{\tau_{12}\,(5\,\alpha_3+2)\alpha_3\left((5184\,{\alpha_3}^2+1344\,\alpha_3+192\,{\alpha_3}^4+3776\,{\alpha_3}^3-256\,)\chi-19278\,{\alpha_3}^3-20628\,{\alpha_3}^2-7560\,\alpha_3-864-3645\,{\alpha_3}^4\right)}{(\alpha_3+4)(3\,\alpha_3+2)(\alpha_3+1)^4\chi}$
$\mathbf{B_3^3}$	$3/8\,\frac{\left(69\,{\alpha_3}^3+193\,{\alpha_3}^2+327\,\alpha_3+136\right)(5\,\alpha_3+2)\tau_{12}\,\alpha_3}{\chi\,(\alpha_3+4)(3\,\alpha_3+2)(\alpha_3+1)^3}$
$\mathbf{B_3^4}$	$-\frac{55}{16}\,\frac{(5\,\alpha_3+2)^2\tau_{12}\,\alpha_3}{(\alpha_3+1)^3}$
$\mathbf{B_3^5}$	$\frac{13}{30}\,\frac{\tau_{12}\,\alpha_3\left(560\,\chi\,\alpha_3+70\,\chi+490\,\chi\,{\alpha_3}^2+225\,{\alpha_3}^2+180\,\alpha_3+36\right)}{(\alpha_3+1)^3\chi}$
$\mathbf{B_3^6}$	$-30\,\frac{(8\,\alpha_3+1)\tau_{12}\,\alpha_3}{\chi\,(\alpha_3+1)^2}$
$\mathbf{B_3^7}$	$-\frac{136}{7}\,\frac{\tau_{12}\,(5\,\alpha_3+2)\alpha_3}{(\alpha_3+1)^2}$
$\mathbf{B_3^8}$	$\frac{1197}{64}\,\frac{\tau_{12}\,(5\,\alpha_3+2)\alpha_3}{\chi\,(\alpha_3+1)^2}$
$\mathbf{C_3^1}$	$1/16\,\frac{\tau_{12}\left(-216\,{\alpha_3}^4-747\,{\alpha_3}^3+246\,{\alpha_3}^2+792\,\alpha_3+240+1300\,{\alpha_3}^4\chi+4490\,{\alpha_3}^3\chi+3468\,\chi\,{\alpha_3}^2+952\,\chi\,\alpha_3+80\,\chi\right)}{\chi\,(2\,\alpha_3+5)(\alpha_3+1)^2(3\,\alpha_3+2)}$
$\mathbf{C_3^2}$	$-\frac{1}{768}\,\frac{\tau_{12}\,(5\,\alpha_3+2)\left(5184\,\chi\,{\alpha_3}^2+1344\,\chi\,\alpha_3+192\,{\alpha_3}^4\chi+3776\,{\alpha_3}^3\chi-256\,\chi-19278\,{\alpha_3}^3-20628\,{\alpha_3}^2-7560\,\alpha_3-864-3645\,{\alpha_3}^4\right)}{(\alpha_3+4)(3\,\alpha_3+2)(\alpha_3+1)^4\chi}$
$\mathbf{C_3^3}$	$-1/48\,\frac{\left(69\,{\alpha_3}^3+193\,{\alpha_3}^2+327\,\alpha_3+136\right)(5\,\alpha_3+2)\tau_{12}}{\chi\,(\alpha_3+4)(3\,\alpha_3+2)(\alpha_3+1)^3}$
$\mathbf{C_3^4}$	$\frac{5}{32}\,\frac{(5\,\alpha_3+2)^2\tau_{12}}{(\alpha_3+1)^3}$
$\mathbf{C_3^5}$	$-\frac{1}{60}\,\frac{\tau_{12}\left(560\,\chi\,\alpha_3+70\,\chi+490\,\chi\,{\alpha_3}^2+225\,{\alpha_3}^2+180\,\alpha_3+36\right)}{\chi\,(\alpha_3+1)^3}$
$\mathbf{C_3^6}$	$\frac{\tau_{12}\,(8\,\alpha_3+1)}{\chi\,(\alpha_3+1)^2}$
$\mathbf{C_3^7}$	$4/7\,\frac{\tau_{12}\,(5\,\alpha_3+2)}{(\alpha_3+1)^2}$
$\mathbf{C_3^8}$	$-\frac{63}{128}\,\frac{\tau_{12}\,(5\,\alpha_3+2)}{\chi\,(\alpha_3+1)^2}$

Table 20: The coefficients for the interior velocity field (65) for ϵ^8.

	$\epsilon^{\mathbf{8}}$
$\mathbf{D_3^1}$	$\frac{1}{128}\,\frac{\tau_{12}\,(5\,\alpha_3+2)\left(768\,{\alpha_3}^3\chi+2432\,\chi\,{\alpha_3}^2+2432\,\chi\,\alpha_3+768\,\chi+255\,{\alpha_3}^4+1002\,{\alpha_3}^3-180\,{\alpha_3}^2-456\,\alpha_3-96\right)}{\chi\,(\alpha_3+4)(3\,\alpha_3+2)(\alpha_3+1)^3}$
$\mathbf{D_3^2}$	$-\frac{5}{12}\,\frac{(5\,\alpha_3+2)\tau_{12}\left({\alpha_3}^2+16+18\,\alpha_3\right)}{\chi\,(\alpha_3+4)^2(\alpha_3+1)^2}$
$\mathbf{D_3^3}$	$\frac{35}{144}\,\frac{(5\,\alpha_3+2)^2\tau_{12}}{(2\,\alpha_3+5)(\alpha_3+1)^2}$
$\mathbf{D_3^4}$	$-\frac{9}{160}\,\frac{(5\,\alpha_3+2)^2\tau_{12}}{\chi\,(\alpha_3+2)(\alpha_3+1)^2}$
$\mathbf{D_3^5}$	0
$\mathbf{D_3^6}$	$\frac{26}{63}\,\frac{\tau_{12}\,(5\,\alpha_3+2)}{(5\,\alpha_3+8)(\alpha_3+1)}$
$\mathbf{D_3^7}$	$-\frac{45}{448}\,\frac{\tau_{12}\,(5\,\alpha_3+2)}{\chi\,(2\,\alpha_3+3)(\alpha_3+1)}$
$\mathbf{D_3^8}$	0

Table 21: The coefficients for the exterior velocity field (64) for ϵ^{i-3}, $\quad i = 1..6$.

	ϵ^{-1}	ϵ^{0}	ϵ^{2}	ϵ^{3}
$\mathbf{B_2^1}$	0	0	0	0
$\mathbf{B_2^2}$	$-1/4\,\frac{\tau_{12}\,(5\,\alpha_3+2)}{(\alpha_3+1)\chi}$	$1/3\,\frac{\tau_{12}\,(5\,\alpha_3+2)}{\alpha_3+1}$	$-1/8\,\frac{(5\,\alpha_3+2)^2\tau_{12}}{\chi\,(\alpha_3+1)^2}$	$1/6\,\frac{(5\,\alpha_3+2)^2\tau_{12}}{(\alpha_3+1)^2}$
$\mathbf{B_2^3}$	0	0	0	$-1/4\,\frac{\tau_{12}\,(5\,\alpha_3+2)(7\,\alpha_3+2)}{\chi\,(\alpha_3+1)^2}$
$\mathbf{B_2^4}$	0	0	0	0
$\mathbf{B_2^5}$	0	0	0	0
$\mathbf{B_2^6}$	0	0	0	0
$\mathbf{B_2^7}$	0	0	0	0
$\mathbf{B_2^8}$	0	0	0	0
$\mathbf{C_2^1}$	0	0	0	$\frac{3}{40}\,\frac{(\alpha_3-1)\tau_{12}\,(5\,\alpha_3+2)}{\chi\,(\alpha_3+1)(3\,\alpha_3+2)}$
$\mathbf{C_2^2}$	$-1/8\,\frac{\tau_{12}\,\alpha_3}{(\alpha_3+1)\chi}$	$1/6\,\frac{\tau_{12}\,\alpha_3}{\alpha_3+1}$	$-1/16\,\frac{\tau_{12}\,\alpha_3\,(5\,\alpha_3+2)}{\chi\,(\alpha_3+1)^2}$	$1/12\,\frac{\tau_{12}\,\alpha_3\,(5\,\alpha_3+2)}{(\alpha_3+1)^2}$
$\mathbf{C_2^3}$	0	0	0	$-1/8\,\frac{\tau_{12}\,\alpha_3\,(5\,\alpha_3+2)}{\chi\,(\alpha_3+1)^2}$
$\mathbf{C_2^4}$	0	0	0	0
$\mathbf{C_2^5}$	0	0	0	0
$\mathbf{C_2^6}$	0	0	0	0
$\mathbf{C_2^7}$	0	0	0	0
$\mathbf{C_2^8}$	0	0	0	0
$\mathbf{D_2^1}$	0	0	0	0
$\mathbf{D_2^2}$	0	0	0	$1/12\,\frac{(\alpha_3-1)\tau_{12}\,(5\,\alpha_3+2)}{\chi\,(\alpha_3+1)(\alpha_3+4)}$
$\mathbf{D_2^3}$	0	0	0	0
$\mathbf{D_2^4}$	0	0	0	0
$\mathbf{D_2^5}$	0	0	0	0
$\mathbf{D_2^6}$	0	0	0	0
$\mathbf{D_2^7}$	0	0	0	0
$\mathbf{D_2^8}$	0	0	0	0

Table 22: The coefficients for the exterior velocity field (64) for ϵ^4 and ϵ^5.

	$\epsilon^{\mathbf{4}}$	$\epsilon^{\mathbf{5}}$
$\mathbf{B_2^1}$	0	0
$\mathbf{B_2^2}$	$2\,\frac{\tau_{12}\,\alpha_3\,(5\,\alpha_3+2)}{\chi\,(\alpha_3+1)^2}$	$-\frac{1}{96}\,\frac{\tau_{12}\,\alpha_3\,(5\,\alpha_3+2)(256\,\chi\,\alpha_3+256\,\chi-315\,\alpha_3-126)}{(\alpha_3+1)^3\chi}$
$\mathbf{B_2^3}$	$1/3\,\frac{\tau_{12}\,(5\,\alpha_3+2)(7\,\alpha_3+2)}{(\alpha_3+1)^2}$	$\frac{75}{8}\,\frac{\tau_{12}\,\alpha_3\,(3\,\alpha_3+1)}{\chi\,(\alpha_3+1)^2}$
$\mathbf{B_2^4}$	$-3/8\,\frac{(5\,\alpha_3+2)(2+9\,\alpha_3)\tau_{12}}{\chi\,(\alpha_3+1)^2}$	$1/2\,\frac{(5\,\alpha_3+2)(2+9\,\alpha_3)\tau_{12}}{(\alpha_3+1)^2}$
$\mathbf{B_2^5}$	0	$-1/2\,\frac{\tau_{12}\,(5\,\alpha_3+2)(11\,\alpha_3+2)}{\chi\,(\alpha_3+1)^2}$
$\mathbf{B_2^6}$	0	0
$\mathbf{B_2^7}$	0	0
$\mathbf{B_2^8}$	0	0
$\mathbf{C_2^1}$	$-1/10\,\frac{(\alpha_3-1)\tau_{12}\,(5\,\alpha_3+2)}{(\alpha_3+1)(3\,\alpha_3+2)}$	0
$\mathbf{C_2^2}$	$1/21\,\frac{\tau_{12}\left(23\,{\alpha_3}^2-2\right)}{\chi\,(\alpha_3+1)^2}$	$-\frac{1}{4032}\,\frac{\tau_{12}\left(5888\,{\alpha_3}^3\chi+5888\,\chi\,{\alpha_3}^2-512\,\chi\,\alpha_3-512\,\chi+4725\,{\alpha_3}^2+3780\,\alpha_3+756\right)}{(\alpha_3+1)^3\chi}$
$\mathbf{C_2^3}$	$1/6\,\frac{\tau_{12}\,\alpha_3\,(5\,\alpha_3+2)}{(\alpha_3+1)^2}$	$\frac{5}{48}\,\frac{(1+4\,\alpha_3)(5\,\alpha_3-1)\tau_{12}}{\chi\,(\alpha_3+1)^2}$
$\mathbf{C_2^4}$	$-3/16\,\frac{\tau_{12}\,\alpha_3\,(5\,\alpha_3+2)}{\chi\,(\alpha_3+1)^2}$	$1/4\,\frac{\tau_{12}\,\alpha_3\,(5\,\alpha_3+2)}{(\alpha_3+1)^2}$
$\mathbf{C_2^5}$	0	$-1/4\,\frac{\tau_{12}\,\alpha_3\,(5\,\alpha_3+2)}{\chi\,(\alpha_3+1)^2}$
$\mathbf{C_2^6}$	0	0
$\mathbf{C_2^7}$	0	0
$\mathbf{C_2^8}$	0	0

Table 23: The coefficients for the exterior velocity field (64) for ϵ^4 and ϵ^5.

	$\epsilon^{\mathbf{4}}$	$\epsilon^{\mathbf{5}}$
$\mathbf{D_2^1}$	0	$-\frac{3}{32}\,\frac{(5\,\alpha_3+2)^2\tau_{12}}{\chi\,(\alpha_3+1)^2}$
$\mathbf{D_2^2}$	$-1/9\,\frac{(\alpha_3-1)\tau_{12}\,(5\,\alpha_3+2)}{(\alpha_3+1)(\alpha_3+4)}$	0
$\mathbf{D_2^3}$	$\frac{5}{48}\,\frac{(\alpha_3-1)\tau_{12}\,(5\,\alpha_3+2)}{\chi\,(2\,\alpha_3+5)(\alpha_3+1)}$	$-\frac{5}{36}\,\frac{(\alpha_3-1)\tau_{12}\,(5\,\alpha_3+2)}{(2\,\alpha_3+5)(\alpha_3+1)}$
$\mathbf{D_2^4}$	0	$\frac{3}{80}\,\frac{(\alpha_3-1)\tau_{12}\,(5\,\alpha_3+2)}{(\alpha_3+2)(\alpha_3+1)\chi}$
$\mathbf{D_2^5}$	0	0
$\mathbf{D_2^6}$	0	0
$\mathbf{D_2^7}$	0	0
$\mathbf{D_2^8}$	0	0

Table 24: The coefficients for the interior velocity field (65) for ϵ^6.

	$\epsilon^{\mathbf{6}}$
$\mathbf{B_2^1}$	$-\frac{15}{8}\,\frac{\tau_{12}\,(5\,\alpha_3+2)^2\alpha_3}{\chi\,(3\,\alpha_3+2)(\alpha_3+1)^2}$
$\mathbf{B_2^2}$	$-\frac{7}{8}\,\frac{\tau_{12}\,(5\,\alpha_3+2)^2\alpha_3}{(\alpha_3+1)^3}$
$\mathbf{B_2^3}$	$-1/2\,\frac{\tau_{12}\,\alpha_3\left(75\,\chi\,{\alpha_3}^2+100\,\chi\,\alpha_3+25\,\chi-75\,{\alpha_3}^2-60\,\alpha_3-12\right)}{(\alpha_3+1)^3\chi}$
$\mathbf{B_2^4}$	$\frac{42}{5}\,\frac{\alpha_3\,(7\,\alpha_3+2)\tau_{12}}{\chi\,(\alpha_3+1)^2}$
$\mathbf{B_2^5}$	$2/3\,\frac{\tau_{12}\,(5\,\alpha_3+2)(11\,\alpha_3+2)}{(\alpha_3+1)^2}$
$\mathbf{B_2^6}$	$-5/8\,\frac{(5\,\alpha_3+2)(13\,\alpha_3+2)\tau_{12}}{\chi\,(\alpha_3+1)^2}$
$\mathbf{B_2^7}$	0
$\mathbf{B_2^8}$	0
$\mathbf{C_2^1}$	$3/16\,\frac{(5\,\alpha_3+2)\left(2\,{\alpha_3}^3+{\alpha_3}^2+24\,\alpha_3+8\right)\tau_{12}}{(\alpha_3+1)^2\chi\,(3\,\alpha_3+2)(\alpha_3+4)}$
$\mathbf{C_2^2}$	$1/16\,\frac{\tau_{12}\,(5\,\alpha_3+2)^2}{(\alpha_3+1)^3}$
$\mathbf{C_2^3}$	$-1/36\,\frac{\tau_{12}\left(105\,\chi\,{\alpha_3}^2-5\,\chi+100\,{\alpha_3}^3\chi+75\,{\alpha_3}^2+60\,\alpha_3+12\right)}{(\alpha_3+1)^3\chi}$
$\mathbf{C_2^4}$	$\frac{3}{55}\,\frac{\tau_{12}\left(61\,{\alpha_3}^2+4\,\alpha_3-2\right)}{\chi\,(\alpha_3+1)^2}$
$\mathbf{C_2^5}$	$1/3\,\frac{\tau_{12}\,(5\,\alpha_3+2)\alpha_3}{(\alpha_3+1)^2}$
$\mathbf{C_2^6}$	$-\frac{5}{16}\,\frac{\tau_{12}\,(5\,\alpha_3+2)\alpha_3}{\chi\,(\alpha_3+1)^2}$
$\mathbf{C_2^7}$	0
$\mathbf{C_2^8}$	0
$\mathbf{D_2^1}$	$1/8\,\frac{\tau_{12}\,(5\,\alpha_3+2)^2}{(\alpha_3+1)^2}$
$\mathbf{D_2^2}$	$-\frac{5}{24}\,\frac{\tau_{12}\,(5\,\alpha_3+2)^2}{\chi\,(\alpha_3+4)(\alpha_3+1)^2}$
$\mathbf{D_2^3}$	0
$\mathbf{D_2^4}$	$-1/20\,\frac{\tau_{12}\,(5\,\alpha_3+2)(\alpha_3-1)}{(\alpha_3+2)(\alpha_3+1)}$
$\mathbf{D_2^5}$	$\frac{7}{60}\,\frac{\tau_{12}\,(5\,\alpha_3+2)(\alpha_3-1)}{(4\,\alpha_3+7)(\alpha_3+1)\chi}$
$\mathbf{D_2^6}$	0
$\mathbf{D_2^7}$	0
$\mathbf{D_2^8}$	0

Table 25: The coefficients for the interior velocity field (65) for ϵ^7.

	$\epsilon^{\mathbf{7}}$
$\mathbf{B_2^1}$	$5/2\,\frac{(5\,\alpha_3+2)^2\tau_{12}\,\alpha_3}{(3\,\alpha_3+2)(\alpha_3+1)^2}$
$\mathbf{B_2^2}$	$-\frac{7}{8}\,\frac{\left(25\,\alpha_3+3\,{\alpha_3}^3-4+56\,{\alpha_3}^2\right)(5\,\alpha_3+2)\tau_{12}\,\alpha_3}{\chi\,(\alpha_3+4)(3\,\alpha_3+2)(\alpha_3+1)^3}$
$\mathbf{B_2^3}$	$-2\,\frac{(5\,\alpha_3+2)^2\tau_{12}\,\alpha_3}{(\alpha_3+1)^3}$
$\mathbf{B_2^4}$	$-\frac{1}{320}\,\frac{\tau_{12}\,\alpha_3\left(25088\,\chi\,{\alpha_3}^2+32256\,\chi\,\alpha_3+7168\,\chi-20625\,{\alpha_3}^2-16500\,\alpha_3-3300\right)}{(\alpha_3+1)^3\chi}$
$\mathbf{B_2^5}$	$\frac{105}{4}\,\frac{\tau_{12}\,\alpha_3\,(1+4\,\alpha_3)}{\chi\,(\alpha_3+1)^2}$
$\mathbf{B_2^6}$	$5/6\,\frac{(5\,\alpha_3+2)(13\,\alpha_3+2)\tau_{12}}{(\alpha_3+1)^2}$
$\mathbf{B_2^7}$	$-3/4\,\frac{\tau_{12}\,(5\,\alpha_3+2)(15\,\alpha_3+2)}{\chi\,(\alpha_3+1)^2}$
$\mathbf{B_2^8}$	0
$\mathbf{C_2^1}$	$-1/32\,\frac{\tau_{12}\,(5\,\alpha_3+2)\left(16\,{\alpha_3}^3\chi+8\,\chi\,{\alpha_3}^2+192\,\chi\,\alpha_3+64\,\chi+195\,{\alpha_3}^3+888\,{\alpha_3}^2+444\,\alpha_3+48\right)}{(\alpha_3+1)^2(3\,\alpha_3+2)(\alpha_3+4)\chi}$
$\mathbf{C_2^2}$	$1/16\,\frac{\left(25\,\alpha_3+3\,{\alpha_3}^3-4+56\,{\alpha_3}^2\right)(5\,\alpha_3+2)\tau_{12}}{\chi\,(\alpha_3+4)(3\,\alpha_3+2)(\alpha_3+1)^3}$
$\mathbf{C_2^3}$	$1/9\,\frac{(5\,\alpha_3+2)^2\tau_{12}}{(\alpha_3+1)^3}$
$\mathbf{C_2^4}$	$-\frac{1}{7040}\,\frac{\tau_{12}\left(31232\,{\alpha_3}^3\chi+33280\,\chi\,{\alpha_3}^2+1024\,\chi\,\alpha_3-1024\,\chi+20625\,{\alpha_3}^2+16500\,\alpha_3+3300\right)}{(\alpha_3+1)^3\chi}$
$\mathbf{C_2^5}$	$\frac{35}{312}\,\frac{\left(43\,{\alpha_3}^2+3\,\alpha_3-1\right)\tau_{12}}{\chi\,(\alpha_3+1)^2}$
$\mathbf{C_2^6}$	$\frac{5}{12}\,\frac{\tau_{12}\,(5\,\alpha_3+2)\alpha_3}{(\alpha_3+1)^2}$
$\mathbf{C_2^7}$	$-3/8\,\frac{\tau_{12}\,(5\,\alpha_3+2)\alpha_3}{\chi\,(\alpha_3+1)^2}$
$\mathbf{C_2^8}$	0
$\mathbf{D_2^1}$	$-3/4\,\frac{(5\,\alpha_3+2)(2\,\alpha_3+3)\tau_{12}}{\chi\,(\alpha_3+4)(\alpha_3+1)^2}$
$\mathbf{D_2^2}$	$\frac{5}{18}\,\frac{(5\,\alpha_3+2)^2\tau_{12}}{(\alpha_3+4)(\alpha_3+1)^2}$
$\mathbf{D_2^3}$	$-\frac{35}{192}\,\frac{(5\,\alpha_3+2)^2\tau_{12}}{\chi\,(2\,\alpha_3+5)(\alpha_3+1)^2}$
$\mathbf{D_2^4}$	0
$\mathbf{D_2^5}$	$-\frac{7}{45}\,\frac{\tau_{12}\,(5\,\alpha_3+2)(\alpha_3-1)}{(4\,\alpha_3+7)(\alpha_3+1)}$
$\mathbf{D_2^6}$	$\frac{5}{42}\,\frac{\tau_{12}\,(5\,\alpha_3+2)(\alpha_3-1)}{\chi\,(5\,\alpha_3+8)(\alpha_3+1)}$
$\mathbf{D_2^7}$	0
$\mathbf{D_2^8}$	0

Table 26: The coefficients for the interior velocity field (65) for ϵ^8.

	$\epsilon^{\mathbf{8}}$
$\mathbf{B_2^1}$	$-15/2\,\frac{\tau_{12}\,(5\,\alpha_3+2)\alpha_3}{\chi\,(\alpha_3+1)^2}$
$\mathbf{B_2^2}$	$\frac{7}{384}\,\frac{\tau_{12}\,(5\,\alpha_3+2)\alpha_3\left(5184\,\chi\,{\alpha_3}^2+1344\,\chi\,\alpha_3+192\,{\alpha_3}^4\chi+3776\,{\alpha_3}^3\chi-256\,\chi-19278\,{\alpha_3}^3-20628\,{\alpha_3}^2-7560\,\alpha_3-864-3645\,{\alpha_3}^4\right)}{(\alpha_3+4)(3\,\alpha_3+2)(\alpha_3+1)^4\chi}$
$\mathbf{B_2^3}$	$3/8\,\frac{(5\,\alpha_3+2)\tau_{12}\left(69\,{\alpha_3}^3+193\,{\alpha_3}^2+327\,\alpha_3+136\right)\alpha_3}{\chi\,(\alpha_3+4)(3\,\alpha_3+2)(\alpha_3+1)^3}$
$\mathbf{B_2^4}$	$-\frac{55}{16}\,\frac{\tau_{12}\,\alpha_3\,(5\,\alpha_3+2)^2}{(\alpha_3+1)^3}$
$\mathbf{B_2^5}$	$-1/10\,\frac{\tau_{12}\,\alpha_3\left(1750\,\chi\,\alpha_3+350\,\chi+1400\,\chi\,{\alpha_3}^2-975\,{\alpha_3}^2-780\,\alpha_3-156\right)}{\chi\,(\alpha_3+1)^3}$
$\mathbf{B_2^6}$	$\frac{132}{7}\,\frac{\alpha_3\,(2+9\,\alpha_3)\tau_{12}}{\chi\,(\alpha_3+1)^2}$
$\mathbf{B_2^7}$	$\frac{\tau_{12}\,(5\,\alpha_3+2)(15\,\alpha_3+2)}{(\alpha_3+1)^2}$
$\mathbf{B_2^8}$	$-\frac{7}{8}\,\frac{(5\,\alpha_3+2)(17\,\alpha_3+2)\tau_{12}}{\chi\,(\alpha_3+1)^2}$
$\mathbf{C_2^1}$	$1/16\,\frac{\tau_{12}\left(-216\,{\alpha_3}^4-747\,{\alpha_3}^3+246\,{\alpha_3}^2+792\,\alpha_3+240+1300\,{\alpha_3}^4\chi+4490\,{\alpha_3}^3\chi+3468\,\chi\,{\alpha_3}^2+952\,\chi\,\alpha_3+80\,\chi\right)}{(2\,\alpha_3+5)\chi\,(\alpha_3+1)^2(3\,\alpha_3+2)}$
$\mathbf{C_2^2}$	$-\frac{1}{768}\,\frac{\tau_{12}\,(5\,\alpha_3+2)\left(5184\,\chi\,{\alpha_3}^2+1344\,\chi\,\alpha_3+192\,{\alpha_3}^4\chi+3776\,{\alpha_3}^3\chi-256\,\chi-19278\,{\alpha_3}^3-20628\,{\alpha_3}^2-7560\,\alpha_3-864-3645\,{\alpha_3}^4\right)}{(\alpha_3+4)(3\,\alpha_3+2)(\alpha_3+1)^4\chi}$
$\mathbf{C_2^3}$	$-1/48\,\frac{\left(69\,{\alpha_3}^3+193\,{\alpha_3}^2+327\,\alpha_3+136\right)(5\,\alpha_3+2)\tau_{12}}{\chi\,(\alpha_3+4)(3\,\alpha_3+2)(\alpha_3+1)^3}$
$\mathbf{C_2^4}$	$\frac{5}{32}\,\frac{(5\,\alpha_3+2)^2\tau_{12}}{(\alpha_3+1)^3}$
$\mathbf{C_2^5}$	$-\frac{1}{2340}\,\frac{\tau_{12}\left(15050\,{\alpha_3}^3\chi+16100\,\chi\,{\alpha_3}^2+700\,\chi\,\alpha_3-350\,\chi+8775\,{\alpha_3}^2+7020\,\alpha_3+1404\right)}{\chi\,(\alpha_3+1)^3}$
$\mathbf{C_2^6}$	$\frac{2}{35}\,\frac{\tau_{12}\left(8\,\alpha_3-2+115\,{\alpha_3}^2\right)}{\chi\,(\alpha_3+1)^2}$
$\mathbf{C_2^7}$	$1/2\,\frac{\tau_{12}\,(5\,\alpha_3+2)\alpha_3}{(\alpha_3+1)^2}$
$\mathbf{C_2^8}$	$-\frac{7}{16}\,\frac{\tau_{12}\,(5\,\alpha_3+2)\alpha_3}{\chi\,(\alpha_3+1)^2}$

Table 27: The coefficients for the interior velocity field (65) for ϵ^8.

	$\epsilon^{\mathbf{8}}$
$\mathbf{D_2^1}$	$\frac{1}{128}\,\frac{\tau_{12}\,(5\,\alpha_3+2)\left(768\,{\alpha_3}^3\chi+2432\,\chi\,{\alpha_3}^2+2432\,\chi\,\alpha_3+768\,\chi+255\,{\alpha_3}^4+1002\,{\alpha_3}^3-180\,{\alpha_3}^2-456\,\alpha_3-96\right)}{\chi\,(\alpha_3+4)(3\,\alpha_3+2)(\alpha_3+1)^3}$
$\mathbf{D_2^2}$	$-\frac{5}{12}\,\frac{(5\,\alpha_3+2)\tau_{12}\left({\alpha_3}^2+16+18\,\alpha_3\right)}{\chi\,(\alpha_3+4)^2(\alpha_3+1)^2}$
$\mathbf{D_2^3}$	$\frac{35}{144}\,\frac{(5\,\alpha_3+2)^2\tau_{12}}{(2\,\alpha_3+5)(\alpha_3+1)^2}$
$\mathbf{D_2^4}$	$-\frac{9}{160}\,\frac{(5\,\alpha_3+2)^2\tau_{12}}{\chi\,(\alpha_3+2)(\alpha_3+1)^2}$
$\mathbf{D_2^5}$	0
$\mathbf{D_2^6}$	$-\frac{10}{63}\,\frac{\tau_{12}\,(5\,\alpha_3+2)(\alpha_3-1)}{(5\,\alpha_3+8)(\alpha_3+1)}$
$\mathbf{D_2^7}$	$\frac{9}{224}\,\frac{\tau_{12}\,(5\,\alpha_3+2)(\alpha_3-1)}{\chi\,(2\,\alpha_3+3)(\alpha_3+1)}$
$\mathbf{D_2^8}$	0

VITA

Edwin Greco was born in Orlando, Florida on December 10^{th} 1977 to Victoria Greco. His first memory is of taunting his mother with threats of jumping into the deepend of a swimming pool at the age of 2. This memory is immediately proceeded by the memory of his mother lifting him, from his hair, up and out of that swimming pool. Shortly thereafter he met his step-father Richard Hooker, who rode a Harley Davidson and sparked in him a life long love affair with motorcycles. By the age of 6 Edwin had received his first motorcycle. At the age of 7, he was briefly involved in his first police chase; crashing into a barbed-wire fence before being caught. At the age of 12 his love of paper airplanes and kites caused him to consider a career as an aerospace engineer. These ambitions were momentarily shelved, however, to persue his desire to become a Naturalist. This entailed exploring undeveloped land in the suburb's of Orlando and reading survival books. At the age of 14 Edwin was enrolled in a magnet school for science and engineering. By 15, Edwin's distaste for AutoCAD resulted in the refocusing of this interest into science. At the same time he began to fall in love with his future wife, Elizabeth, during their long bus rides home. At the age of 17 Edwin purchased a Yamaha FZ750, his first street legal motorcycle. Upon graduating, Edwin and Elizabeth attended Jacksonville University, where Edwin earned a B.S. in Mathematics and Physics. After marrying they moved to Atlanta, Georgia where Edwin could pursue graduate studies and Elizabeth would start medical school at Emory. In 2005, they were blessed by the birth of their daughter Madeline and in 2008 by Miranda. After graduation, Edwin plans to stay in Atlanta, taking a position as instructor within the Physics Dept. at Georgia Tech; conveniently located an hour south of excellent hiking and motorcycle riding in the Appalachian Mountains.

REFERENCES

[1] Acrivos, A., Jeffrey, D. J., and Saville, D. A., "Particle migration in suspensions by thermocapillary or electrophoretic motion," *Journal of Physics of Fluids*, vol. 212, p. 95, 1990.

[2] Anderson, J. L., "Droplet interactions in thermocapillary motion," *Int. J. Multiphase Flow*, vol. 11, p. 813, 1985.

[3] Barton, K. D. and Subramanian, R. S., "The migration of liquid drops in a vertical temperature gradient," *Journal of Colloid Interface Science*, vol. 133, No. 1, pp. 211–222, 1989.

[4] Barton, K. D. and Subramanian, R. S., "Thermocapillary migration of a liquid drop normal to a plane surface," *Journal of Colloid Interface Science*, vol. 137, no. 1, pp. 170–182, 1990.

[5] Brenner, H., "The stokes resistance of a slightly deformed sphere," *Chemical Engineering Science*, vol. 19, pp. 519–539, 1964.

[6] Chen, S. H., "Thermocapillary migration of a fluid sphere parallel to an insulated plane," *Langmuir*, vol. 15, pp. 8618–8626, 1999.

[7] Craster, R. V. and Matar, O. K., "On the dynamics of liquid lenses," *Journal of Colloid and Interface Science*, vol. 303, pp. 503–516, 2006.

[8] Ganatos, P., Pfeffer, R., and Weinbaum, S., "A numerical-solution technique for three-dimensional stokes flows, with applications to the motion of strongly interacting spheres in a plane," *Journal of Fluid Mechanics*, vol. 84, part 1, pp. 79–111, 1978.

[9] Garnier, N., Grigoriev, R. O., and Schatz, M. F., "Optical manipulation of microscale fluid flow," *Physical Review Letters*, vol. 91, no. 5, p. 054501, 2003.

[10] Grigoriev, R. O., "Chaotic mixing in thermocapilary-driven microdroplets," *Physics of Fluids*, vol. 17, p. 033601, 2005.

[11] Grigoriev, R. O., Sharma, V., and Schatz, M. F., "Optically controlled mixing in microdroplets," *Lab on a Chip*, vol. 6, p. 1369, 2006.

[12] Hadland, P. H., Balasubramaniam, R., Wozniak, G., and Subramanian, R. S., "Thermocapillary migration of bubbles and drops at moderate to large marangoni number and moderate reynolds number in reduced gravity," *Experiments in Fluids*, vol. 26, pp. 240–248, 1999.

[13] Happel, J. and Brenner, H., *Low Reynolds Number Hydrodynamics*. Noordhoff International Publishing, 1973.

[14] Hassonjee, Q., Ganatos, P., and Pfeffer, R., "A strong-interaction theory for the motion of arbitrary three-dimensional clusters of spherical particles at low reynolds number," *Journal of Fluid Mechanics*, vol. 197, pp. 1–37, 1988.

[15] http://www.netlib.org/lapack/, "Lapack – linear algebra package." Internet, Nov. 2007.

[16] Kevorkian, J. and Cole, J. D., *Pertubation methods in applied mathematics*. Springer-Verlag, 1981.

[17] Kotz, K. T., Noble, K. A., and Faris, G. W., "Optical microfluidics," *Applied Physics Letters*, vol. 85, pp. 2658–2660, September 2004.

[18] Kralchevsky, P. A. and Nagayama, K., *Particles at Fluid Interfaces and Membranes*. Elsevier Science B. V., 2001.

[19] Lacy, L. L., Witherow, W. K., Facemire, B. R., and Nishioka, G. M., "Optical studies of a model binary miscibility gap system," technical memorandum, NASA: Marshall Space Flight Center, 1982.

[20] Lamb, H., *Hydrodynamics*. Cambridge University Press, 6th ed., 1932.

[21] Lee, S. H., Chadwick, S., and Leal, L. G., "Motion of a sphere in the presence of a plane interface. part 1. an approximate solution by generalization of the method of lorentz," *Journal of Fluid Mechanics*, vol. 93, part 4, pp. 705–726, 1979.

[22] Levich, V. G., *Physicochemical Hydrodynamics*. Prentice-Hall, 1962.

[23] Lide, D. R., *CRC Handbook of Chemistry and Physics*. CRC-Press, 79 ed., 1998.

[24] Loewenberg, M. and Davis, R. H., "Near-contact, thermocapillary migration of a nonconducting, viscous drop normal to a planar interface," *Journal of Colloid and Interface Science*, vol. 160, pp. 265–274, 1993.

[25] Ma, X., Balasubramaniam, R., and Subramanian, R. S., "Numerical simulation of thermocapillary drop motion with internal circulation," *Numerical Heat Transfer, Part A (Applications)*, vol. 35, pp. 291–309, 1999.

[26] Merritt, R. M. and Subramanian, R. S., "Migration of a gas bubble normal to a plane horizontal surface in a vertical temperature gradient," *Journal of Colloid and Interface Science*, vol. 131, no. 2, pp. 514–525, 1989.

[27] Meyyappan, M. and Subramanian, R. S., "Thermocapillary migration of a gas bubble in an arbitrary direction with respect to a plane surface," *Journal of Colloid and Interface Science*, vol. 115, no. 1, pp. 206–219, 1987.

[28] Meyyappan, M., Wilcox, W. R., and Subramanian, R. S., "The slow axisymmetric motion of two bubbles in a thermal gradient," *Journal of Colloid and Interface Science*, vol. 94, no. 1, pp. 243–257, 1983.

[29] Mohlenkamp, M. J., "A fast transform for spherical harmonics," *Journal of Fourier Analysis and Applications*, vol. 5(2/3), pp. 159–184, 1999.

[30] Nas, S., Muradoglu, M., and Tryggvason, G., "Pattern formation of drops in thermocapillary migration," *International Journal of Heat and Mass Transfer*, vol. 49, pp. 2265–2276, July 2006.

[31] Neuhaus, D. and Feuerbacher, B., "Bubble motions induced by a temperature gradient," in *Proceedings of the 6th European Symposium on Materials Science under Microgravity Conditions*, (Bordeaux, France), pp. 241–244, European Space Agency, December 1986.

[32] Pozrikidis, C., *Boundary Integral and Singularity Methods for Linearized Viscous Flow*. The Press Syndicate of the University of Cambridge, 1992.

[33] Pozrikidis, C., "Particle motion near and inside an interface," *Journal of Fluid Mechanics*, vol. 575, pp. 333–357, 2007.

[34] Ramos, J. I., "Lumped models of gas bubbles in thermal gradients," *Applied Mathematical Modelling*, vol. 21, pp. 371–386, 1997.

[35] Rybalko, S., Magome, N., and Yoshikawa, K., "Forward and backward laser-guided motion of an oil droplet," *Physical Review E*, vol. 70, p. 046301, 2004.

[36] Sen, A. K. and Davis, S. H., "Steady thermocapillary flows in two-dimensional slots," *Journal of Fluid Mechanics*, vol. 121, pp. 163–186, 1982.

[37] Smith, H. D., Mattox, D. M., Wilcox, W. R., Subramanian, R. S., and Meyyappan, M., "Experimental observation on the thermocapillary driven motion of bubbles in a molten glass under low gravity conditions," in *Materials Processing in the Reduced Gravity Environment of Space* (Rindone, G. E., ed.), (Boston Park Plaza Hotel, Boston, Massachusetts, U.S.A), pp. 279–288, Materials Research Society, New York : North-Holland, November 1982.

[38] Smith, K. A., Ottino, J. M., and de la Cruz, M. O., "Dynamics of a drop at a fluid interface under shear," *Physical Review E*, vol. 69, p. 046302, 2004.

[39] Sneeuw, N., "Global spherical harmonic analysis by least-squares and numerical quadrature methods in historical perspective," *Geophysical Journal International*, vol. 118, pp. 707–16, Sept. 1994.

[40] Srinivasarao, M., Collings, D., Philips, A., and Patel, S., "Three-dimensionally ordered arrray of air bubbles in a polymer film," *Science*, vol. 292, p. 79, 2001.

[41] Stone, H. A., Stroock, A. D., and Ajdari, A. R., "Engineering flows in small devices: Microfluidics toward a lab-on-a-chip," *Annual Review of Fluid Mechanics*, vol. 36, pp. 381–411, 2004.

[42] Subramanian, R. S. and Balasubramaniam, R., *The Motion of Bubbles and Drops in Reduced Gravity*. Cambridge University Press, 2001.

[43] Swanson, T. D., Juhasz, A., Long, W. R., and Ottenstein, L., "Workshop on Two-Phase Fluid Behavior in a Space Environment," *NASA STI/Recon Technical Report N*, vol. 89, pp. 26184–+, 1989.

[44] Thompson, R. L., DeWitt, K. J., and Labus, T. L., "Marangoni bubble motion phenomenon in zero gravity," *Chemical Engineering Communications*, vol. 5, no. 5-6, pp. 299–314, 1980.

[45] Vainchtein, D., Widloski, J., and Grigoriev, R. O., "Mixing properties of steady flow in thermocapillary driven droplets," *Physics of Fluids*, vol. 19, p. 167102, 2007.

[46] Wang, Y., Mauri, R., and Acrivos, A., "Thermocapillary migration of a bidisperse suspension of bubbles," *Journal of Fluid Mechanics*, vol. 261, pp. 47–64, 1994.

[47] Wei, H. and Subramanian, R. S., "Thermocapillary migration of a small chain of bubbles," *Physics of Fluids A*, vol. 5, no. 7, pp. 1583–1595, 1993.

[48] Wozniak, G., "On the thermocapillary motion of droplets under reduced gravity," *Journal of Colloid and Interface Science*, vol. 141, no. 1, pp. 245–254, 1991.

[49] Xie, J., Lin, H., Zhang, P., Liu, F., and Hu, W., "Experimental investigation on the thermocapillary drop migration at large marangoni number in reduced gravity," *Journal of Colloid and Interface Science*, vol. 285, pp. 737–743, 2005.

[50] Young, N. O., Goldstein, J. S., and Block, M. J., "The motion of bubbles in a vertical temperature gradient," *Journal of Fluid Mechanics*, vol. 6, p. 350, 1959.